Master's thesis

NTNU
Norwegian University of Science and Technology
Faculty of Natural Sciences
Department of Chemistry

Mats Solberg Nes

Understanding the Effects of TiO_2 Anchoring Groups on the Optical Properties of Chromophores in Dye-Sensitized Solar Cells

Master's thesis in Chemistry
Supervisor: Solon Oikonomopoulos
May 2020

NTNU
Norwegian University of
Science and Technology

NTNU

Norwegian University of
Science and Technology

Understanding the Effects of TiO_2 Anchoring Groups on the Optical Properties of Chromophores in Dye-Sensitized Solar Cells

Mats Solberg Nes

Master of Science in Chemistry
Submission date: May 2020
Supervisor: Solon Oikonomopoulos, IKJ

Norwegian University of Science and Technology
Department of Chemistry

I hereby declare that the work done in this thesis is independent and in accordance with the rules and regulations of the Norwegian University of Science and Technology.

May 29, 2020

Mats Solberg Nes

Mats Solberg Nes

Acknowledgements

This master's thesis, titled *Understanding the Effects of TiO_2 Anchoring Groups on the Optical Properties of Chromophores in Dye-Sensitized Solar Cells*, was performed at the Department of Chemistry at NTNU in Trondheim between September 2018 and May 2020.

Firstly, I would like to thank my supervisor Associate Professor Solon Oikonomopoulos without whom this project would be impossible. With his unconventional work schedule he has taught me the virtue of patience and the value of thinking by myself, for which I am grateful.

I would also like to extend my gratitude towards department engineer Roger Aarvik for tirelessly providing the research group with chemicals and equipment, and to senior engineer Susanna Villa Gonzalez for conducting and interpreting mass spectroscopy analyses.

The learning curve at a synthetic organic lab can be steep and unforgiving, but due to the supportive and encouraging atmosphere of the Solar Cells research group it has felt like a privilege to be able to take part of it, and I am confident that my time at NTNU is one I will look back at with proud and joy. This is especially due to the excellent guidance of PhD student David Moe Almenningen from whom I have learnt greatly. A special thanks to fellow masters' student Are Joacim Hognes is also in order as we have shared countless hours in the laboratory working together, and we have learnt to find solace in each other's low yields.

Lastly, I would like to extend my gratitude towards my parents Randi Solberg and Olav-Magnar Nes for their continuous support and encouragement, and for sponsoring me with coffee during my five years at NTNU.

Abstract

The world is in dire need for a shift towards green and renewable energy sources due to the increasing effects of global warming being felt around the globe. Dye-sensitized solar cells (DSSCs) is one of numerous solar cell technologies which has seen a surge in research and development in recent years. DSSCs stands as a semi-transparent, flexible, cheap and highly tuneable alternative which can contend against the more conventional silicon-based solar cells.

In this study, three novel phenothiazine-based chromophores (**MSN-004** – **MSN-006**), in addition to a reference dye (**MSN-003**), bearing different anchoring groups have been synthesized. **MSN-003** and **MSN-004** were synthesized following a five-step synthesis in a total yield of 15 and 3% respectively, and **MSN-005** and **MSN-006** were synthesized in a total yield of 1 and 10% following a three-step synthesis. Optical analyses were conducted on the dyes **MSN-003**, **MSN-004** and **MSN-006** before and after adsorption on the TiO_2-semiconductor in order to ascertain the influence the anchoring groups has on the optical properties of the chromophores. In addition, the photovoltaic performance and dye-loading properties of said dyes were also measured.

A bathochromic shift of absorption was measured for **MSN-004** and **MSN-006** when adsorbed onto the TiO_2-semiconductor, whereas **MSN-003** gave a hypsochromic shift. A correlation between the photovoltaic performance and dye-loading was also found, ranking the dyes in descending order of PCE and dye loading: **MSN-003** >> **MSN-004** > **MSN-006**.

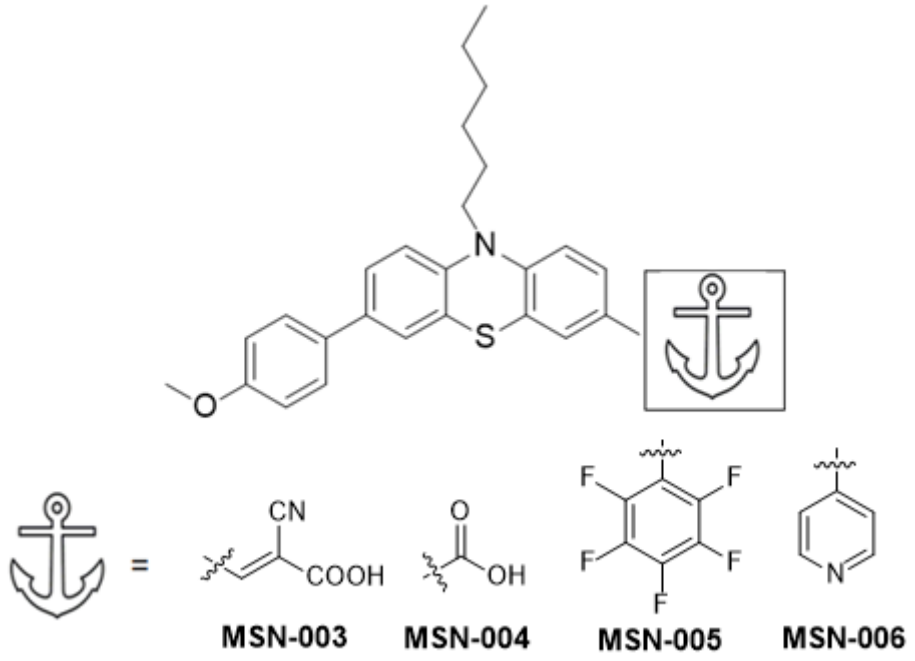

Figure 1: The synthesized dyes during this project.

Table of Content

Symbols and Abbreviations

δ	Chemical Shift
η	Power Conversion Efficiency
λ_{max}	Wavelength of Maximum Absorption
2D	Two-Dimensional
A	Anchoring Group
AM	Air Mass
br	Broad
CB	Conduction Band
CDCA	Chenodeoxycholic Acid
COSY	Correlated Spectroscopy
CV	Cyclic Voltammetry
d	Doublet
D	Donor Group | Dye Molecule
D^*	Excited Dye Molecule
D^+	Oxidized Dye Molecule
dd	Doublet of Doublet
DFT	Density Functional Theory
DCM	Dichloromethane
DMF	Dimethylformamide
DMSO	Dimethyl Sulfoxide
DSSC	Dye-Sensitized Solar Cell
e^-	Elementary Charge
$E_{1/2}$	Half-Wave Potential
$E_{0\text{-}0}$	Band-Gap Energy
EtOAc	Ethyl Acetate
eq.	Equivalent
FF	Fill Factor
FTO	Fluorine-Doped Tin Oxide
FTIR	Fourier-Transform Infrared Spectroscopy

h	Hours
HMBC	Heteronuclear Multiple Bond Correlation Spectroscopy
HOMO	Highest Occupied Molecular Orbital
HRMS	High Resolution Mass Spectroscopy
HSQC	Heteronuclear Single Quantum Coherence Spectroscopy
ICT	Intramolecular Charge Transfer
IPCE	Incident Photon-to-Current Conversion Efficiency
IR	Infrared
J	Coupling Constant
J_{max}	Current Density at Maximum Power Point
J_{sc}	Short-Circuit Current Density
lit.	Literature
LUMO	Lowest Unoccupied Molecular Orbital
m	Medium | Multiplet
$[M]^+$	Molecular Ion
$[M+H]^+$	Protonated Molecular Ion
m/z	Mass to Charge Ratio
MLCT	Metal to Ligand Charge Transfer
mp	Melting Point
NBS	N-Bromosuccinimide
NHE	Normal Hydrogen Electrode
NMP	N-Methyl-2-pyrrolidon
NMR	Nuclear Magnetic Resonance
NTNU	Norwegian University of Science and Technology
P_{max}	Maximum Power Output
P_{in}	Intensity of Illumination
PCE	Power Conversion Efficiency
q	Quartet
quint.	Quintet
R_f	Retention Factor
rt	Room Temperature

s	Singlet | Strong
t	Triplet
td	Triplet of Doublets
THF	Tetrahydrofuran
TLC	Thin Layer Chromatography
UV-Vis	Ultraviolet-Visible Light
V_{max}	Voltage at Maximum Power Point
V_{OC}	Open-Circuit Voltage
w	Weak
w/	With
w/o	Without

Numbered Compounds

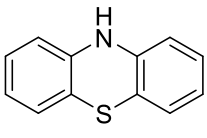

1

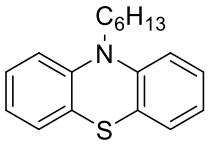

2

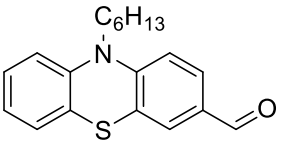

3

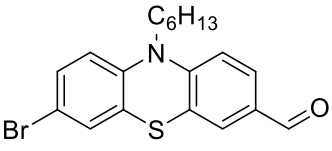

4

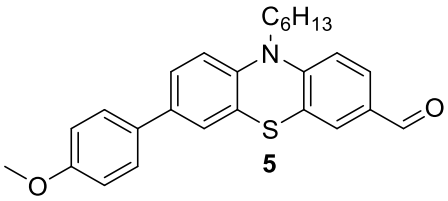

5

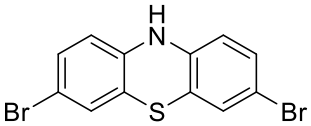

6

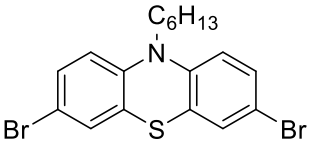

7

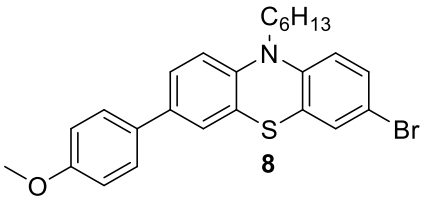

8

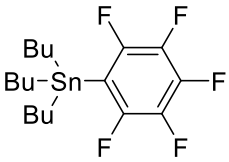

9

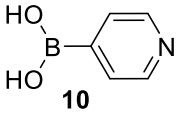

10

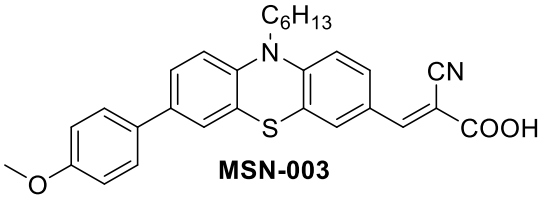

MSN-003

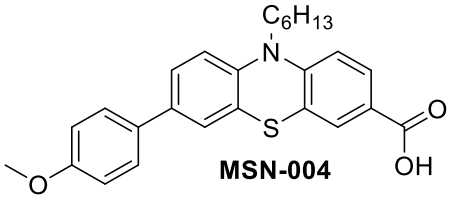

MSN-004

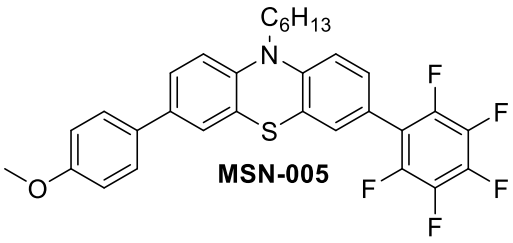

MSN-005

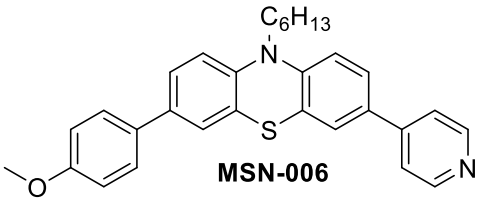

MSN-006

1 Introduction

The energy demand of the planet is expected to increase by almost 50% within 2050,[1] and to meet this demand in a sustainable fashion regarding the climate it is important that the renewable energy sources available to us are exploited as efficiently as possible. When comparing health risks, environmental impact and the cost of the different energy sources, nuclear energy wins out.[2] Nuclear energy is however plagued by issues with waste management, weapons development and the fear of nuclear accidents. This has led to several countries pledging to a nuclear power phase-out, such as Germany planning to shut down all its reactors within 2022. The increasing discontinuation of nuclear energy increases the burden of the remaining renewable energy sources, and the development of these alternative sources has to continue with accelerated effort in the future.

Solar energy is a clear contender to solving the projected surge in energy demand as the earth receives enough solar energy in 40 minutes to cover the global energy requirements for a whole year.[3] And within this field, dye-sensitized solar cells (DSSCs) has shown great promise.

DSSCs are part of the third generation of photovoltaic technologies which has gained a lot of attention in recent years and offers exciting properties which can contend to the more conventional silicon-based solar cells. Currently, DSSCs have reached power conversion efficiencies close to 15%,[4] which is still considerably lower than that of silicon-based solar cells (up to 46%).[5] But where the DSSCs really shine, is their high degree of tuneability in regard to shape, colour and transparency. DSSCs also outperform silicon-based solar cells under diffuse light conditions and elevated temperatures,[6] as well as in fabrication costs.

1.2 Background and Aim of the Project

This master's thesis is part of an ongoing collaboration between the theoretical chemistry department and the organic electronics research group. The project aims to examine the differentiations on the optical properties of the chromophores once anchored to the TiO_2-semiconducor by altering the anchoring group. To this end, phenothiazine-based chromophores have been synthesized, bearing different types of anchoring groups and evaluated towards their optical properties and ultimately their effect on the resulting device efficiency. The anchoring groups chosen consists of the most commonly used (-COOH and -cyanoacrylic group), as well as ones predicted (through collaboration with theoretical chemistry) to have the most prominent optical shift effects (-pyridine and -perfluorophenyl). In order to extract meaningful and comparable results the main chromophore for a series of varying anchoring groups has been kept constant.

2 Theory

2.1 Fundamentals of Solar Cells

Solar energy, which is abundant and clean, has been harnessed by plants via photosynthesis for millions of years but has only recently been exploited by humans. It was not until 1839 that the photovoltaic effect was discovered by Edmond Bequerel who did experiments with illuminated metal

electrodes in an electrolyte solution.[7] This sparked a newfound interest in the field and in 1883 the first solar cell made with a selenium/gold junction reported an efficiency of 1%.[8] The photovoltaic effect could however not be fully explained until the pioneering works of Albert Einstein in 1905, describing how electrons could be emitted from a solid due to absorption of photons.[9]

The sun emits light in a range of wavelengths, however, they do not reach the ground in the same intensity. This is due to molecules in the atmosphere, such as ozone and carbon dioxide, preferentially absorbing specific wavelengths of the incoming sunlight. The atmospheres effect on the incoming sunlight is adjusted by using the concept of air mass (AM). AM is defined as the relative length of a direct sunbeam through the atmosphere. AM 1 defines a vertical entry of radiation in the atmosphere hitting the equator. The standard measurement condition for photovoltaic cells states an AM of 1.5G, which corresponds to a solar angle of approximately 48°. The solar radiation spectrum of AM 1.5G is shown in **Fig. 2.1**.

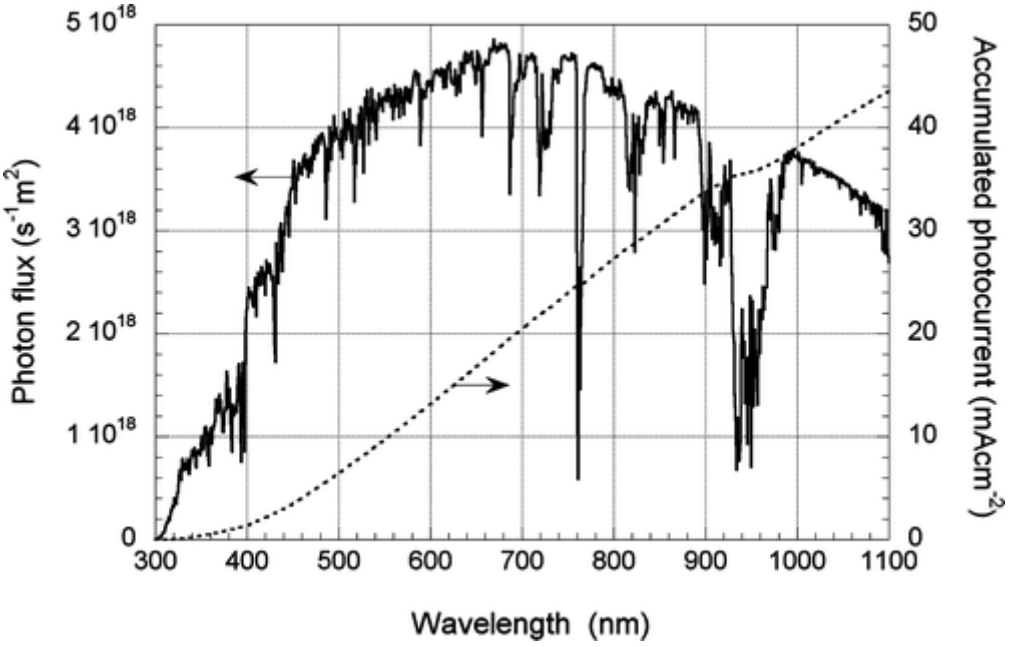

Figure 2.1. Photon flux of an AM 1.5G spectrum at 1000 W/m^2, along with calculated accumulated photocurrent (dashed line).[6]

The electrical characteristics of a photovoltaic cell can be summarized in a *J-V* curve, as shown in **Fig. 2.2**. The curve is obtained by applying a variable voltage across the solar cell during illumination while measuring the current. J_{SC} is the short-circuit current and correlates to the maximum current provided when the output connectors are shorted together. J_{SC} is strongly influenced by the light absorption of the dye molecule, the intramolecular charge transfer (ICT) and the subsequent electron injection to the semiconductor. The open-circuit voltage, V_{OC}, is the maximum voltage produced when the terminals are not connected to any load, and is affected by the concentration of electrons in the conduction band of the semiconductor. In both extremes, J_{SC} and V_{OC}, no power is produced. But in between these points power will be produced, and P_{max} is the point where the solar cell has the highest power output.

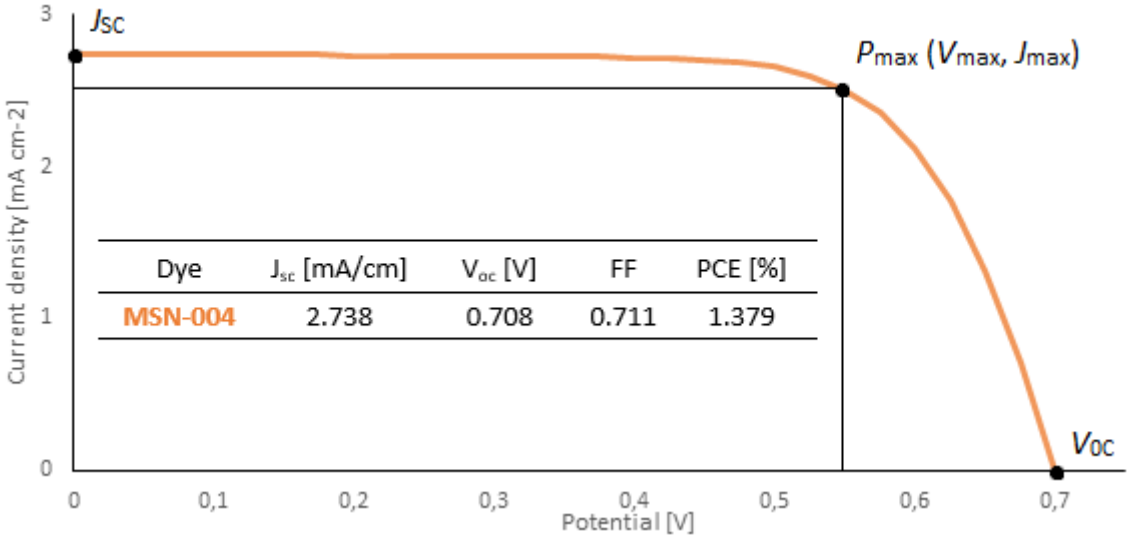

Figure 2.2: *J-V* curve for **MSN-004** measured under 1.5G illumination, along with calculated photovoltaic values.

The fill factor (FF) is the relationship between the maximum power produced by the solar cell and the product of J_{SC} and V_{OC}, and can be seen as a measurement of the squareness/ideality of the *J-V* curve.

$$\mathrm{FF} = \frac{\mathrm{J_{max}} * \mathrm{V_{max}}}{\mathrm{J_{SC}} * \mathrm{V_{OC}}} \tag{2.1}$$

The power conversion efficiency (PCE, η) of a solar cell is the most commonly used measurement for a photovoltaic cells' performance. This value is determined as the fraction of incident power which is converted to electricity, and is given by the following equation.

$$\mathrm{PCE} = \frac{\mathrm{J_{SC}} * \mathrm{V_{OC}} * \mathrm{FF}}{\mathrm{P_{in}}} * 100\% \tag{2.2}$$

Where P_{in} is the intensity of the incoming illumination [mW/cm^2].

Another measurement for the efficiency of a solar cell is the incident photon-to-electron conversion efficiency (IPCE). In this measurement the solar cell is illuminated by monochromatic light, and the current is again measured. This differs from standard PCE measurements as a reference photodiode is measured before each cell to calculate the actual number of photons illuminating the surface. IPCE values represent the ratio of electrons generated to the number of incident photons, per wavelength, as shown in the following equation.[3]

$$\mathrm{IPCE} = \frac{\text{Photocurrent Density}}{\text{Wavelength} * \text{Photon Flux}} \tag{2.3}$$

2.2 Dye-Sensitized Solar Cells (DSSC)

DSSCs were first invented by Grätzel and O'regan in 1991 and are regarded as the latest addition in solar cell technology.[10] These electrochemical cells consist of four main parts; a working electrode, counter electrode, semiconductor and an electrolyte. Both the working- and counter electrode are made electrically conductive by coating a sheet of glass with fluorine-doped tin oxide (FTO). The semiconductor, most commonly a 10 µm thick film of TiO_2 particles (10-30 nm in diameter), is then sintered on top of the working electrode.[3] The titanium oxide is then coated with a monolayer of dye-molecules before the electrodes are sandwiched together between a layer of electrolyte, as shown in **Fig. 2.3**.

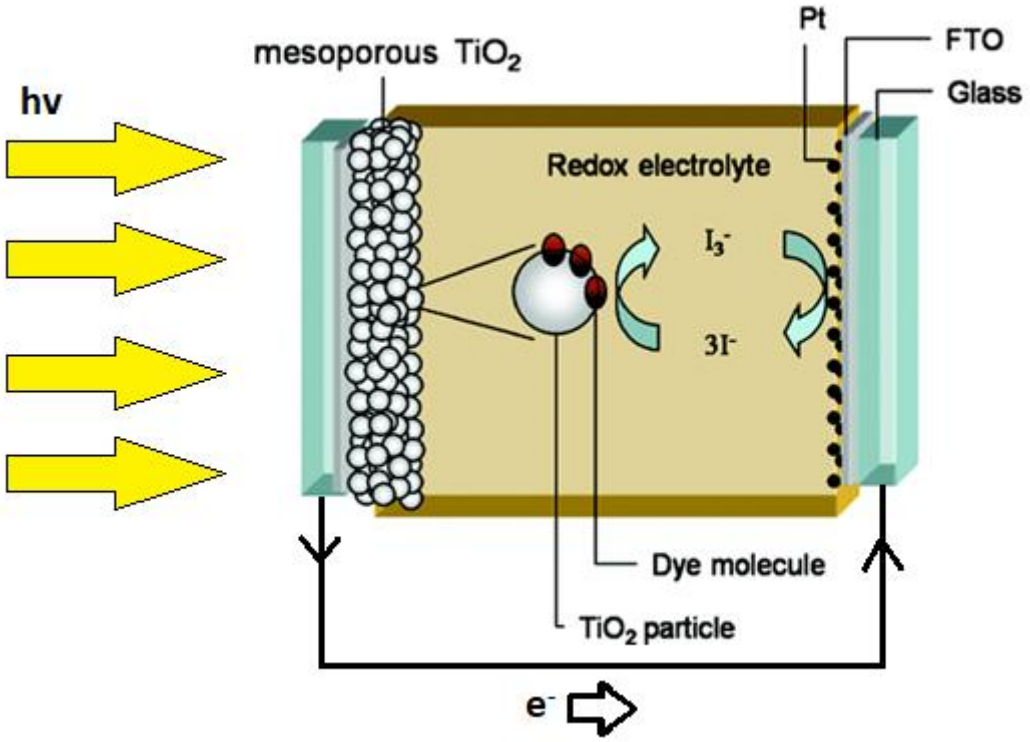

Figure 2.3: General construction of DSSCs.[6]

The fundamental difference between DSSCs and conventional silicon-based solar cells lies with the mechanisms of charge transport. Silicon solar cells generate electron flow through a *P-N* junction, which is the interface between two types of semiconducting materials. The *N* side contains an excess of negative charges, while the *P* side contains a deficit of negative charges. The difference in electric charge at the boundary leads to electrons migrating from the *N* side to the *P* side, establishing a permanent electrical field which only allows electrical current to pass in one direction. Incoming photons will knock off electrons on the *N* side, creating an electron-hole pair, which is separated by the electric field. The electron is then reintroduced to a hole on the *P* side via the external circuit.

In the case of DSSCs, light absorption does not lead to free electrons and holes, but to the formation of excitons.[10] Excitons are bound electron-hole pairs and can be regarded as a mobile excited state.[11] The electron of the exciton is then injected into the conductive band of the semiconductor due to the LUMO-LUMO (Lowest Unoccupied Molecular Orbital) energy difference of the sensitizer and semiconductor, and the charge transport is carried out between the semiconductor and electrolyte. The oxidized dye molecule is then reduced back to its neutral form via the electrolyte. The function of DSSCs encompasses a complex symbiosis of several different mechanisms. The advantages of this artificial photosynthetic process lie in the great possibility of optimization, such as

improving charge transfer by altering the semiconductor or chemically modifying the dye molecules for more efficient light capture. There are many electronic processes taking place inside a DSSC, some are more favourable than others. These processes are summarized in **Fig. 2.4**. Processes which contribute to the photogenerated current are marked with green arrows, while red arrows indicate unfavourable processes.

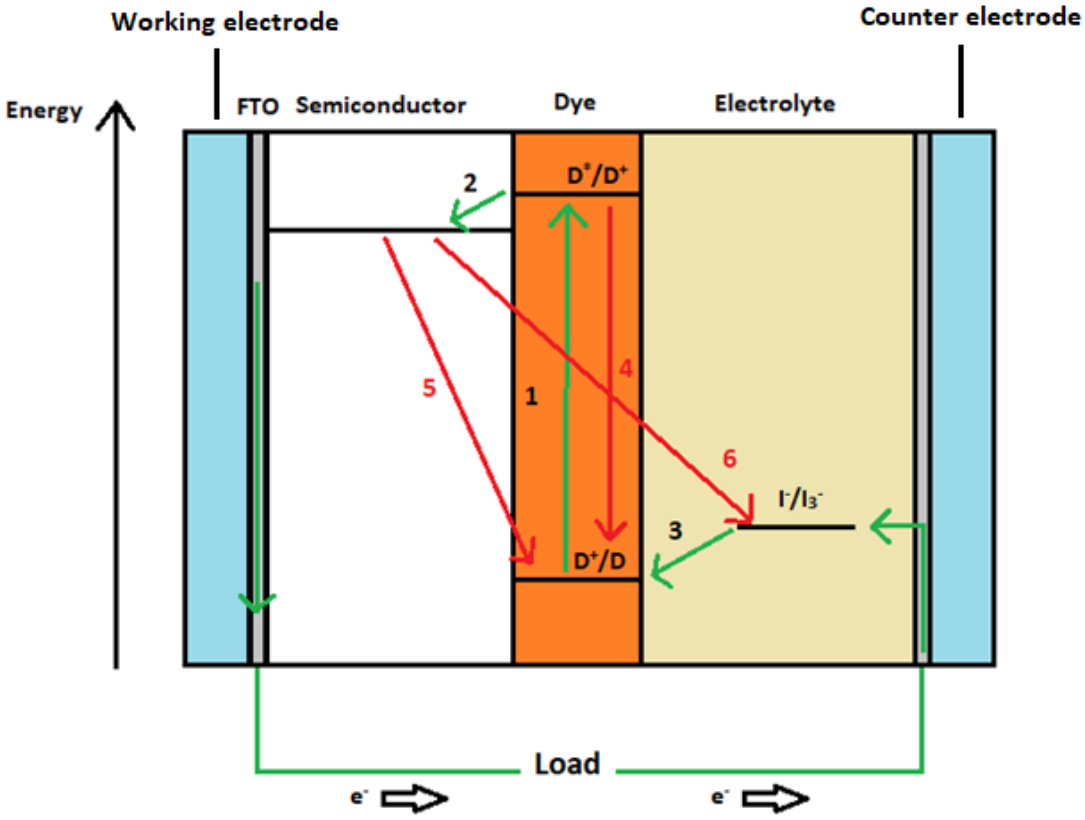

Figure 2.4: The electronic processes happening in DSSCs: 1) Excitation, 2) injection, 3) regeneration, 4) relaxation, 5) recombination to oxidized dye and 6) recombination to oxidized redox shuttle species.

The first process taking place is the excitation of the dye molecule due to absorption of photons, stated in the following equation:

$$\mathrm{D} + h\mathrm{v} \rightarrow \mathrm{D}^* \tag{2.4}$$

Where D and D^* is the ground state and excited state of the dye molecule, and *h*v is the energy of the incoming photon. The subsequent injection of the excited electron into the semiconductor can be described by Equation 2.5:

$$\mathrm{D}^* \rightarrow \mathrm{D}^+ + \mathrm{e}^-_{\mathrm{TiO_2}} \tag{2.5}$$

Where D^+ is the oxidized dye molecule generated when the excited dye, D^*, injects its electron into the TiO_2 conduction band.

The oxidized dye is subsequently reduced back to its neutral form via the I^-/I_3^- redox system, shown in Equation 2.6 and 2.7.

$$I_3^- + 2e^-_{(cathode)} \rightarrow 3I^-_{(cathode)} \quad (2.6)$$

$$D^+ + \frac{3}{2}I^- \rightarrow D + \frac{1}{2}I_3^- \quad (2.7)$$

The unfavourable reactions that might occur inside a DSSC are described in Equation 2.8 – 2.10. Firstly, the excited dye molecule, D*, can relax back to its ground state, D, generating a small amount of heat or producing a photon of less energy.

$$D^* \rightarrow D \quad (2.8)$$

Secondly, the excited dye molecule can react with the oxidized redox species, giving away its electron to the electrolyte instead of injecting it into the semiconductor.

$$D^* + \frac{1}{2}I_3^- \rightarrow D^+ + \frac{3}{2}I^- \quad (2.9)$$

The last of the unfavourable reactions is the transfer of an injected electron in the semiconductor to the oxidized redox species.

$$e^-_{TiO_2} + \frac{1}{2}I_3^- \rightarrow \frac{3}{2}I^- \quad (2.10)$$

Also illustrated in **Fig 2.4** are the relative energy levels of the different orbitals for the dye, semiconductor and electrolyte. These positions are fundamentally important for the function of DSSCs as a mismatch of energy levels could cause the whole process to become thermodynamically unfavoured. For the electron injection process the LUMO of the dye needs to be sufficiently higher in energy than the conductive band (E_{CB}) of the semiconductor ($E_{CB}(TiO_2)$ = -0.5 V), as the energy gap between these two levels are the driving force for electron injection.[12] For efficient electron injection a LUMO level of -0.7 V or higher is desirable for the chromophore.[13] The HOMO (Highest Occupied Molecular Orbital) of the dye must also be appreciably lower in energy than the redox potential of the I^-/I_3^- redox system (E_{redox} (I^-/I_3^-) = 0.42 V) for effective reduction of the dye to take place. A HOMO of ≥ 0.62 V for the chromophore is necessary for this process to be efficient.[13] All voltages are referenced towards normal hydrogen electrode (NHE).

The HOMO-LUMO bandgap of the dye can be tailored to match the energy levels of different kinds of semiconductors and redox media by chemically altering the molecule, which allows for great versatility. To obtain the energy gap between the HOMO and LUMO it is common to use cyclic voltammetry (CV). In this electrochemical technique a scanning potential is imposed on the dye while measuring the current produced. In the voltage-current plots this method produces, the HOMO and LUMO levels can be calculated from the maxima of the oxidation and reduction peaks or from the onset of these processes depending on the dye.[14]

2.3 Sensitizers for DSSCs

Early sensitizers used in DSSCs were dominated by metal complexes containing heavy transition metals such as ruthenium (Ru), osmium (Os) and iridium (Ir). The pioneering works of Grätzel and O'regan is largely attributed to this trend as they reported an efficiency of 7.12% of a Ru-based dye in 1991,[15, 16] shown in **Fig. 2.5**.

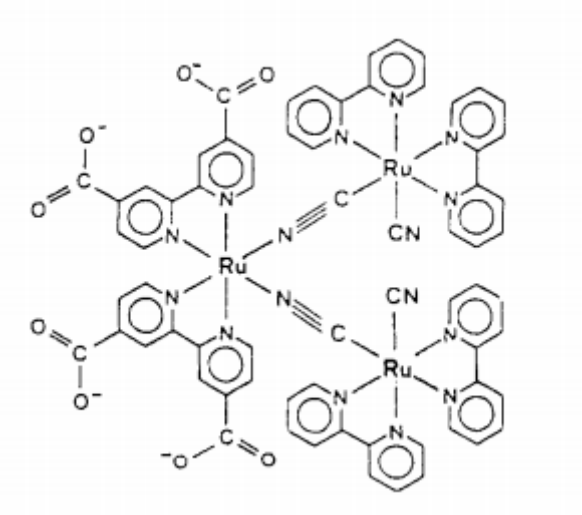

Figure 2.5: The Ru-based sensitizer used by Grätzel and O'regan with a reported efficiency of 7.12%.[15]

Metal complexes are well suited as sensitizers for several reasons, mainly because of their broad absorption spectrum ranging from the visible to the near-infrared. The central metal ion is crucial in defining the properties of the complex, as metal to ligand charge transfer (MLCT) processes accounts for light absorption in the visible region of the solar spectrum.[17] Additionally, ruthenium complexes frequently show good thermal and chemical stability, as well as suitable HOMO and LUMO levels.[6] Having sensitizers containing heavy transition metal ions naturally leads to some limitations due to issues of toxicity and availability, as well as ease of synthesis. Sensitizers containing metal complexes also exhibit moderate absorption coefficients, which means thicker films are needed.[3] However, the practical thickness of DSSCs are limited by electron diffusion length, and increasing the thickness does not necessarily translate to increased photocurrent due to the excitons not being able to reach the semiconductor to dissociate.[18]

As a result of the limitations accompanied with metal-based sensitizers, increasing research and development has been allocated towards metal-free sensitizers. The advantages of fully organic sensitizers lies with their reduced toxicity, high tuneability, cheaper production and possibility for thinner solar cells due to a higher molar extinction coefficients.[6] The general architectural structure of these types of sensitizers are based on a push-pull system containing a donor, π-bridge and an acceptor (commonly referred to as a D-π-A) structure. Other variants are also common, for example without a π-bridge (D-A) or with additional donor groups (often called auxiliary donors, D-D-A). Rather on relying on the MLCT process for excitation, these types of sensitizers utilize intramolecular charge transfer between the electron-rich donating group (D) and the electron-withdrawing acceptor-group (A).[19] A typical push-pull design using phenothiazine (**1**) as main chromophore is shown in **Fig. 2.6**.

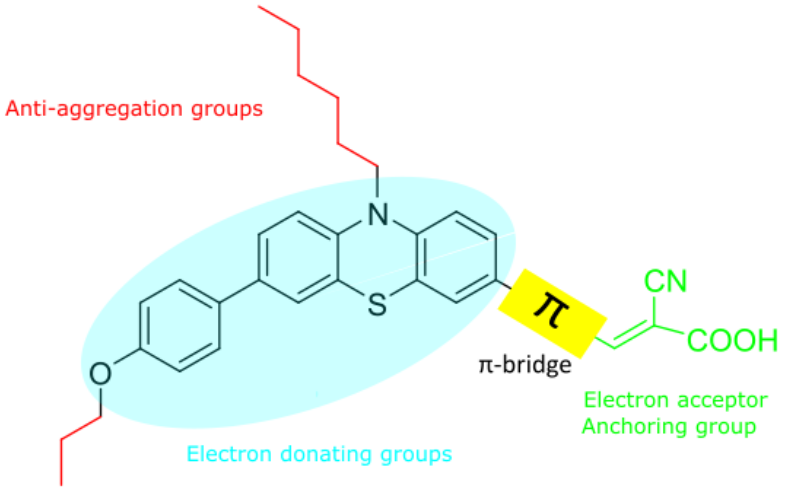

Figure 2.6: Design of a push-pull (D-D-π-A) phenothiazine-based sensitizer with its main components highlighted.

The HOMO level for the sensitizer is dictated by the donor moiety and π-bridge, and the LUMO level is dependent on the electron-withdrawing acceptor group.[19] This allows for optimization of device performance as each part of the D-π-A system can be easily exchanged. There are numerous different chromophores that metal-free dyes are based on, such as triarylamines,[20] squarenes,[21] coumarines[22] and phenothiazines.[13] Each of these moieties offers unique properties regarding chemical, optical and electronic characteristics, making this a highly diverse field within sensitizers.

2.4 Phenothiazine Sensitizers

Phenothiazine (**1**) was first synthesized in 1883 and found itself in widespread use in the 1930s after its anthelmintic and antibiotic properties were discovered.[23] It was not until 2007 that phenothiazine was first used as a sensitizer for DSSCs when Sun *et al.*[24] reported an efficiency of 5.5%.

Phenothiazine, which is composed of two benzene rings connected by a sulfur and a nitrogen atom, offers interesting characteristics due to its electron-rich heteroatoms. This leads to phenothiazine having stronger electron-donating properties than many other amines and *N*-heterocycles.[25] Phenothiazine also exhibits a unique non-planar butterfly conformation in its ground state which helps avoiding unwanted aggregation.[24] From a synthetic perspective there are three main reactive sites on the phenothiazine scaffold; N-10, C-3 and C-7, as seen on **Fig. 2.7**.

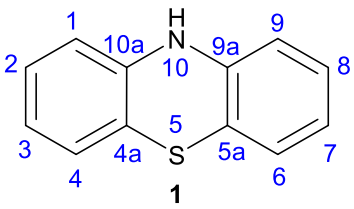

1

Figure 2.7: Phenothiazine (**1**) with numbered positions.

The nitrogen atom is often furnished with an alkyl chain for further anti-aggregation properties. The C-3 and C-7 positions can be readily functionalized with additional donor groups, π-spacers or

anchoring groups. These groups can be preferentially added to each reactive site, creating an asymmetric sensitizer as in the case of **Fig. 2.6**. Another possibility is to attach donor-π-bridge and anchoring groups to both C-3 and C-7 creating a D(-π-A)$_2$ sensitizer,[26] which has shown to increase efficiency by decreasing side-by-side π-stacking of the dye molecules.[19]

Buene *et al.* has conducted a comprehensive investigation of the photovoltaic effects accompanied with the introduction of π-spacers and additional donor groups on the phenothiazine scaffold.[3] It was found that additional donor groups provided moderate gains, yielding a 4-11% increase of PCE. This limited effect is most likely due to the folded nature of the phenothiazine scaffold along the N-S axis which restricts the conjugation between the donor and anchoring group, inhibiting electron donation. This phenomenon leads to the unfortunate result that any positive effects contributed by the auxiliary donor side of the phenothiazine sensitizer are severely impaired.

The introduction of π-spacers has generally been the most applied strategy for improving the performance of DSSCs, but in the case of phenothiazine-based sensitizers the π-spacers often result in a degradation of efficiency.[3, 24, 27, 28] A decrease in both V_{OC} and J_{SC} can be observed when introducing π-spacers, where the loss of J_{SC} is explained by an increase in recombination losses of electrons due to an increase of π-π stacking.[29] In addition, the large conjugated systems constructed by introducing π-spacers can also lead to an increase of photodegradation of the dye molecule and a decrease in the stability of the DSSCs.[30] The reasoning for the decrease in V_{OC} accompanied by the introduction of π-spacers is not found in the literature, but an explanation is given by Buene.[3] The decrease in V_{OC} is attributed to a change in E_{CB} for TiO_2. Buene has postulated that the change of E_{CB} is due to the π-spacer affecting the pKa of the dye. As the π-spacer increases the distance between the donor- and acceptor moieties, it is expected that the pKa of the anchoring group will decrease as the electron donation through induction is reduced. Lower pKa of the dye will lead to an increase in protonation of the TiO_2-surface during the staining procedure, which will lead to a shift of E_{CB} to a more positive potential.[31]

In summary the effects of the auxiliary donor groups are minor but positive. The introduction of π-spacers leads to improved absorption properties, but the decrease of V_{OC} and J_{SC} severely limits the performance enhancements. Lou *et al*.[30] (2016) has performed a comprehensive review of phenothiazine-based DSSCs, and the average values for the photovoltaic data emphasizing the correlation of V_{OC}, J_{SC} and PCE to π-spacers and auxiliary donors are given in **Table 2.1**.

Table 2.1: Average values of J_{SC}, V_{OC} and PCE of phenothiazine dyes with D-π-A, D-D-A and D-D-π-A structures in the review by Lou *et al.*

Dye structure	J_{SC} [mA cm^{-2}]	V_{OC} [mV]	PCE [%]
D-π-A	11.0	645	4.74
D-D-A	13.2	750	6.36
D-D-π-A	9.1	600	3.60

2.5 Anchoring Groups

The role of the anchoring group is crucial in the function of DSSCs as it is responsible for the interfacial electron injection between the dye and the semiconductor. In order to increase the efficiency, high affinity of the anchoring group to the semiconductor is desirable. The immobilization

of the sensitizer onto the semiconductor can be done through a multitude of mechanisms, including physical entrapment, van der Waals interactions, hydrogen bonding, hydrophobic interactions, electrostatic interactions and covalent bonding.[32] The main mechanism employed by DSSCs is covalent attachment, usually with carboxylic acid as the functional anchoring group.[6, 33] The binding modes for carboxylic-, cyanoacrylic-, pyridyl- and catechol anchoring groups are shown in **Fig. 2.8**.

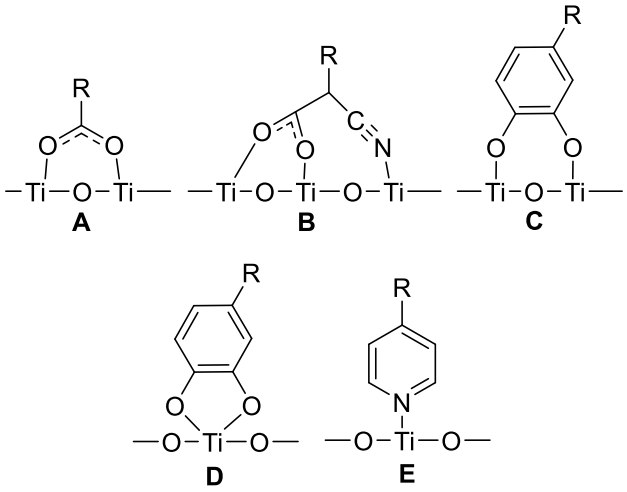

Figure 2.8: Different binding modes of anchoring groups on TiO_2 surface: Bidentate bridging of carboxyl group (**A**), bidentate bridging of carboxyl group combined with coordination bond of cyano group (**B**), bidentate binuclear bridging linkage of catechol (**C**), bidentate mononuclear chelating linkage of catechol (**D**) and coordination bond of pyridyl (**E**).

The carboxylic anchoring group is mainly considered to bind to the TiO_2 semiconductor via bidentate bridging linkage between the carboxyl group of the dye and the Brønsted acid sites on the TiO_2 surface (surface-bound hydroxyl groups, Ti-OH) (**Fig. 2.8 A**).[34] It has been found that the cyano group in the cyanoacrylic anchoring group can either increase or decrease the efficiency of the dye depending on the specific binding mechanism employed. The cyanoacrylic anchoring group can form a bidentate bridging linkage of the carboxyl group to the Brønsted acid sites on the TiO_2, identical to that of the carboxylic group (**Fig. 2.8 A**). This would lead to a decrease in efficiency of the dye due to the strong electron-withdrawing properties of the cyano group, which is not directly attached to the TiO_2, preventing electrons from being injected into the conduction band via the carboxylic acid moiety. However, if the cyano group binds to the TiO_2 surface in addition to the carboxylic group, both the stability of adsorption and electron injection properties are increased (**Fig. 2.7 B**).[35]

The catechol anchoring group has been known for binding to the Brønsted acid sites of the TiO_2 through bidentate binuclear bridging linkage (**Fig. 2.7 C**) or bidentate mononuclear chelating linkage (**Fig. 2.8 D**).[34] Pyridyl anchoring groups tend to form coordinate bonds on the Lewis acid sites on the TiO_2 surface (exposed Ti^{n+} sites), rather than forming bidentate bridging linkages (**Fig. 2. E**).[36] Pyridyl can also adsorb at Brønsted acid sites on the TiO_2 surface if they are not occupied, but show a higher affinity towards the Lewis acid sites.[37]

As the acceptor group is highly influential of the LUMO level of the dye molecule it will accordingly influence the light harvesting properties. It has been shown that the peak UV-Vis absorption wavelength of identical dyes bearing different anchoring groups follows the trend that the larger the Hammett value, the higher the electron withdrawing ability of the anchoring group, which corresponds to a larger bathochromic shift (red shift).[33] However, this trend is often complicated by effects of unwanted aggregation, solvatochromism, deprotonation of anchoring group and π-stacking interactions[33, 38] The optical shifts observed are also very dye-specific, where some dyes observe

little or no change, whereas in other cases the UV-Vis peak can be shifted by 100 nm or more in either direction.[39, 40] Prediction of UV-Vis-shifts has previously been done by using density functional theory (DFT), however such calculations are very time consuming and are not suitable for rapid screening tasks involving large number of molecules.[38] In a recent study (2019) by Venkatraman *et al.*[38] the successful prediction of spectral shifts accompanied with the adsorption of chromophores onto the TiO_2 semiconductor were identified in 80% of cases by utilizing machine learning.

2.6 Dye Aggregation

In an ideal situation the dye molecules would align themselves neatly on the semiconductor surface as a monolayer, with some space in between each dye molecule. This is however often not the case as dye molecules tend to form aggregates, which has the potential to severely disrupt the proper function of the DSSC. The two main forms of dye aggregates are H- (hypsochromic, blue shift) and J- (bathochromic, red shift) aggregates, illustrated in **Fig. 2.9**.[41]

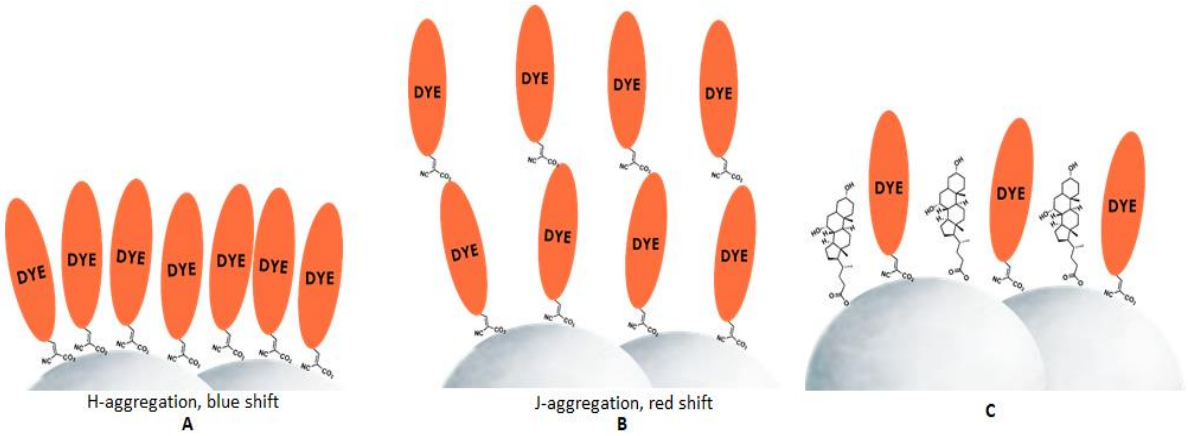

Figure 2.9: Illustrated H-aggregation (**A**), J-aggregation (**B**) and use of co-adsorbent (**C**).

J-aggregation is the phenomenon where dye molecules bind on top of each other instead of adsorbing on the semiconductor. This leaves the aggregating dye molecule unable to inject its electron into the semiconductor, and thus not contributing to the photogenerated current. J-aggregation might also prevent the electrolyte from reaching the bottommost dye on the semiconductor surface, inhibiting electron regeneration.[41]

H-aggregation is the process where dye molecules stack too close to each other in a side-by-side fashion, resulting in increased dye-dye interactions. H-aggregation has been found to broaden the absorption spectra for some dyes, but is generally considered to be an undesirable phenomenon in DCCSs due to the hypsochromic shift accompanied with H-aggregates impeding the chromophore from absorbing lower energy photons. A decrease in the rate of electron-injection between the dye and semiconductor has also been linked to the formation of H-aggregates, which increases the probability of the chromophore injecting its electron to the redox media instead of the semiconductor (Equation 2.9).[41]

Formation of dye aggregates can however be controlled through different strategies such as introducing anti-aggregating moieties on the dye molecule itself, for instance alkyl chains. Another

strategy is to utilize optical inert co-adsorbents, as depicted in **Fig. 2.9 C**, where chenodeoxycholic acid (CDCA) is adsorbed in-between the dye molecules inhibiting the formation of H-aggregates.

2.7 Target Molecules

The target molecules for this project, **MSN-003** – **MSN-006**, are shown in **Fig. 2.10**. Calculations performed by Venkatraman at the theoretical chemistry department at NTNU predicts a hypsochromic shift of absorption when anchored onto TiO_2 for **MSN-003**, **MSN-004** and **MSN-005** with confidences of 100%, 76% and 86% respectively. **MSN-006** is predicted to give a bathochromic shift of absorption with 78% certainty.

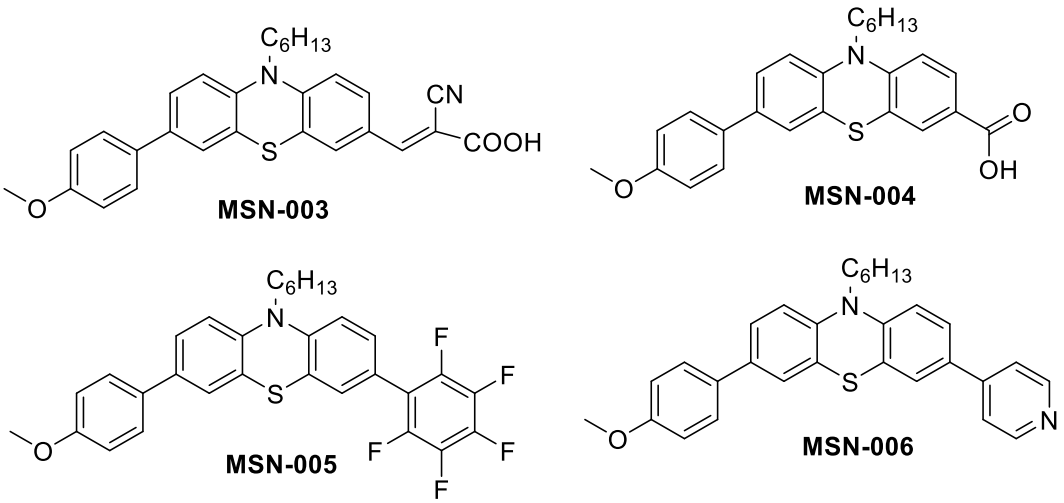

Figure 2.10: Dye molecules synthesized during the project.

The structure of the chromophores follows a D-D-A push-pull system as described in Section 2.3-2.4. The amine functionality is furnished with an *n*-hexyl chain to inhibit formation of aggregates while at the same time serving as a weak electron-donating moiety to the phenothiazine core. The donor-side of the chromophore is fitted with a 4-methoxyphenyl group for further increase of the electron donating properties of the dye. It was decided to omit the use of a π-spacer due to the very limited performance enhancements accompanied with its inclusion and in order to simplify the synthesis. The anchoring groups (cyanoacrylic- (**MSN-003**), carboxylic- (**MSN-004**), perfluorophenyl (**MSN-005**) and pyridyl- (**MSN-006**)) were chosen due to the strong predictions by Venkatraman *et al.*[38] of improved optical absorption once attached onto TiO_2.

The retrosynthetic route to **MSN-003** and **MSN-004** is shown in **Scheme 2.1**, and **Scheme 2.2** depicts the retrosynthetic route towards **MSN-005** and **MSN-006**. The reactions used in the synthesis is described in Section 2.8.

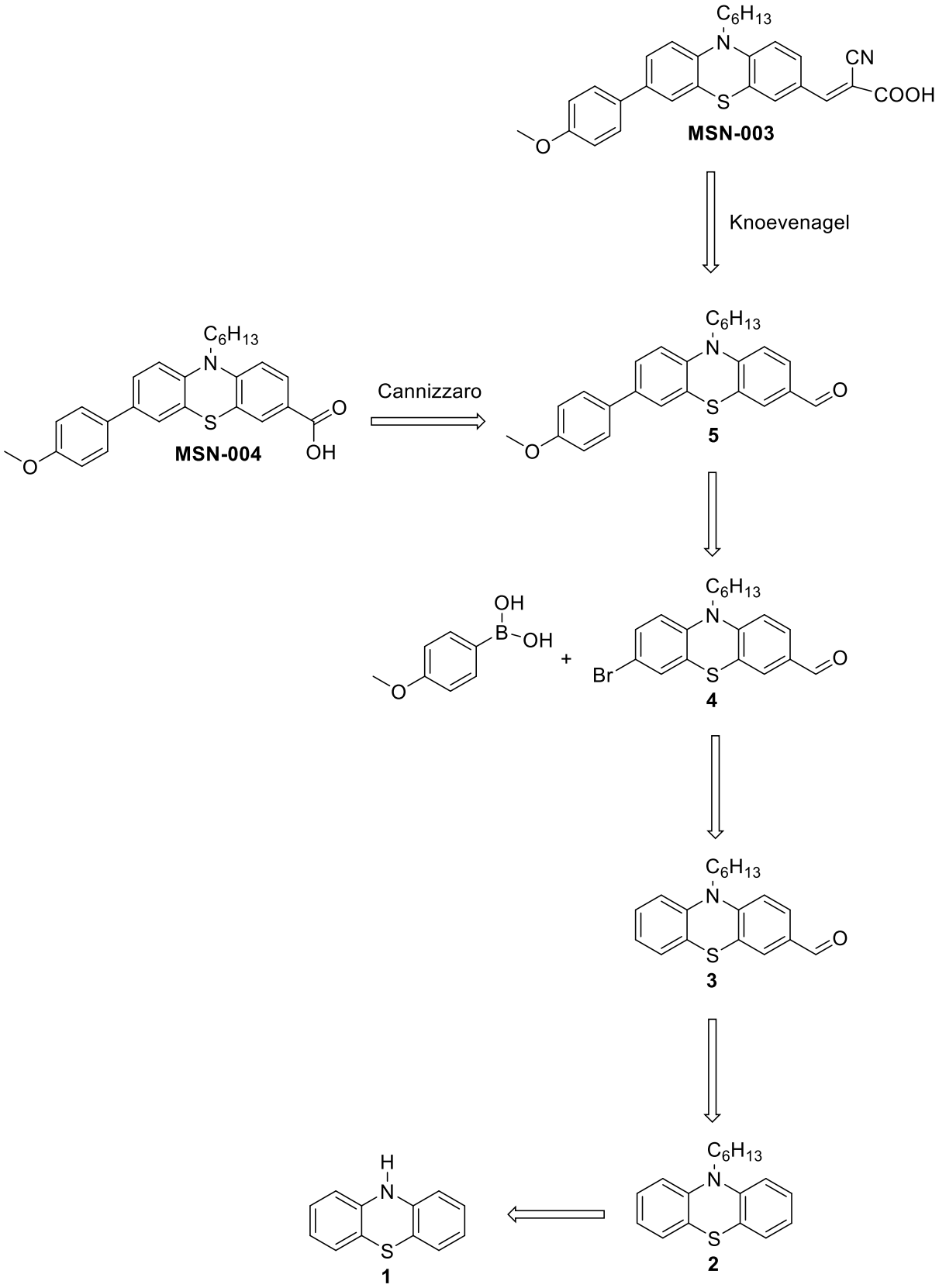

Scheme 2.1: Retrosynthetic route towards the target molecules **MSN-003** and **MSN-004**.

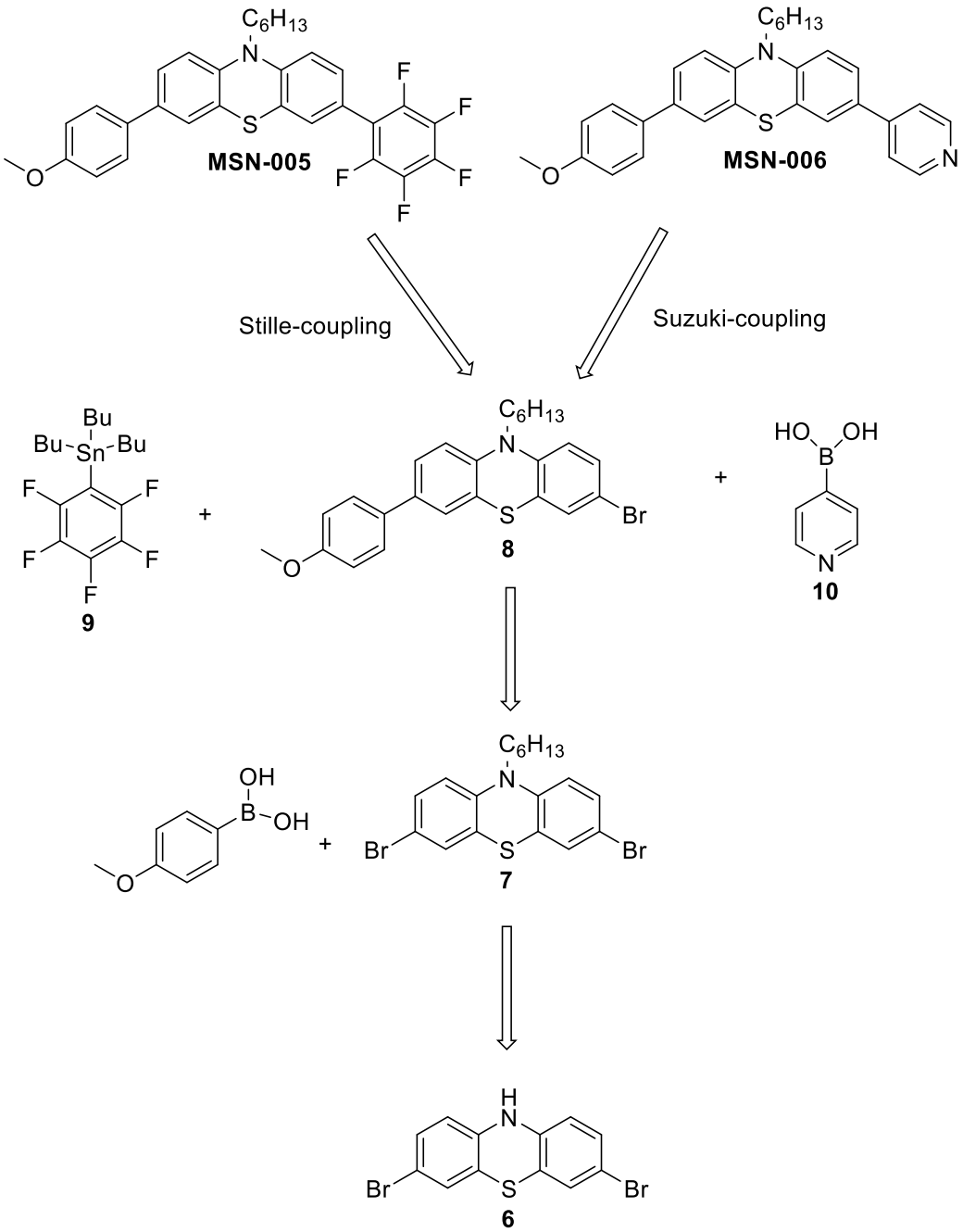

Scheme 2.2: Retrosynthetic route towards the target molecules **MSN-005** and **MSN-006**.

2.8 Reactions Used in the Synthesis

2.8.1 Amine Alkylation

The base-promoted alkylation of an amine with a haloalkane follows a simple S_N2-mechanism and produces a higher substituted amine.[42] Alkylation of amines can however be difficult to control as the basicity of the nitrogen atom increases with increased substitution of electron donating groups (e.g. alkyl chains), promoting further reaction with the haloalkane.[43] This issue is less prevalent when alkylating secondary amines as the generated tri-substituted amine will exhibit substantial steric hinderance preventing further reaction. The proposed mechanism for the base-promoted alkylation of a secondary amine is shown in **Scheme 2.8.1**.

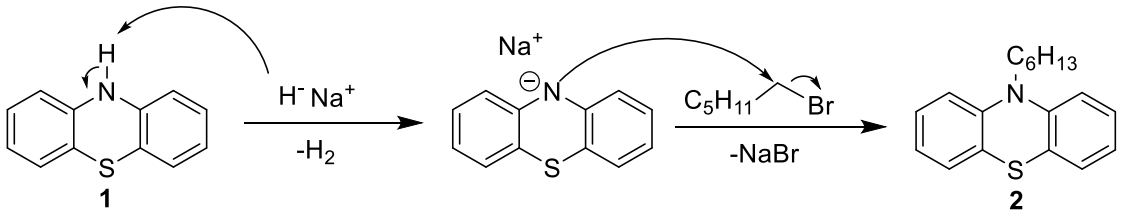

Scheme 2.8.1: Proposed mechanism for the formation of **2** via N-alkylation of **1** and *n*-bromohexane.

2.8.2 Vilsmeier-Haack Formylation

The Vilsmeier-Haack reaction is a common method of introducing an aldehyde-group to electron rich aromatic compounds, as well as electron rich alkenes.[44] The reaction uses phosphorous oxychloride ($POCl_3$) along with dimethylformamide (DMF) which reacts to form the Vilsmeier Reagent *in situ*. The Vilsmeier Reagent undergoes electrophilic aromatic substitution on the aromatic ring (or alkene) to produce an iminium intermediate. The iminium intermediate is then hydrolysed, yielding the formylated product. The proposed mechanism for Vilsmeier-Haack formylation of **2** is shown in **Scheme 2.8.2**.

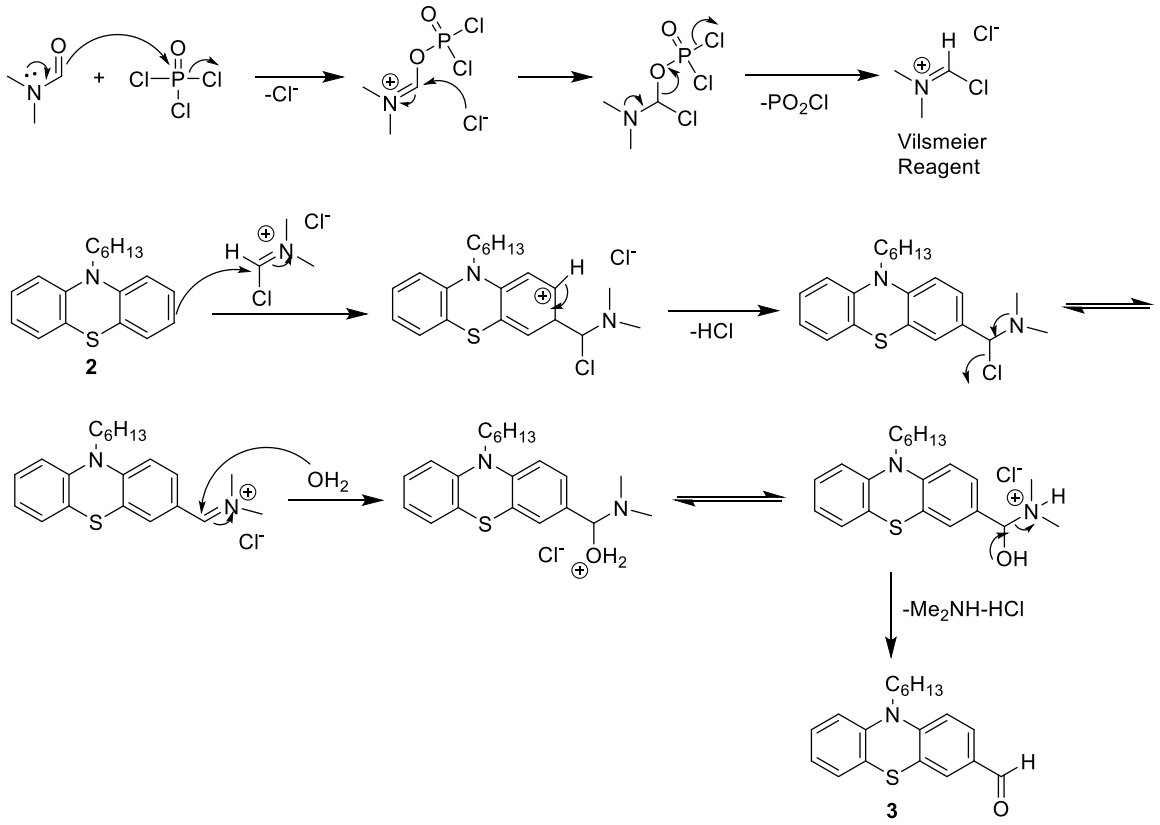

Scheme 2.8.2: Proposed mechanism for the Vilsmeier-Haack formylation of **2**.

2.8.3 Bromination

Bromination of aromatic compounds can be achieved through several different reagents, out of whom molecular bromine (Br_2) and N-bromosuccinimide (NBS) are the most commonly used.[42] NBS is often the preferred reagent compared to Br_2 due to its lower toxicity. NBS also produces a very low concentration of bromine, decreasing the possibility of unwanted di-bromination.[45] The reaction occurs through electrophilic aromatic substitution,[42] and the proposed mechanism is shown in **Scheme 2.8.3**.

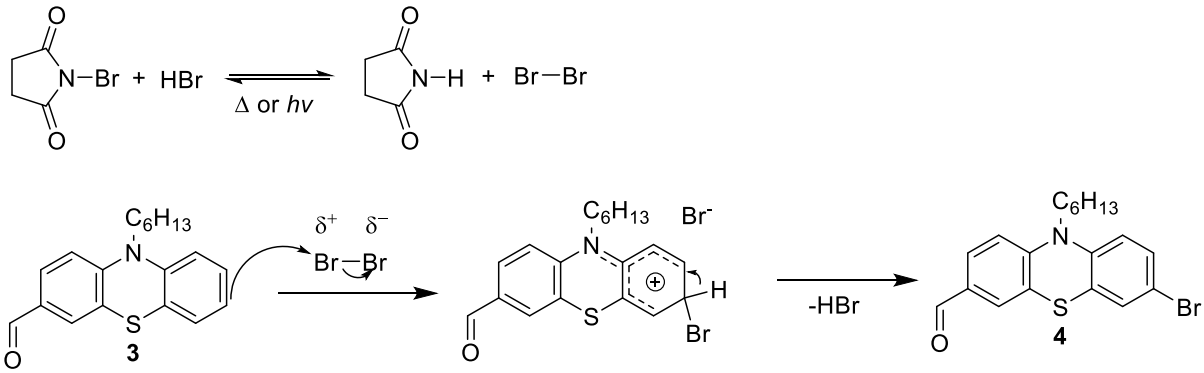

Scheme 2.8.3: Proposed mechanism for the bromination of **3** with NBS. The stabilizing effects through resonance of the lone pairs on the nitrogen is also shown.

2.8.4 Suzuki Cross-Coupling

The palladium-catalysed Suzuki cross-coupling between aryl halides and boronic acids/esters is a powerful synthetic tool for introducing new carbon-carbon bonds, and is an invaluable reaction in the synthesis of sensitizers due to their large conjugated carbon-based backbones.[3, 46] Other, non palladium-catalyzed, methodologies for introducing aryl-aryl bonds involves e.g. Grignard reagents, but these reactions involves harsh conditions and water-sensitive organometallic compounds which severely limits the substrate scope.[47] The proposed mechanism for the Suzuki cross-coupling is shown in **Scheme 2.8.4**.[48-50]

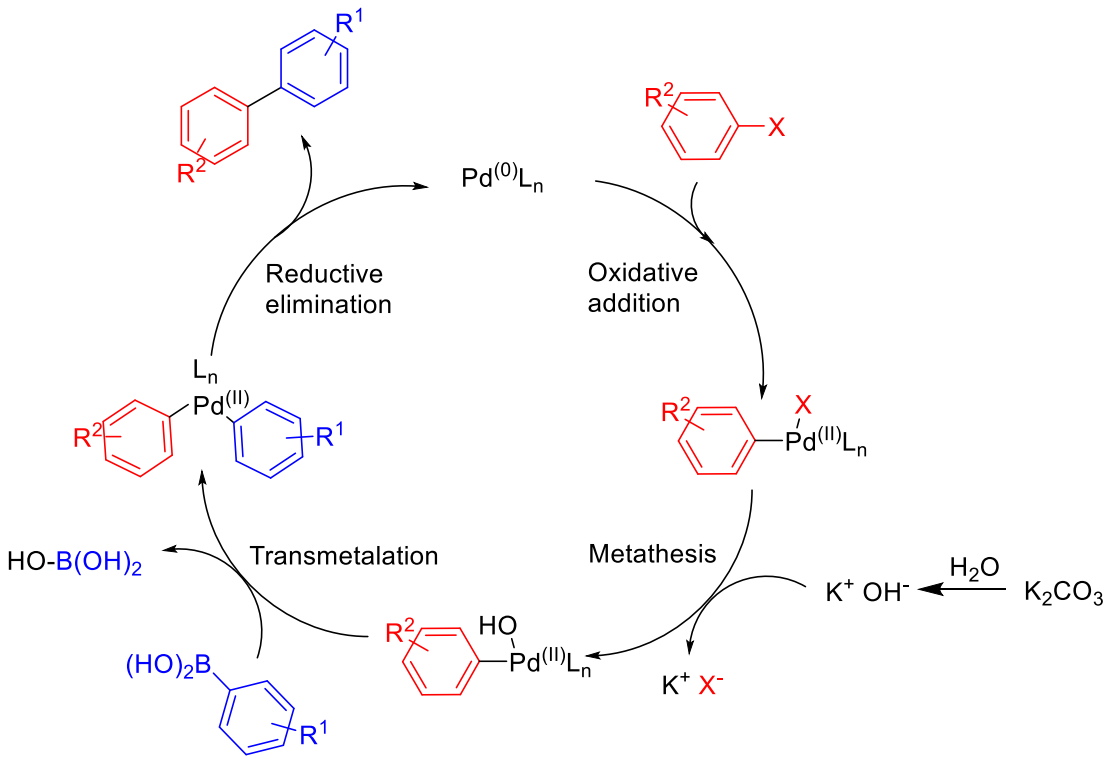

Scheme 2.8.4: The general catalytic cycle for Suzuki cross-coupling.

The catalytic cycle begins with oxidative addition of the aryl halide to the $Pd^{(0)}$ catalyst, generating a Pd^{II} complex. Oxidative addition is usually considered to be the rate-determining step in the catalytic cycle, but there are reports of reactions where transmetalation and reductive elimination are rate determining.[51] Oxidative addition favours weak C-X bonds (C-I > C-Br > C-Cl), and subsequent electron withdrawing groups on the aryl halide will accelerate this step.[3] Following oxidative addition the halide is substituted with an hydroxyl group in the metathesis step,[52] before the coupling partner is introduced to the Pd^{II}-complex via transmetalation. The rate of transmetalation is increased by electron-donating substituents on the boronic acid derivative.[53] Lastly, the aryl-aryl coupled product is formed by reductive elimination, regenerating the $Pd^{(0)}$ catalyst and initiating a new cycle.

2.8.5 Knoevenagel Condensation

The Knoevenagel condensation, first described by Emil Knoevenagel in 1898, is a nucleophilic addition between a carbonyl group and an active hydrogen compound in the presence of a catalytic amount of base.[54] The proposed reaction cycle for the Knoevenagel condensation of cyanoacetic acid as active hydrogen compound and **5** as carbonyl-bearing group with piperidine as catalytic base is shown in **Scheme 2.8.5**.[3]

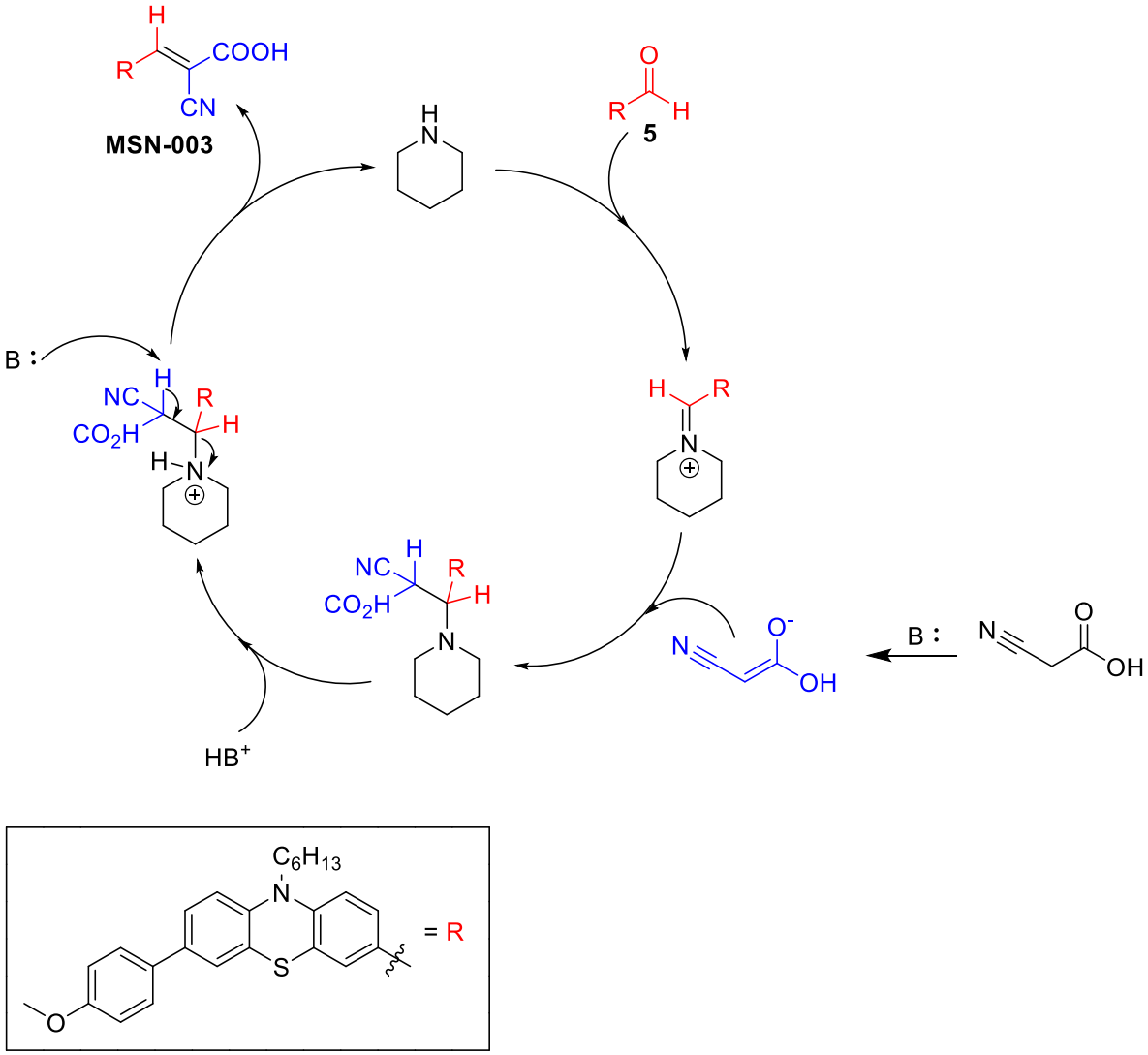

Scheme 2.8.5: Synthesis of **MSN-003** by Knoevenagel condensation of **5** and cyanoacetic acid in presence of piperidine as catalyst.

The reaction is initiated by the amine catalyst reacting with the carbonyl species forming an imminium ion intermediate. The base also deprotonates the active hydrogen compound forming a resonance stabilized enolate which attacks the imminium ion intermediate. The amine functionality of the intermediate is subsequently protonated while the active hydrogen derivative is deprotonated, initiating a rearrangement which releases the amine base, regenerates the catalyst and yields the final α,β-unsaturated product.

2.8.6 Cannizzaro Reaction

The Cannizzaro reaction is a base-induced disproportionation of two aldehyde molecules lacking α-protons to give a primary alcohol and carboxylic acid in a 1:1 ratio.[55] The reaction requires strongly alkaline conditions which limits the substrate scope, and aldehydes containing α-protons would be converted to their enolate counterparts and further reacted through aldol condensation. The proposed mechanism for the Cannizzaro reaction of **5** to obtain **MSN-004** is shown in **Scheme 2.8.6**.

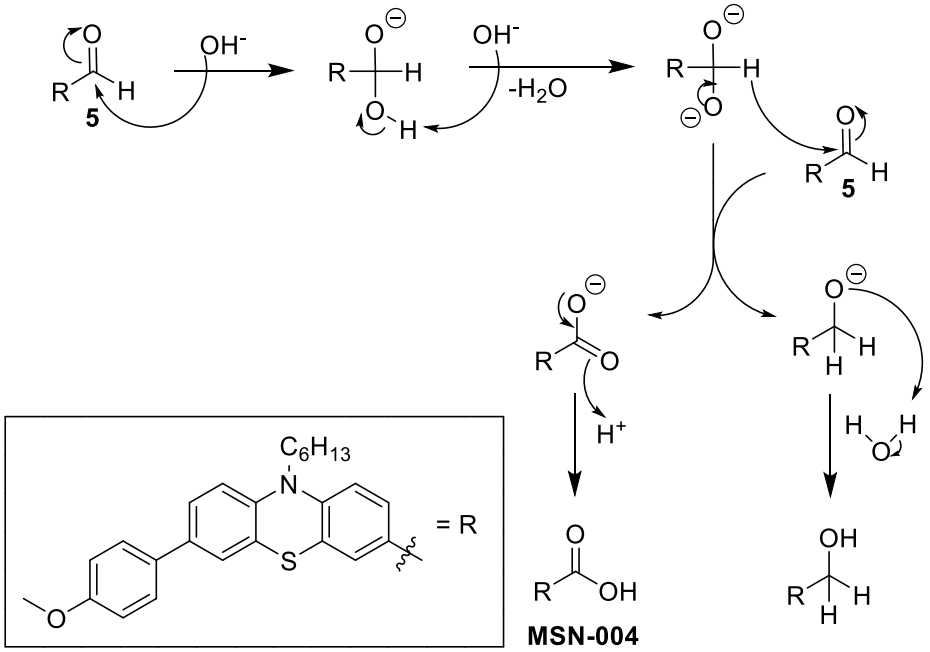

Scheme 2.8.6: Synthesis of **MSN-004** via the Cannizzaro reaction of **5**.

The reaction starts with hydroxide attack on the carbonyl group followed by deprotonation to give the di-anion intermediate. The unstable intermediate then collapses while releasing a hydride anion which attacks another carbonyl group, in what is considered to be the rate-determining step.[56] The carboxylate- and alkoxide ions are subsequently transformed to their respective carboxylic acid and primary alcohol by acquiring protons from the acidic work-up.

2.8.7 Stille Cross-Coupling

The Stille cross-coupling is a versatile alternative to the Suzuki cross-coupling, both employing palladium as catalyst, but differs from the Suzuki coupling by replacing the organoboron reagents with organostannanes. The advantages with the Stille coupling lie with its milder reaction conditions as there is no need for a base, making it more tolerant towards more sensitive functional groups. Organostannanes are also air stable, but tend to be highly toxic.[57] The proposed mechanism for the general catalytic cycle for Stille cross-coupling is shown in **Scheme 2.8.7**.[58]

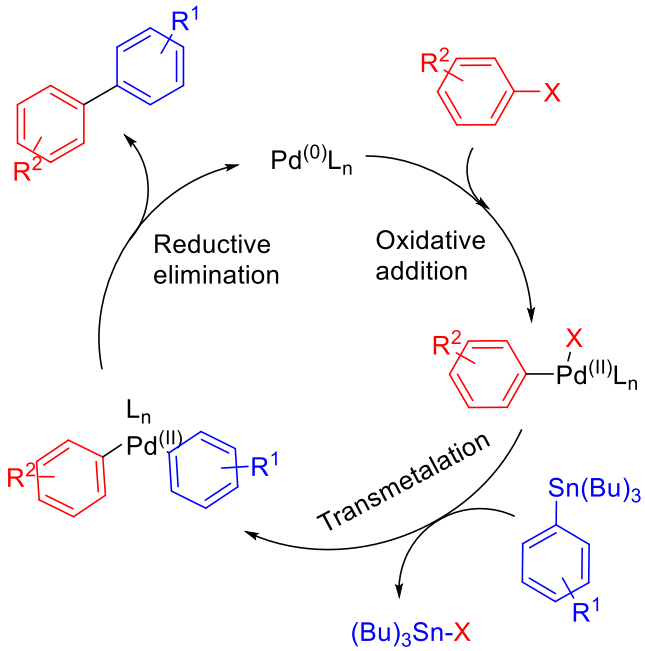

Scheme 2.8.7: The catalytic cycle for Stille cross-coupling.

The catalytic cycle begins, in the same way as with the Suzuki-coupling, with oxidative addition of the aryl halide to the $Pd^{(0)}$ catalyst, generating a Pd^{II} complex. As there is no base present the metathesis step does not occur. Following oxidative addition the transmetalation process takes place which introduces the coupling partner. In contrast to the Suzuki-coupling, transmetalation is widely considered to be the rate-determining step in the reaction.[59] The finished aryl-aryl compound is formed by reductive elimination as the final step, releasing the catalyst and initiating a new cycle.

In an effort to optimize the reaction it has been found that converting the organotin reagent to a more reactive organocopper intermediate by addition of copper(I)iodide increases the reaction rate.[58, 60] Further increase of reaction rate has been observed when adding a fluoride source, often in the form of caesium fluoride (CsF), as it would lead to the precipitation of $(Bu)_3Sn$-F, driving the equilibrium towards the more reactive organocopper intermediate.[58, 60] The proposed mechanism for the Copper(I)- and CsF effect in the Stille coupling is shown in **Scheme 2.8.8**.

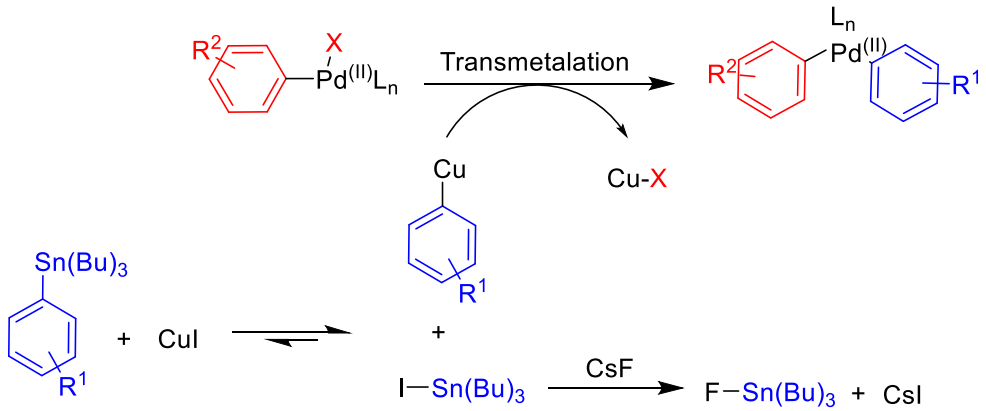

Scheme 2.8.8: Optimization of the transmetalation step in the Stille coupling by addition of copper(I)iodide and caesium fluoride.

3 Results and Discussion

3.1 General

Three novel dyes (**MSN-004**, **MSN-005** & **MSN-006**) and the reference dye **MSN-003** has been synthesized and are shown in **Fig. 2.10**. The synthesis of a fourth novel dye bearing a catechol anchoring group was started but could not be finished due to time constraints imposed by the covid-19 outbreak. A study of UV-Vis-absorption properties, dye loading and photovoltaic performance of **MSN-003**, **MSN-004** and **MSN-006** will be presented in Section 3.3 and 3.4. These analyses were not conducted on **MSN-005** due to covid-19 limiting access to the laboratories.

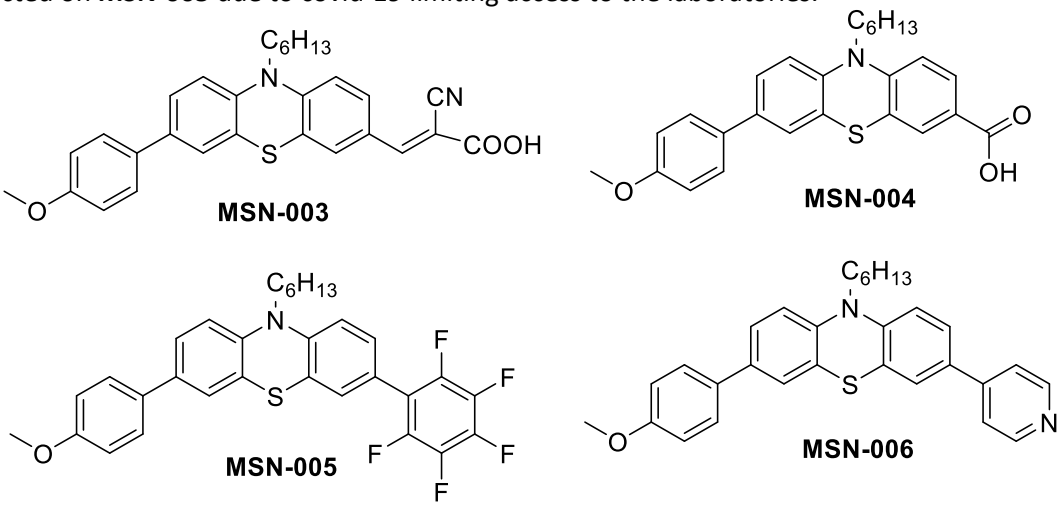

Figure 2.10: The target molecules synthesized.

3.2 Synthesis of MSN-003 – MSN-006

3.2.1 N-alkylation of Phenothiazine

The attachment of the *n*-C_6H_{13} anti-aggregating group on the N-10 position was successfully done via a nucleophilic aliphatic substitution reaction, shown in **Scheme 3.2.1**. Detailed reaction parameters are found in Section 7.2 and 7.6.

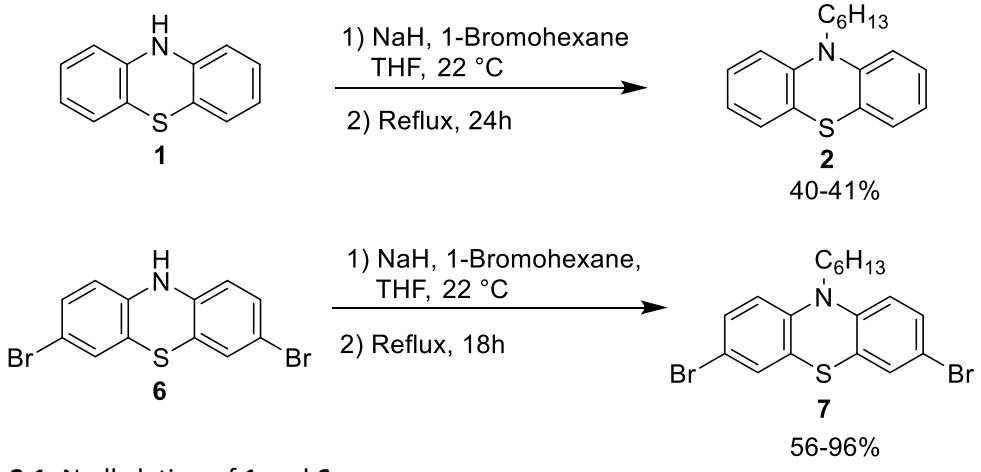

Scheme 3.2.1: N-alkylation of **1** and **6**.

The synthesis of **2** was done in 2 parallels with 41 and 40% yield, and **7** was similarly synthesized in two parallels with 56 and 96% yield following the procedure by Elkassih *et al.*[61] The yields of **7** were satisfactory, but the yields of **2** were considerably lower than the 72% reported in the literature.[62] The lower yields of **2** are most likely due to poor handling of solvents and chemicals. Even though a surplus of bromohexane and NaH was added, TLC did not indicate full conversion, most likely attributed to unwanted reaction between NaH and residual/atmospheric water. The formation of quaternary amine is also a possible side product, but is not expected to be a favourable product due to the steric hindrance of **2**. The potential quaternary amine salt would in either way be easily separated from the product by washing with water. The second synthesis of **7** afforded a yield superior to those reported in the literature (93%).

3.2.2 Formylation of Phenothiazine

Compound **3** was synthesized via a Vilsmeier-Haack formylation of **2** following a procedure by Hua *et al.*[63], shown in **Scheme 3.2.2**. Detailed reaction parameters are found in Section 7.3.

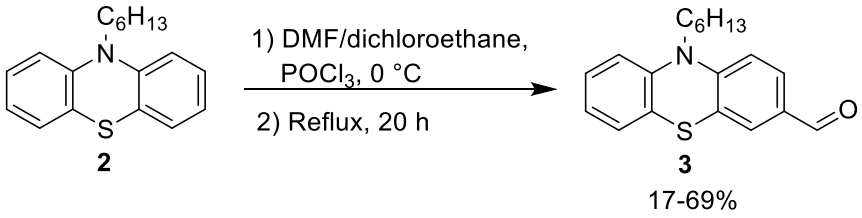

Scheme 3.2.2: Vilsmeier-Haack formylation of **2**.

The obtained yield from the first synthesis of **3** (17%) was somewhat lower than those previously reported in the literature (58-75%).[62, 63] This is attributed to poor solubility of the crude product in the solvent system (hexane: EtOAc, 9:1) used during purification, which led to some precipitation of the crude product on top of the column. This issue was addressed in the second synthesis where a more suitable eluent-system was adapted (EtOAc:petroleum ether, 1:4). Some solubility issues still persisted, but these problems were finally negated by dry loading the crude on Celite prior to purification. These improvements to the purification process afforded the product **3** in an acceptable yield of 69%.

3.2.3 Bromination of Phenothiazine

Compound **3** was successfully brominated to give compound **4** in good yields following the procedure of Hua *et al.*[63], shown in **Scheme 3.2.3**. Detailed reaction parameters can be found in Section 7.4. Compound **6** (see **Scheme 3.2.1**) had previously been made in large quantities by the research group, deeming it unnecessary to repeat the synthesis.

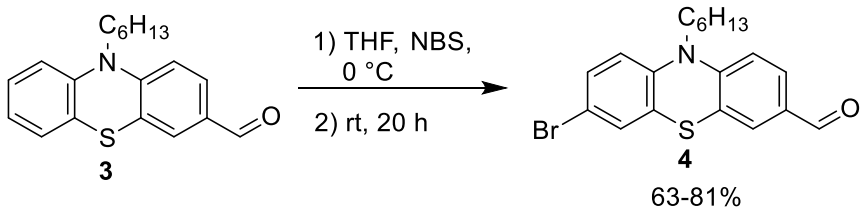

Scheme 3.2.3: Bromination of **3**.

By ensuring the purity of **3** prior to the bromination, the synthesis of **4** is a facile reaction. Both the nitrogen- and sulfur-atom are activating, *para*-directing substituents, however nitrogen has the strongest directing properties of the two.[3] This favours the electrophilic aromatic substitution of bromine on the 3- and 7- position, leaving only one possibility on **3**, as the other position is occupied by the aldehyde group. Compound **4** has previously been synthesised in yields of 68-89%.[27, 63]

3.2.4 Suzuki-Coupling of Donor Group on Phenothiazine

Commercially available 4-methoxyphenylboronic acid was attached onto phenothiazine via Suzuki cross-coupling to yield product **5** and **8** (**Scheme 3.2.4**), following the procedure by Buene *et al.*[27] The procedure is further described in Section 7.5 and 7.7.

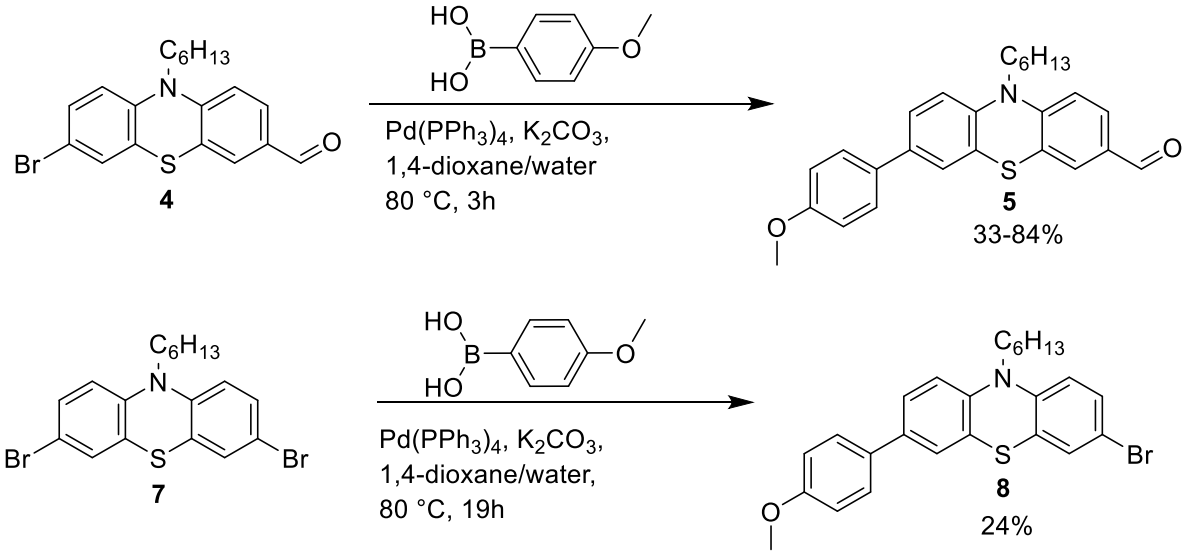

Scheme 3.2.4: Insertion of auxiliary donor-group via Suzuki cross-coupling for the synthesis of **5** and **8**.

In the synthesis of **8** the undesirable di-coupling of the donor group was observed. Difficulties in obtaining an eluent-system for efficient separation of the mono- and di-coupled product resulted in that the purification process (column chromatography) had to be repeated 3 times. This would have led to some mechanical loss which could explain the low yield compared to those reported in the literature (51%). The issue of di-coupling was not present in the synthesis of **5**, and the yields obtained more closely resembled those in the literature (64-89%).[27, 63]

3.2.5 Knoevenagel Condensation of Anchoring Group, Synthesis of MSN-003

The Knoevenagel condensation between **5** and cyanoacetic acid afforded the finished dye **MSN-003** in good yield, following the procedure of Buene *et al.*[27] Detailed reaction parameters are found in Section 7.8.

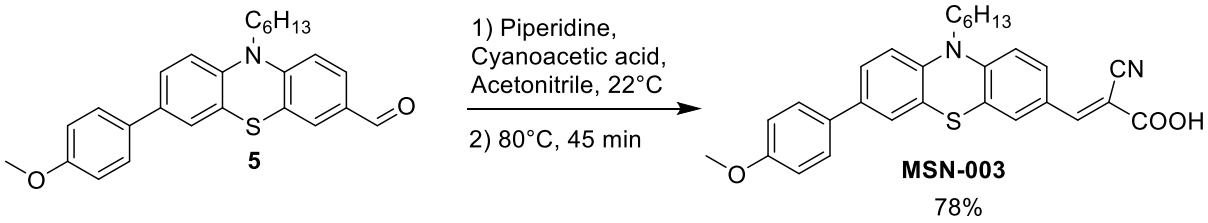

Scheme 3.2.5: The Knoevenagel condensation between **5** and cyanoacrylic acid.

The Knoevenagel condensation with cyanoacetic acid is a frequently used reaction in the field of DSSCs, as it is one of the most extensively used anchoring groups.[3, 6, 13, 63] It has also proven to be a reliable reaction with yields in the range of 67-99%.[3, 64, 65] The dye **MSN-003** was obtained in a yield of 78% without the need for further purification after extraction. This was possible by ensuring the purity of **5** prior to the reaction, limiting the possibility of unwanted side-reactions.

3.2.6 Oxidation of Aldehyde, Synthesis of MSN-004

The aldehyde group on compound **5** was oxidized to give the finished dye **MSN-004** via the Cannizzaro reaction, following a general procedure by Bejan *et al.*[66] The reaction procedure is described in Section 7.9.

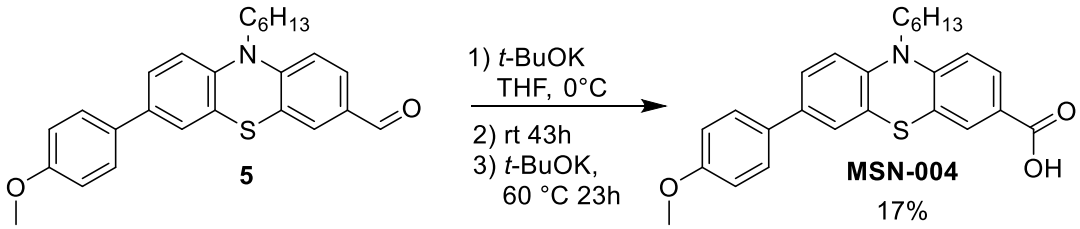

Scheme 3.2.6: Synthesis of **MSN-004** via the Cannizzaro reaction.

For the oxidation of **5** the use of more conventional oxidizing agents like potassium permanganate, hydrogen peroxide and chromic acid were deemed not suitable as it would lead to the unwanted oxidization of the sulphide.[67-69] The Cannizzaro reaction negates this issue by only being reactive on the aldehyde group. The reaction did however prove to be very slow-going as NMR-analysis of the reaction mixture indicated only 7% conversion after 18 hours. After an additional NMR-analysis indicating 14% conversion after a total of 43 hours it was decided to add additional base and increasing the reaction temperature, breaking from the general procedure described by Bejan *et al.* followed up to this point. This seemed to have a positive effect on the reaction rate as NMR indicated 37% conversion after an additional 23 hours, at which point it was decided to stop the reaction. When normalizing the obtained yield (17%) to the degree of conversion (37%) the reaction reached a theoretical yield of 46%. This is as expected as the reaction produces a 1:1 ratio of carboxylic acid and

primary alcohol. The primary alcohol by-product was isolated during purification and confirmed by NMR.

Optimization of the reaction was not attempted as the first synthesis produced a sufficient amount of dye for structural characterization and solar cell device fabrication. There are numerous experimental procedures using the Cannizzaro reaction on phenothiazine in the literature, differing in the choice of base and solvent.[70] The reaction has also shown to follow third-order kinetics, second order in aldehyde and first order in base.[71] This leaves room for optimization by altering the concentration and type of base and solvents for future work.

3.2.6 Stille-Coupling of Anchoring Group, Synthesis of MSN-005

The pentafluorophenyl (**9**) anchoring group was attempted attached onto compound **8** via Stille-coupling in three parallels. The first two attempts were unsuccessful, observing no product formation. Formation of the finished dye **MSN-005** was confirmed in the third attempt, albeit in a very low yield of 4%. Detailed reaction parameters are found in Section 7.10.

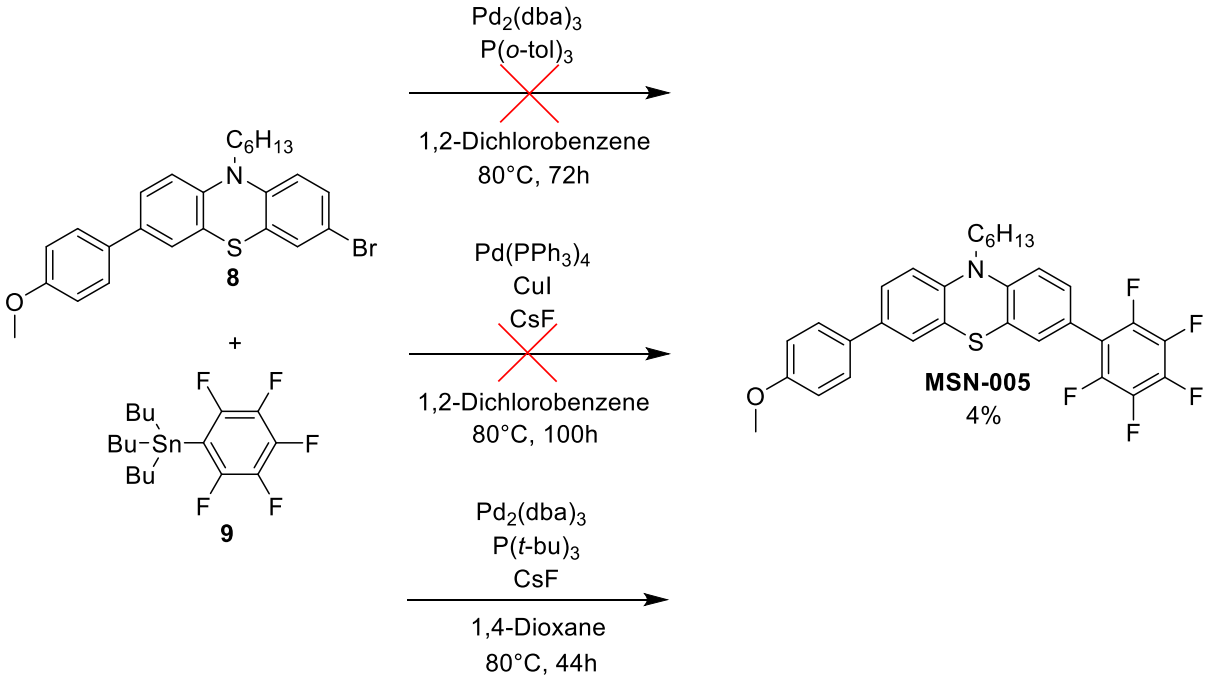

Scheme 3.2.6: Synthesis of **MSN-005** via Stille-coupling.

The reaction to synthesize **MSN-005** has not been reported previously, to the best of our knowledge. Reactions involving this specific Stille reagent **9** are very scarce in the literature where only one example of **9** being attached to an aryl-halide via Stille-conditions could be found (Martinelli *et al.*[72]). However, as the aryl-halide used in the aforementioned procedure was iodine, which is more reactive than the bromine on **8**,[73] it was determined to follow a general Stille-procedure by Gao *et al.*[74] involving bromine as halide.

Disappointingly no product was obtained following the procedure of Gao *et al.* TLC analysis after 72 hours indicated little activity as the reactant (**8**) spot was still very prominent. Confirming formation of **MSN-005** by NMR is facile as the ^{1}H-spectrum is expected to show similar splitting patterns to that

of the reactant **8** but will differ in having peaks in the ^{19}F-spectrum. After column chromatography 43% of the starting material (**8**) was recovered, and three additional fractions were analysed by ^{1}H- and ^{19}F- NMR. The spectra of these fractions were unintelligible, and the by-products could not be identified.

Seeing as Gao *et al.* obtained 85% yield after 48 hours it was apparent that the synthesis of **MSN-005** required different reaction conditions. For the second attempt the procedure of Mee *et al.*[58] was followed, with the exception of dichlorobenzene being used as solvent instead of DMF due to issues with solubility. The procedure of Mee *et al*. is very similar to that of Martinelli *et al.*, both utilizing the same kind of catalyst and copper(I)iodide as co-catalyst. However, it was reported in the same study that adding a fluorine source in the form of CsF gave a synergetic effect with the copper(I)iodide, further increasing the reaction rate, as described in Section 2.8.7. Nonetheless, these reaction parameters did not seem to be optimal for the synthesis as no product formation was observed. TLC- and NMR-analyses after 2.5 and 20 hours indicated little activity, and an UV-Vis analysis after 24 hours revealed no new absorption peaks. Additional reactant (**9**), solvent and catalyst were added after 27 hours in hope of increasing the reaction rate. 16% of the starting material (**8**) was recovered after purification, combined with two other fractions which could not be interpreted by NMR.

For the third attempt the procedure of Littke *et al.*[75] was followed, except for 1,4-dioxane being used as solvent instead of N-metyl-2-pyrrolidone (NMP). The procedure called for the same catalyst as the first parallel but differing in the choice of ligand, solvent and the addition of CsF. Littke *et al.* reported yields of 81-97% after 3-6 hours of reaction. After 44 hours TLC analysis of the reaction mixture, once again, indicated low conversion, and the reaction was stopped. NMR-analyses of the isolated fractions after purification did however confirm product formation, along with an identifiable by-product (substitution of hydrogen with bromine on **8**).

Finding reaction parameters for the successful Stille-coupling of **9** on **8** proved to be very challenging, and further efforts of optimization were not conducted due to time constraints. The role of the solvent has been shown to greatly affect the function of the catalysts,[58] and the choice to use different solvents than those listed in the literature procedure in the second and third parallel could have been a cause for the low reactivity. These difficulties are exemplified with a quote from Mitchell in a review of the Stille-reaction:[76]

> "A look at the catalyst (or to be exact, precatalyst) and cocatalyst combinations, together with solvent variations … will make it clear that there is in fact no 'ideal' system, but that each reaction will basically require optimization."

3.2.7 Suzuki-Coupling of Anchoring Group, Synthesis of MSN-006

The last step in the synthesis of **MSN-006** was completed by a Suzuki-coupling of 4-pyridinylboronic acid (**10**) onto **8**, following the general procedure by Buene *et al.*[27] Further reaction details are found in Section 7.11.

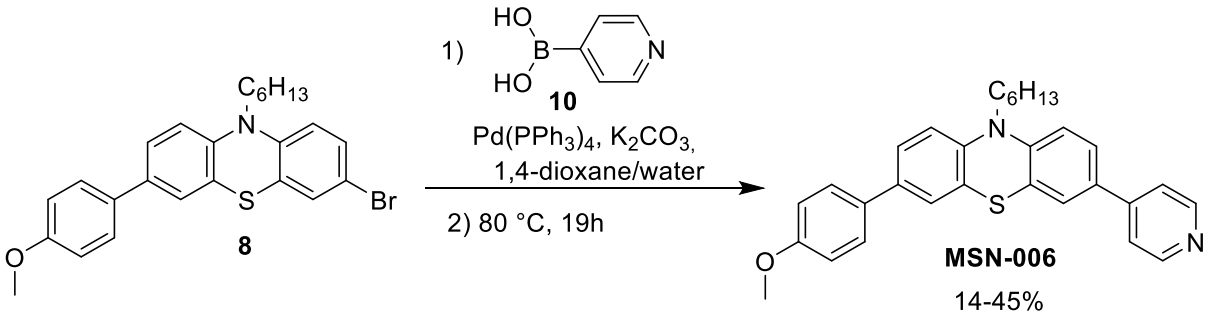

Scheme 3.2.7: Synthesis of **MSN-006** by Suzuki-coupling of boronic acid **10** onto **8**.

There are no previous reports in the literature of the pyridine group being directly connected onto the phenothiazine core, as in the case of **MSN-006**. Jia *et al.*[77] has produced a phenothiazine-based dye with pyridine as anchoring group, but with benzothiadiazole as π-spacer, utilizing a procedure identical to that of Buene *et al.* The Suzuki-cross coupling produced **MSN-006** in low to moderate yields where the first parallel obtained the product in 45% and the second parallel in 14%, compared to the 75% reported by Jia *et al.* It has been found that Suzuki-couplings involving nitrogen- and sulfur-heterocycles are especially challenging due to the instability of the compounds, either in the form of boronic acid derivative or aryl halide.[3, 78, 79]

The particularly low yield in the second synthesis can be explained by difficulties in purification as there was observed overlapping spots on the TLC after column chromatography. As these spots were superimposed on another further purification by column chromatography proved futile. However, some success of purifying the product was achieved by washing the crude with methanol, as the impurities appeared to have a somewhat higher solubility in methanol compared to the dye. This method did not remove all the impurities, and further purification was attempted by precipitation in acetonitrile. These combined efforts afforded **MSN-006** in appreciable purity, but at the cost of considerable mechanical loss of product.

The superimposed spots were also observed in the first synthesis, but further purification was not considered to be necessary due to NMR-spectra indicating high purity.

3.3 Characterization of the Dyes MSN-003 - MSN-006

3.3.1 Structural Characterization

The dyes **MSN-003** – **MSN-006** were identified using full spectroscopic characterization with ^{1}H- and ^{13}C NMR (in the case of **MSN-005** ^{19}F NMR analysis was also conducted), HSQC, HMBC, COSY, IR and HRMS. HRMS (**H**igh **R**esolution **M**ass **S**pectroscopy) was used to confirm formation of product, and IR was used for additional confirmation of product formation by studying characteristic absorption bands of functional groups.

NMR is the preferred spectroscopic tool for elucidating the chemical structures of the obtained products. The 1D experiments, ^{1}H-, ^{19}F and ^{13}C NMR, gives information about the chemical environment around each atom. The chemical shifts of each atom were determined by using the 2D techniques COSY, HSQC and HMBC. ^{1}H-^{1}H COSY (**CO**rrelated **S**pectroscop**Y**) indicates spin-spin coupling between adjacent protons and is a valuable tool to determine if a proton has neighbouring protons. ^{1}H-^{13}C HSQC (**H**eteronuclear **S**ingle **Q**uantum **C**oherence) provides correlation between

carbon atoms and their attached protons. ^{1}H-^{13}C HMBC (**H**eteronuclear **M**ultiple **B**ond **C**orrelation) shows coupling between protons and carbons separated by two to four bonds while suppressing one-bond correlations (HSQC).[80]

3.3.1.1 Identification of MSN-004

The HRMS spectrum (Appendix H.6) confirms formation of **MSN-004** with the predicted chemical formula $C_{26}H_{27}NO_3S$. IR (Appendix H.7) further confirms the desired product by indicating C=O stretch at 1683 cm^{-1}.[80]

This section will give a thorough walk-through for the structural elucidation of **MSN-004** by using NMR. **MSN-004** with numbered atoms is shown in **Fig. 3.3.1.1**, and the obtained shifts are summarized in **Table 3.3.2**. The structures of the remaining dyes were determined by using similar methodology as with **MSN-004**, but will not be expressed with the same amount of detail. The NMR spectra used for the subsequent elucidation are shown in Appendix H1-H5.

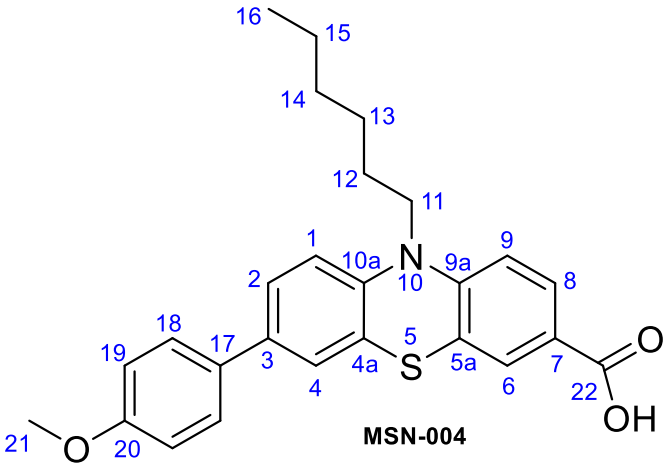

Figure 3.3.1.1: Finished chromophore **MSN-004** with numbered positions.

At δ_H 3.84 ppm the ^{1}H NMR spectrum indicates a singlet with integral of 3 which must correspond to H-21. C-21 was determined to have a chemical shift of δ_C 55.37 ppm by HSQC. The quaternary carbon C-20 was determined by HMBC as H-21 only revealed one long range coupling. The chemical shift of C-20 was determined to be δ_C 159.09 ppm.

Certain splitting patterns are expected when examining aromatic protons, and the measured coupling constants are a valuable tool for accurately determining the order of which they are arranged. **Table 3.3.1** shows the expected coupling constants for benzene and its derivatives.

Table 3.3.1: H,H coupling constants for benzene and its derivatives.[80]

J[Hz]	Benzene	Derivatives
J_o	7.5	7-9
J_m	1.4	1-3
J_p	0.7	< 1

The H-19 and H-18 protons show identical splitting (doublets), integral of 2, coupling constant of J_o 8.8 Hz and are located at δ_H 6.95 and 7.45 ppm. Their adjacency is further proven by COSY. By using HMBC and utilizing the fact that $^{3}J_{CH} > ^{2}J_{CH}$ in aromatic structures (see **Fig. 3.3.1.2**),[80] δ_H 7.45 ppm was

determined to be *meta* to C-20 (H-18) due to it having a stronger coupling compared to the proton at δ_H 6.95 ppm. This leaves the proton at δ_H 6.95 ppm to be assigned to H-19. The chemical shifts of the connected carbons (C-19 & C-18) were determined via HSQC to be δ_C 114.27 ppm and δ_C 127.56 ppm respectively. Using the same technique ($^3J_{CH}$>$^2J_{CH}$ in aromatic structures) C-17 was determined to have a shift of δ_C 132.29 ppm by observing $^3J_{CH}$ with H-19, and C-3 was found to be δ_C 136.14 ppm after observing $^3J_{CH}$ with H-18.

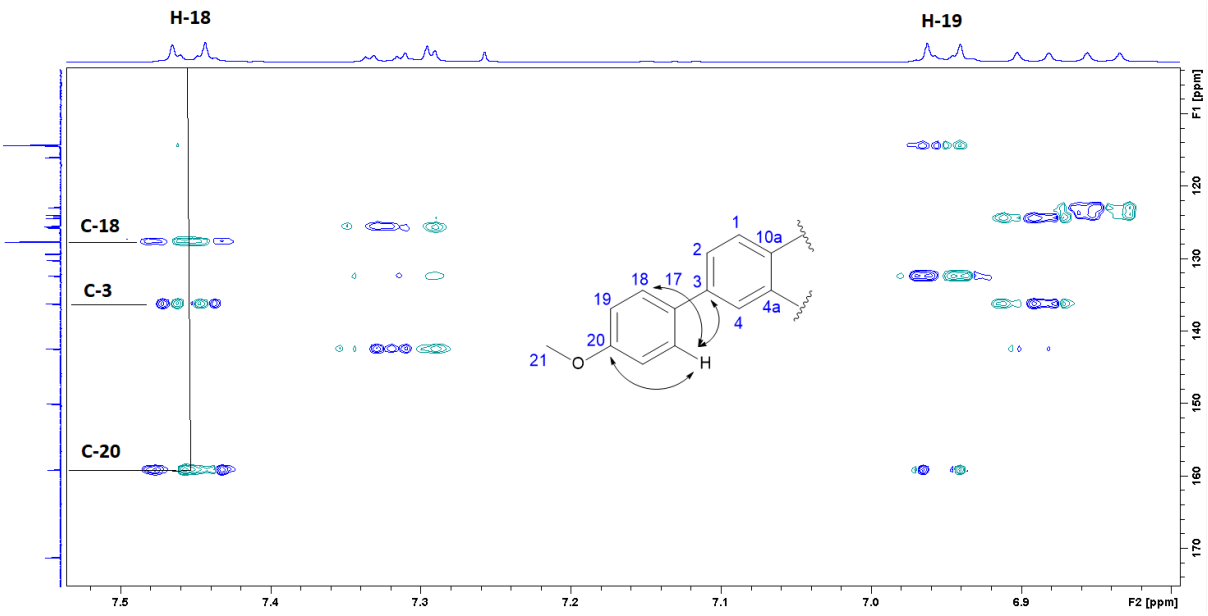

Figure 3.3.1.2: Showcasing the $^3J_{CH}$>$^2J_{CH}$ phenomenon for aromatic structures using HMBC.

From the HMBC spectra coupling with C-17 to the doublet of doublets at δ_H 7.32 ppm (J_o=8.4, J_m=2.1 Hz) and to the doublet at δ_H 7.29 ppm (J_m=2.1 Hz) can be observed, which must correspond to the H-2 and H-4 positions. As the shift at δ_H 7.32 ppm exhibits a doublet of doublets it needs to couple with two protons, and that can only be achieved at the H-2 position. This leaves δ_H 7.29 ppm to be placed at H-4. It can be observed in the HSQC spectrum that H-2 and H-4 correlates to δ_C 125.48 and δ_C 125.62 ppm, but a clear distinction of which proton that adheres to which carbon shift cannot be accurately deduced due to the limited resolution of the spectrum. Using COSY a correlation between H-2 and the doublet at δ_H 6.89 ppm (J_o=8.4 Hz) was found, confirming δ_H 6.89 ppm to be located at H-1 with corresponding δ_C 115.91 ppm.

Assigning the shifts on the n-hexyl chain is a facile process as the H-16 and H-11 positions are easily identifiable due to their multiplicity, integral and distinct shift. The COSY spectrum is additionally easily interpretable in this region, so no further in-depth explanation is given for the elucidation of these shifts.

By looking at the HMBC spectrum, H-11 couples to two carbon atoms in the aromatic region, δ_C 142.36 and δ_C 149.96 ppm. These positions must correlate to C-10a and C-9a. By observing a coupling of δ_C 142.36 ppm to H-1 ($^2J_{CH}$), H-2 ($^3J_{CH}$) and H-4 ($^3J_{CH}$) via HMBC it was determined that this shift belongs to position 10a, leaving δ_C 149.96 ppm for 9a. A coupling between H-1 and δ_C 124.30 ppm is also observed in HMBC, which must correlate to the $^3J_{CH}$-coupling to C-4a.

The H-6, H-8 and H-9 protons exhibit similar splitting patterns as H-4, H-2 and H-1, and their proton- and carbon shifts were determined by using results from HMBC, COSY and HSQC as previously shown. There was also measured a larger difference of δ_c for C-6 and C-8, allowing for their

respective protons to be determined accurately by HSQC. The remaining shifts belonging to the quaternary carbon atoms (C-5a, C-7 and C-8) were determined by HMBC. All carbon- and proton shifts, along with multiplicity, integral and coupling constants, are shown in **Table 3.3.2**.

Table 3.3.2: Chemical shifts along with coupling constants, integrals, and multiplicity for **MSN-004** assigned to the positions shown in **Fig. 3.3.1.1**.

Position in **Fig. 3.3.1.1**.	δ_H [ppm]	Multiplicity	Integral [#H]	*J*[Hz]	δ_C [ppm]
1	6.89	d	1	8.4	115.91
2	7.32	dd	1	2.1, 8.4	125.48 / 125.62
3	-	-	-	-	136.14
4	7.29	d	1	2.1	125.48 / 125.62
4a	-	-	-	-	124.30
5	-	-	-	-	-
5a	-	-	-	-	123.88
6	7.82	d	1	2.0	129.25
7	-			-	122.83
8	7.88	dd	1	2.0, 8.6	130.13
9	6.84	d	1	8.6	114.35
9a	-	-	-	-	149.96
10	-	-	-	-	-
10a	-	-	-	-	142.36
11	3.88	t	2	7.3	47.93
12	1.83	quint.	2	7.4	26.72
13	1.50-1.40	m	2	-	26.58
14	1.36-1.28	m	4	-	31.43
15	1.36-1.28	m	4	-	22.60
16	0.89	t	3	7.1	14.00
17	-	-	-	-	132.29
18	7.45	d	2	8.8	127.56
19	6.95	d	2	8.8	114.27
20	-	-	-	-	159.09
21	3.84	s	3	-	55.37
22	-	-	-	-	171.15

3.3.1.2 Identification of MSN-003

The HRMS spectrum (Appendix G.6) confirms formation of **MSN-003** with the predicted chemical formula $C_{29}H_{28}N_2O_3S$. IR (Appendix G.7) further confirms the desired product by indicating C≡N stretch at ~ 2200 cm^{-1} and C=O stretch at 1689 cm^{-1}.[80] The NMR spectra of **MSN-003** are shown in Appendix G.1-G.5, and the obtained shifts are presented in **Table 3.3.3**.

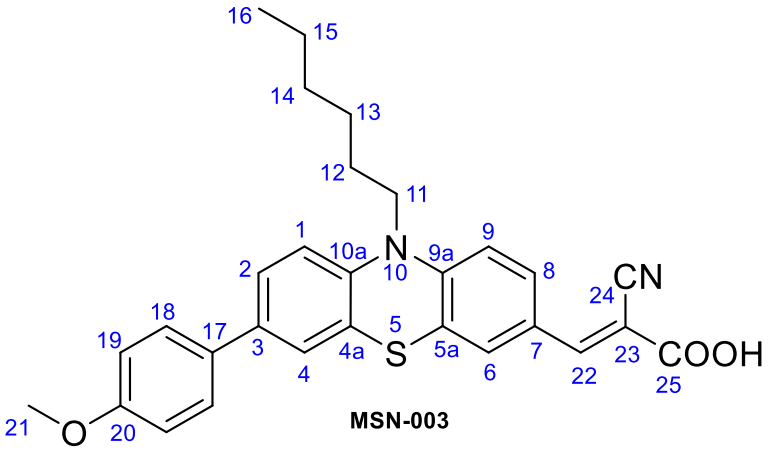

Figure 3.3.1.2: Finished chromophore **MSN-003** with numbered positions.

Table 3.3.3: Chemical shifts along with coupling constants, integrals and multiplicity for **MSN-003** assigned to the positions shown in **Fig. 3.3.1.2**.

Position in **Fig. 3.3.1.2**	δ_H [ppm]	Multiplicity	Integral [#H]	*J*[Hz]	δ_C [ppm]
1	7.16	d	1	8.5	116.02
2	7.51	dd	1	2.2, 8.5	124.88
3	-	-	-	-	134.63
4	7.46	d	1	2.2	123.91
4a	-	-	-	-	121.90
5	-	-	-	-	-
5a	-	-	-	-	122.08
6	7.88	d	1	2.1	128.41
7	-	-	-	-	124.81
8	7.97	dd	1	2.1, 8.7	130.99
9	7.21	d	1	8.7	114.85
9a	-	-	-	-	147.97
10	-	-	-	-	-
10a	-	-	-	-	140.52
11	4.01	t	2	7.1	46.29
12	1.76	quint.	2	7.7	25.39
13	1.49-1.43	m	2	-	25.03
14	1.36-1.28	m	4	-	30.13
15	1.36-1.28	m	4	-	21.41
16	0.89	t	3	6.9	13.16
17	-	-	-	-	130.26
18	7.63	d	2	8.8	126.56
19	7.04	d	2	8.8	113.68
20	-	-	-	-	158.16
21	3.84	s	3	-	54.50
22	8.21	s	1	-	151.80
23	-	-	-	-	98.85
24	-	-	-	-	116.17
25	13.78	s	1	-	163.12

3.3.1.3 Identification of MSN-006

The HRMS spectrum (Appendix J.6) confirms formation of **MSN-006** with the predicted chemical formula $C_{30}H_{30}N_2OS$. IR is not a suitable spectroscopic tool for confirming product formation as the pyridyl anchoring group is not expected to introduce any new absorption bands.

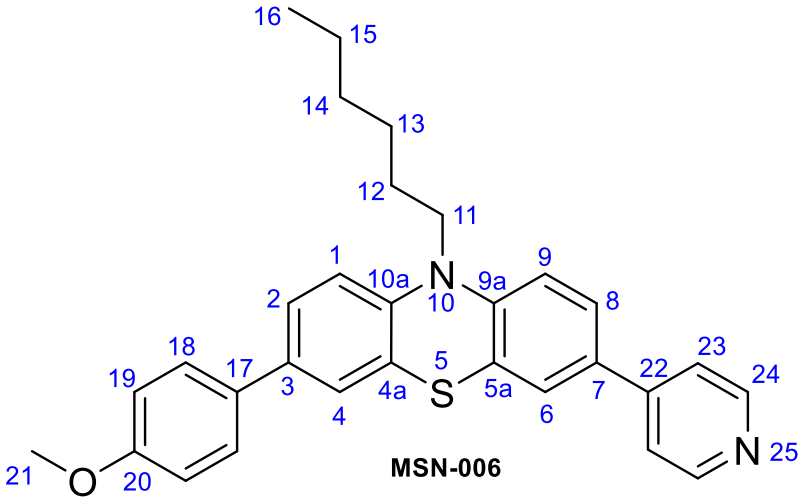

Figure 3.3.1.3: Finished chromophore **MSN-006** with numbered positions.

Due to the pyridyl group exhibiting comparable electronic properties to the methoxy-phenyl group, the resulting NMR spectra contain substantial overlap of signals. The ^{1}H NMR peaks from H-23 overlap with H-6 & H-8 masking the characteristic doublet of doublet and doublet expected from H-8 and H-6 respectively. The high degree of electronic symmetry of the molecule also led to difficulty in interpreting HSQC due to insufficient difference in δ_C. The position of δ_C 125.44, 125.57, 125.61 and 125.88 ppm could not be determined accurately, but are thought to correlate to C-2, C-4, C-6 and C-8. HSQC was also unable to differentiate C-1 and C-9. The obtainable chemical shifts for **MSN-006** are shown in **Table 3.3.4**, and the spectra used for the elucidation are found in Appendix J.1-J.5.

Table 3.3.4: Chemical shifts along with coupling constants, integrals, and multiplicity for **MSN-006** assigned to the positions shown in **Fig. 3.3.1.3**.

Position in **Fig. 3.3.1.3**.	δ_H [ppm]	Multiplicity	Integral [#H]	*J*[Hz]	δ_C [ppm]
1	6.88	d	1	8.3	115.62/115.46
2	7.34-7.31	m	2	-	-
3	-	-	-	-	135.58
4	7.34-7.31	m	2	-	-
4a	-	-	-	-	124.32
5	-	-	-	-	-
5a	-	-	-	-	125.19
6	7.44-7.39	m	4	-	-
7	-			-	131.82
8	7.44-7.39	m	4	-	-
9	6.90	d	1	8.4	115.62/115.46
9a	-	-	-	-	146.01
10	-	-	-	-	-
10a	-	-	-	-	143.14
11	3.87	t	2	7.2	47.65
12	1.83	quint.	2	7.4	26.79
13	1.49-1.42	m	2	-	26.63
14	1.36-1.28	m	4	-	31.45
15	1.36-1.28	m	4	-	22.60
16	0.88	t	3	6.9	13.99
17	-	-	-	-	132.42
18	7.45	d	2	8.7	127.51
19	6.94	d	2	8.7	114.23
20	-	-	-	-	159.00
21	3.83	s	3	-	55.32
22	-	-	-	-	146.94
23	7.44-7.39	m	4	-	120.70
24	8.60	d	2	6.0	150.24
25	-	-	-	-	-

3.3.1.4 Identification of MSN-005

The HRMS spectrum (Appendix I.7) confirms formation of **MSN-005** with the predicted chemical formula $C_{31}H_{26}NOF_5S$. The characteristic absorption bands due to C-F stretching is expected to appear in the range of 1000-1400 cm^{-1} which is already saturated with aromatic C=C and C-O absorption bands, making IR an unsuitable tool for spectroscopic identification of the compound.[80] The NMR spectra of **MSN-005** are shown in Appendix I.1-I.6, and the obtained shifts are presented in **Table 3.3.5**.

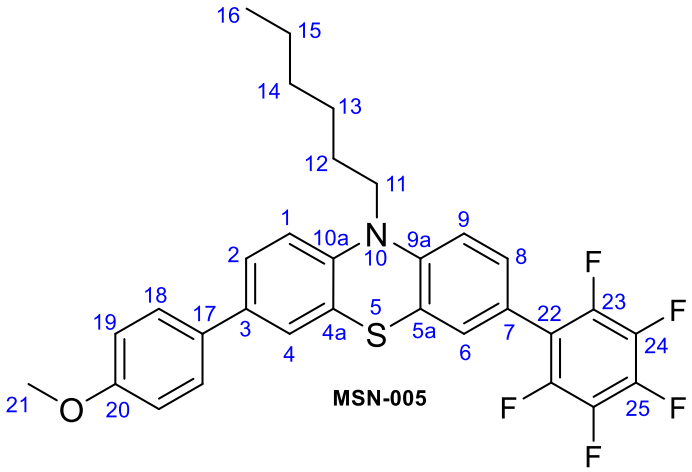

Figure 3.3.1.4: Finished chromophore **MSN-005** with numbered positions.

The C-23, C-24 and C-25 carbons were not detectable in the ^{13}C NMR spectrum due to decoupling taking place against ^{1}H. No $^{13}C\{^{19}F\}$ analyses were available on the NMR instruments, leaving these positions unable to be accounted for. There was also an overlap observed in the ^{1}H NMR spectrum in addition to a broadening of signals masking some of the expected splitting patterns. This led to only a partially structural elucidation being possible for **MSN-005**, shown in **Table 3.3.5**. During the elucidation the apparent multiplet in the ^{1}H NMR spectrum at δ_H 6.97-6.89 is treated as three individual doublets, as shown in **Fig. 3.3.1.5**. This is due to the dyes **MSN-004** and **MSN-006** showing similar splitting patterns, and this behaviour is also expected to occur for **MSN-005**. The existence of the H-9 doublet of **MSN-005** is further proven when interpreting HMBC as the three proton-signals can easily be distinguished from each other.

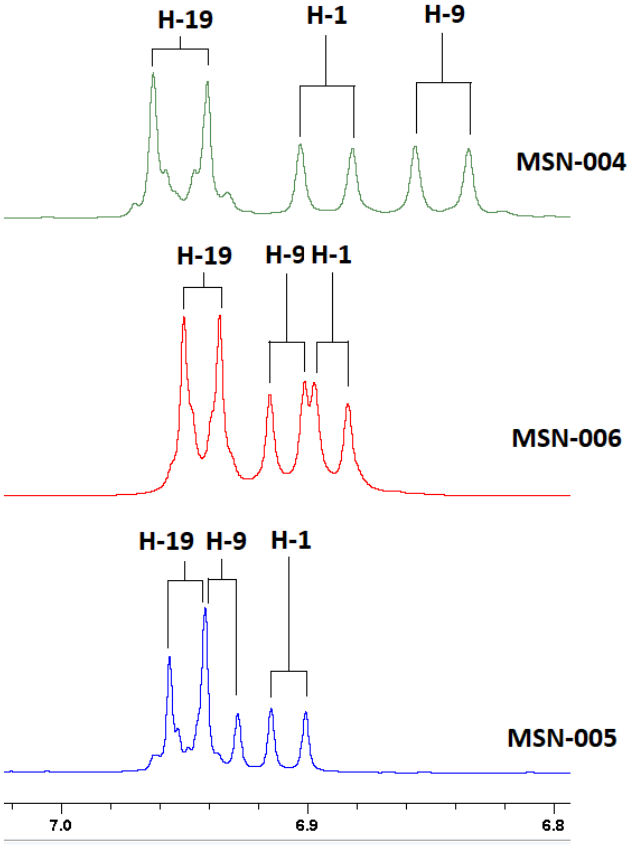

Figure 3.3.1.5: Showcasing the overlap of the H-9 and H-19 protons in the ^{1}H NMR of **MSN-005**.

Table 3.3.5: Chemical shifts along with coupling constants, integrals, and multiplicity for **MSN-005** assigned to the positions shown in **Fig. 3.3.1.4**.

Position in **Fig. 3.3.1.4**.	δ_H [ppm]	Multiplicity	Integral [#H]	*J*[Hz]	δ_C [ppm]
1	6.91	d	1	8.4	115.69
2	7.33	dd	1	2.2, 8.4	125.55/125.66
3	-	-	-	-	135.73
4	7.32	d	1	2.0	125.55/125.66
4a	-	-	-	-	124.46
5	-	-	-	-	-
5a	-	-	-	-	124.85
6	7.22-7.18	m	2	-	128.76/129.19
7	-	-	-	-	119.98
8	7.22-7.18	m	2	-	128.76/129.19
9	6.93	d	1	-	115.07
9a	-	-	-	-	146.12
10	-	-	-	-	-
10a	-	-	-	-	143.18
11	3.89	t	2	7.2	47.66
12	1.86	quint.	2	7.5	26.84
13	1.50-1.44	m	2	-	26.69
14	1.36-1.31	m	4	-	31.48
15	1.36-1.31	m	4	-	26.62
16	0.89	t	3	7.0	13.99
17	-	-	-	-	132.47
18	7.45	d	2	8.8	127.56
19	6.95	d	2	8.6	114.25
20	-	-	-	-	159.03
21	3.84	s	3	-	55.36
22	-	-	-	-	127.75
23	-	-	-	-	-
24	-	-	-	-	-
25	-	-	-	-	-

3.3.2 Optical Properties

The normalized UV-Vis absorption spectra for **MSN-003**, **MSN-004**, **MSN-005** and **MSN-006** shown in **Fig. 3.3.2.1** were obtained by measuring the dyes in DCM.

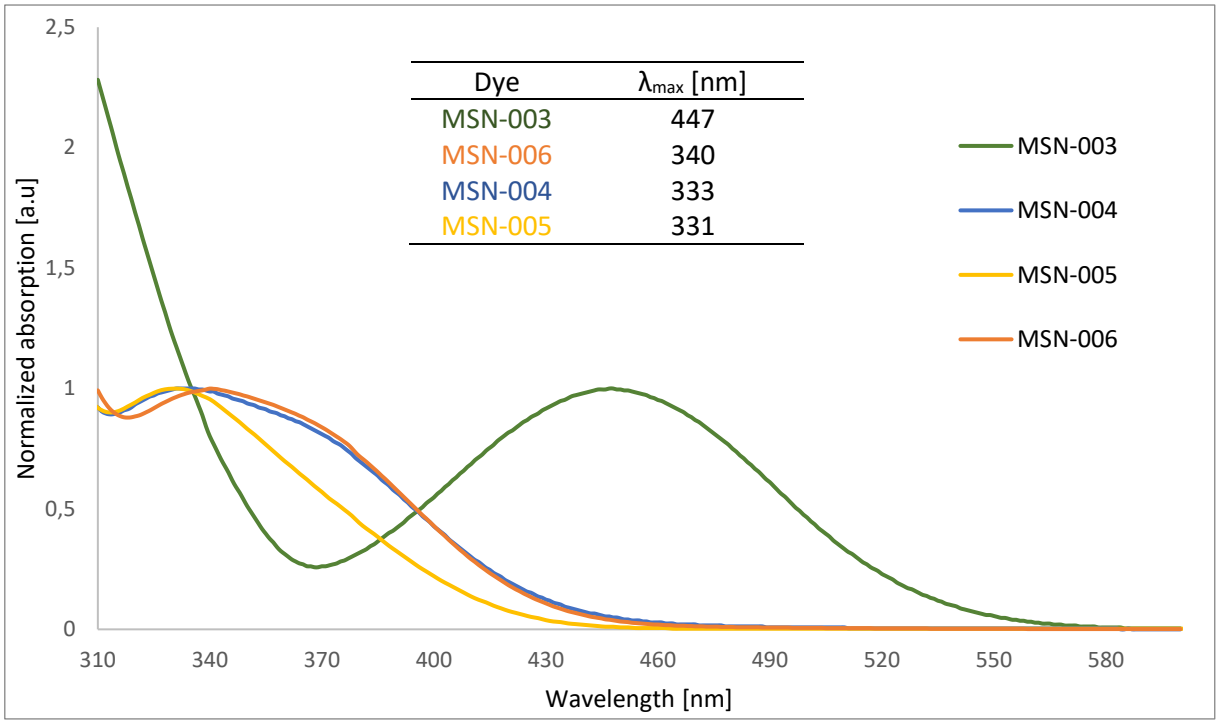

Figure 3.3.2.1: The normalized UV-Vis absorption spectra of **MSN-003** - **MSN-006** measured in DCM along with their respective absorption maxima.

The UV-Vis spectra of **MSN-003** is in accordance with previous reports by Buene *et al*.[27] The dyes **MSN-006** and **MSN-004** show remarkable similarities to each other with only 7 nm differing between the absorption maxima, and are also in stark contrast to **MSN-003** by being severely blue-shifted. Such amount of hypsochromic shift is not desirable for DSSCs as the photon flux in the solar spectrum rises with increasing wavelength (see **Fig. 2.1**), and the resulting blue shift will ultimately decrease the performance of the solar cell.

The large difference of absorption maxima between **MSN-004** and **MSN-003** is especially surprising due to the similarities of the anchoring groups. In addition to the cyano-group, **MSN-003** differs with **MSN-004** only by having an extra double bond extending the anchoring group. Although not considered to be a π-spacer, the double bond does extend the conjugation between the donor- and acceptor groups and might facilitate better electron transport and light harvesting properties (also orbital mixing helps). This is further supported by **MSN-006** which also lacks the extra extension of anchoring group and displays similar absorption to that of **MSN-004**, while at the same time having a vastly different anchoring group with ~twice the Hammett value compared to **MSN-004**.[81, 82] The pyridyl group of **MSN-006** has an expected absorbance maximum of 250-260 nm and is not visible in **Fig. 3.3.2.1**.[83]

3.3.3 Electrochemical Properties

Cyclic voltammetry was carried out to determine whether the anchoring group would affect the energy levels of the dyes. Since none of the dyes possess any film forming properties, all the measurements were carried out in solution. The voltammograms are presented in **Fig. 3.3.3.1**

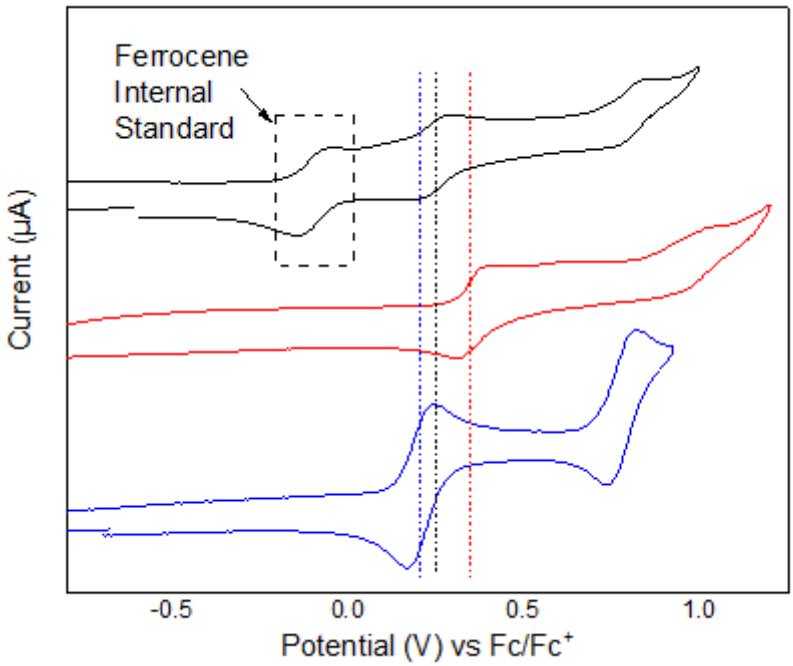

Figure 3.3.3.1: Representative cyclic voltammograms of **MSN-006** (black), **MSN-005** (blue) and **MSN-004** (red) in solution (dry acetonitrile, 0.1 M $TBAPF_6$). Scan rate: 100 mV/s. The colored dashed lines aid in the visualization of the differences for the $E_{1/2}$ of the oxidation processes.

All the dyes exhibit a reversible oxidation process, characteristic of the phenothiazine moiety. In the case of **MSN-004** the $E_{1/2}$ lies at 0.44 V and is the one that requires the most energy in order to be oxidized. The most easily oxidized dye is **MSN-005** with an $E_{1/2}$ = 0.31 V, while **MSN-006** lies in the middle with an $E_{1/2}$ = 0.34 V. The $E_{1/2}$ values can be used to calculate the HOMO of the molecule which can be found by the empirical equation:

$$E_{HOMO} = 5.1 + E_{ox} \quad (3.1)$$

The LUMO of the dyes can be calculated by obtaining the optical bandgap ($E_{o\text{-}o}$) from the UV-Vis measurements and subtracting it from the HOMO value since these are linked by the following equation:

$$E_{HOMO} - E_{LUMO} = E_{0\text{-}0} \quad (3.2)$$

As expected, the variation of the anchoring chain results in small changes to the energy levels. This does not allow for any definitive trends to be extracted concerning the effect that the three electron accepting anchoring units have to the ionization potential.

The results are summarized in **Table 3.3.3**, and the position of the HOMO- and LUMO levels for the dyes relative to the energy levels of the electrolyte and semiconductor is illustrated in **Fig. 3.3.3.2**.

Table 3.3.3: Electrochemical properties of the dyes **MSN-003** – **MSN-006** obtained via cyclic voltammetry and UV-Vis.

Dye	E_{HOMO} vs. NHE [V]	$E_{0\text{-}0}$ [eV][a]	E_{LUMO} vs. NHE [V][b]
MSN-003	0.88[c]	2.29	-1.41
MSN-004	1.04	2.81	-1.77
MSN-005	0.91	2.95	-2.04
MSN-006	0.94	2.72	-1.78

[a] Band gap energy estimated by UV-Vis spectroscopy

[b] Estimated value by using $E_{HOMO} - E_{LUMO} = E_{0\text{-}0}$

[c] Previously measured value by Buene *et al.*[62]

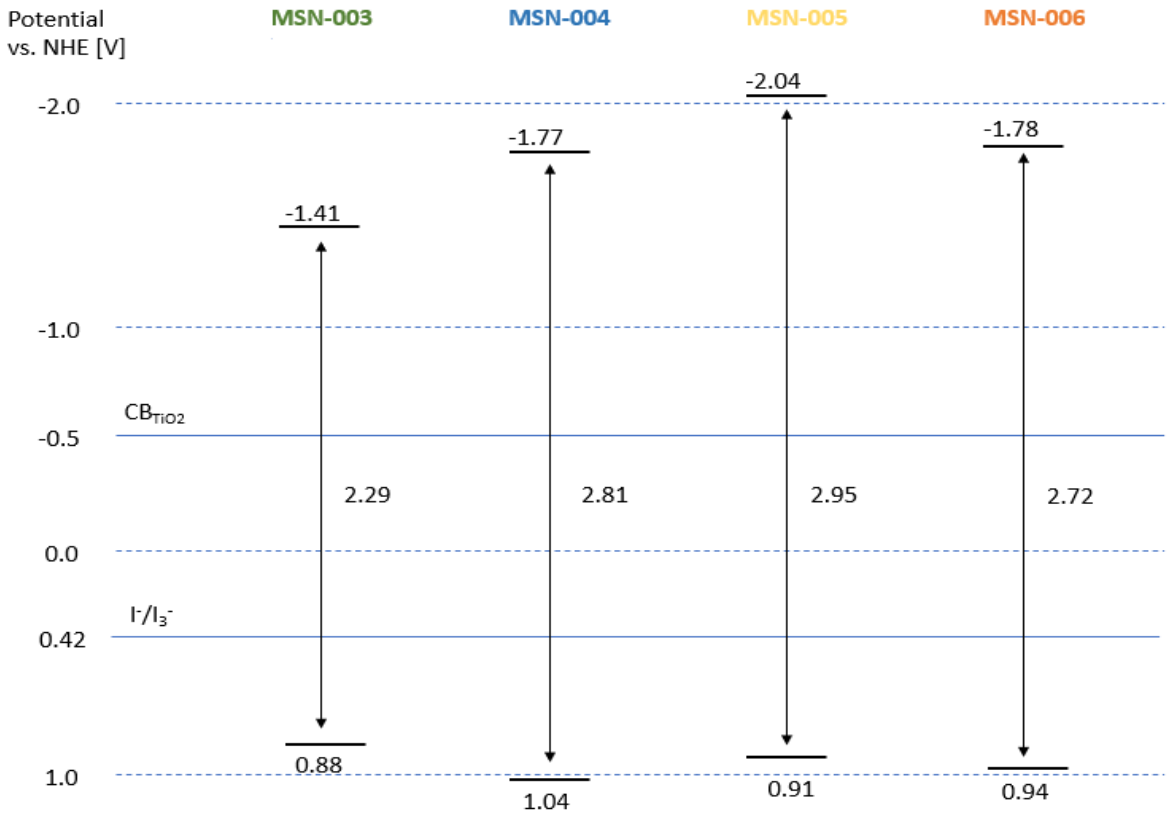

Figure 3.3.3.2: HOMO- and LUMO levels of the synthesized dyes along with the energy levels for the conductive band of the TiO_2 semiconductor and redox potential of the electrolyte.

As seen in **Fig. 3.3.3.2**, altering the anchoring groups affects the LUMO level of the chromophore in a larger degree than the HOMO level, which is as expected (Section 2.3). The increased band gap energy of **MSN-004** – **MSN-006** accounts for the bathochromic shift of absorption shown in **Fig. 3.3.2.1** when comparing to **MSN-003**.

3.4 Device Fabrication

3.4.1 Anchoring Effects on TiO_2

The UV-Vis absorption spectra of **MSN-003**, **MSN-004** and **MSN-006** in solution (DCM) and when adsorbed onto TiO_2 (with and without the anti-aggregating co-adsorbent CDCA) is shown in **Fig. 3.4.1**, and the measured values are summarized in **Table 3.4.1**.

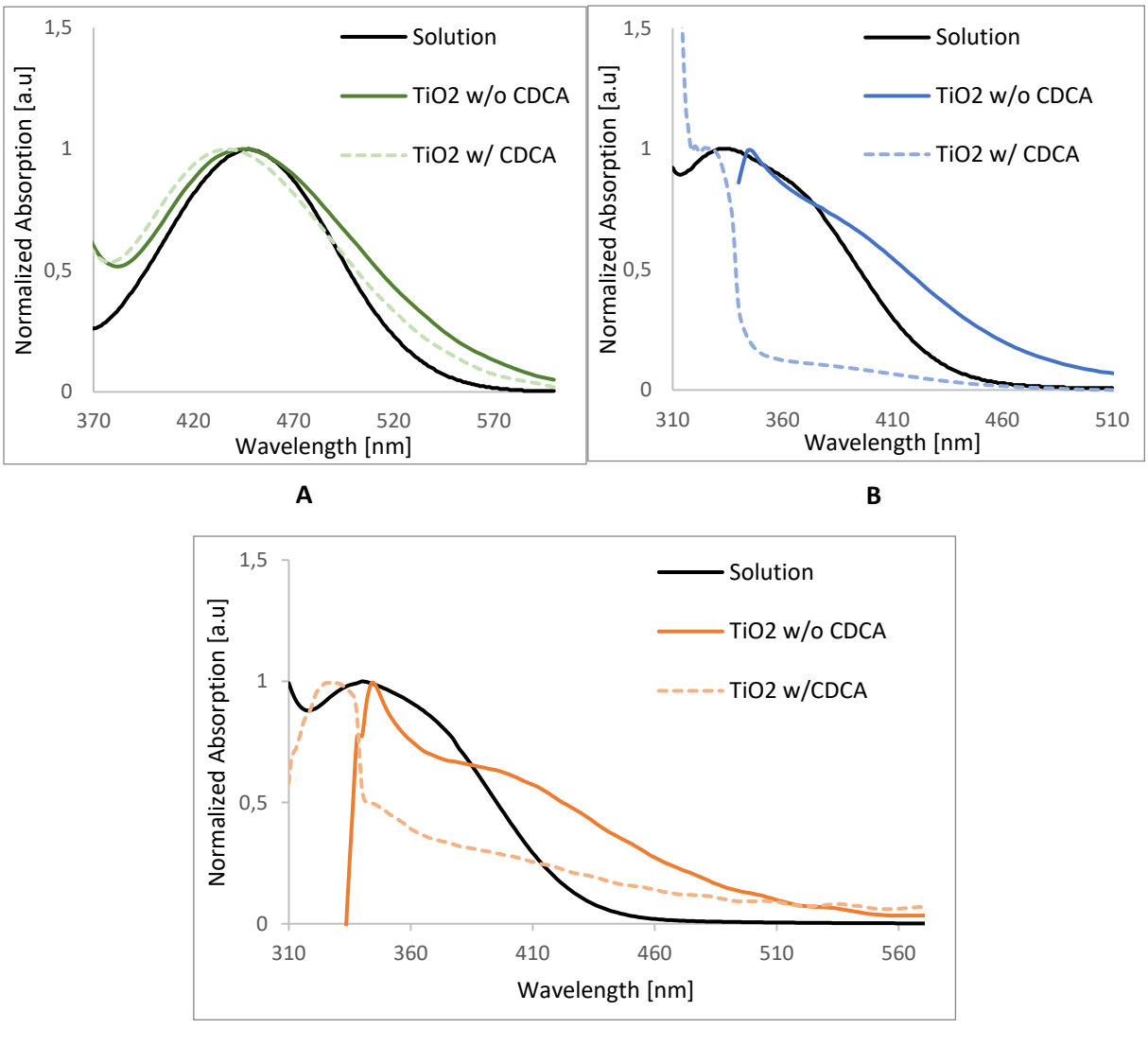

Figure 3.4.1: UV-Vis absorption spectra of **MSN-003** (**A**), **MSN-004** (**B**) and **MSN-006** (**C**) in solution (DCM) and when adsorbed onto TiO_2 (with and without CDCA).

Table 3.4.1: UV-Vis measurements of the dyes **MSN-003**, **MSN-004** and **MSN-006** in solution (DCM) and while adsorbed onto TiO_2 (with and without CDCA).

Dye	λ_{max} solution [nm]	λ_{max} TiO_2 w/CDCA [nm]	λ_{max} TiO_2 w/o CDCA [nm]	λ_{max} solution - λ_{max} TiO_2 w/ CDCA [nm]	λ_{max} solution - λ_{max} TiO_2 w/o CDCA [nm]
MSN-003	447	437	446	10	1
MSN-006	340	328	345	12	-5
MSN-004	333	325	345	8	-12

As can be seen in **Table 3.4.1** all the dyes exhibit a hypsochromic shift of absorption maxima when adsorbed onto the TiO_2 surface when CDCA is present, where the largest shift is measured for **MSN-006**. The high blue-shift of **MSN-006** is likely attributed to the pyridyl anchoring group offering extra π-π stacking interactions leading to increased H-aggregation. However, without the addition of CDCA the dyes **MSN-006** and **MSN-004** switch to a bathochromic shift of absorption, whereas **MSN-003** still maintains a blue-shift, albeit considerably reduced. **MSN-006** experiences a lower degree of red-shift than **MSN-004**, again, likely due to π-π stacking interactions of the aromatic anchoring group leading to some H-aggregation.

In order to investigate the relative bonding strength of the different anchoring groups on the TiO_2 surface a test was developed where UV-Vis absorption was measured as a function of staining time of the TiO_2 electrode. The test was conducted both with and without the addition of CDCA (10:1 CDCA:dye) in order to extrapolate its significance on the anchoring process of the dyes. The results are shown in **Fig. 3.4.2**. The procedure is further explained in Section 7.14.

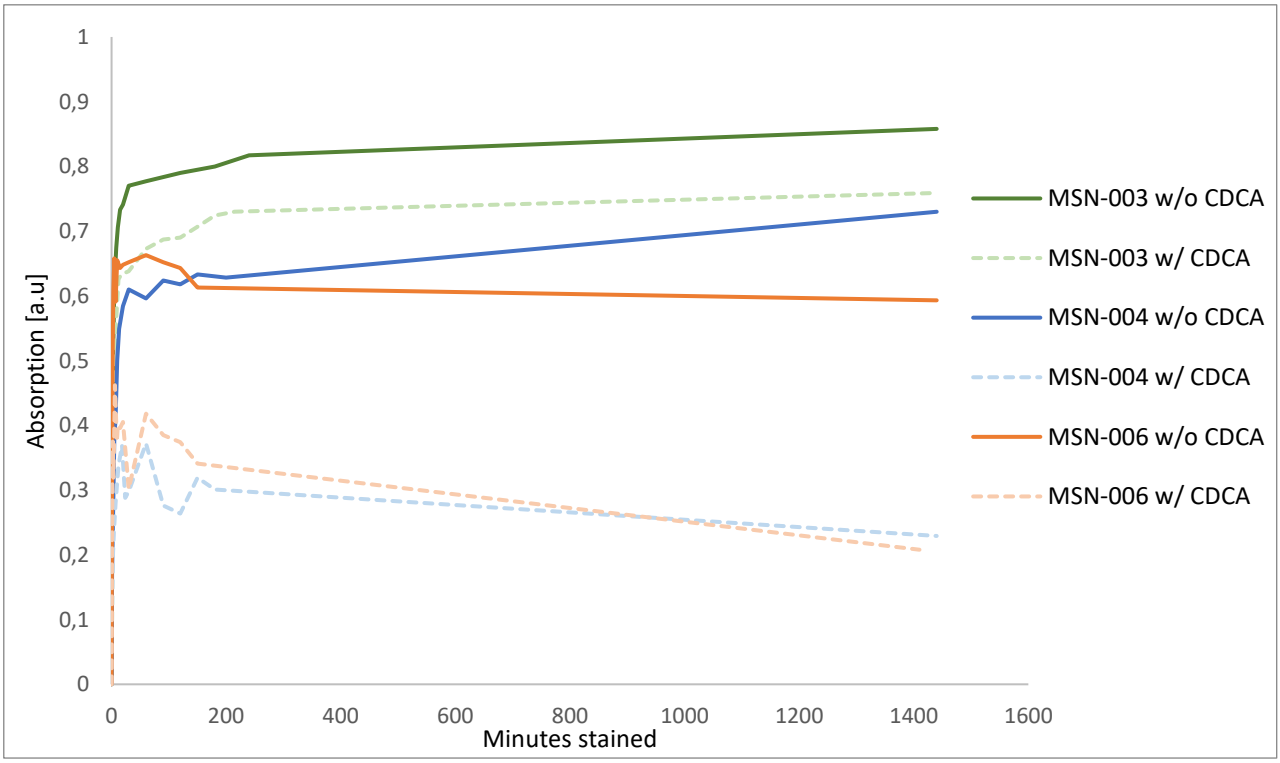

Figure 3.4.2: UV-Vis absorption of the dyes **MSN-003**, **MSN-004** and **MSN-006** when adsorbed onto TiO_2 as function of staining time.

By examining **Fig. 3.4.2** it becomes apparent that the initial adsorption rate of the dyes on the TiO_2 surface is very high as ~90% peak absorption intensity is reached after ~20 minutes staining time. A higher absorption intensity is also measured for all the dyes when no CDCA is added. The CDCA competes with the dye molecules on the TiO_2 surface while not contributing to any absorption in the UV-Vis spectrum, leading to an expected decrease of absorption intensity.

One unexpected trend which was observed was the decrease of absorption intensity of **MSN-004** and **MSN-006** as the staining time increased when CDCA was present. This might indicate that the binding nature of these anchoring groups are of a reversible character, and that CDCA has a stronger binding affinity towards TiO_2 and displaces the dye molecules over time. When performing the staining procedure without CDCA the measured absorption intensity was more than doubled for **MSN-004** and **MSN-006** which further illustrates the preferential adsorption of CDCA. This trend is not observed for **MSN-003**, indicating a stronger and more stable bond when comparing to CDCA, **MSN-004** and **MSN-006**.

In addition to measuring the absorption intensity, the absorption maximum (λ_{max}) was also analysed as a function of staining time in order to identify a correlation between H-/J-aggregation, staining time and CDCA's efficiency of inhibiting said aggregates. These results are shown in **Fig. 3.4.3** – **3.4.5**.

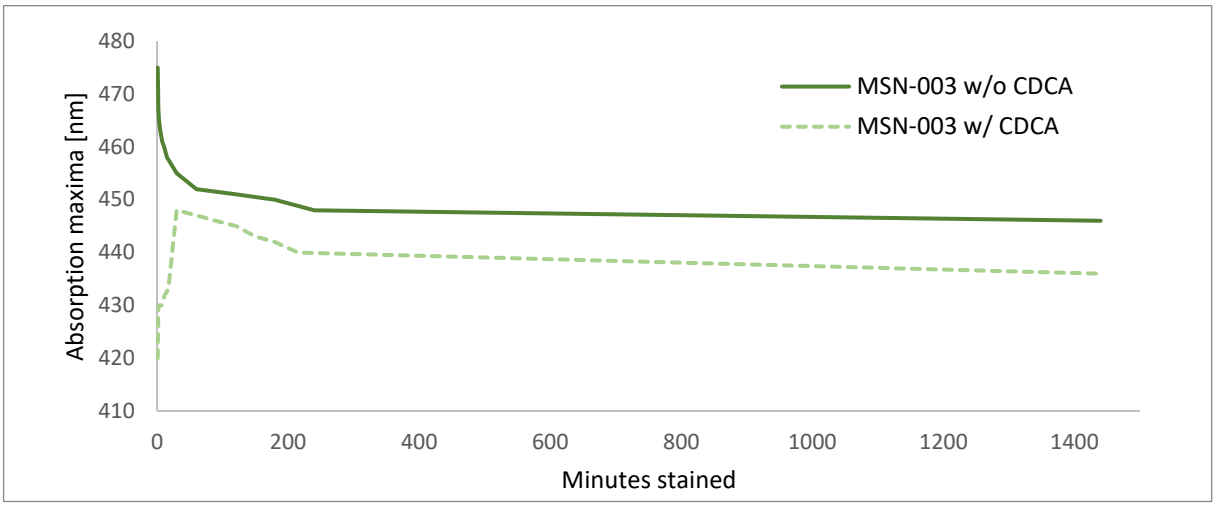

Figure 3.4.3: Absorption maxima measured as function of staining time of **MSN-003** on TiO_2 with and without the addition of CDCA.

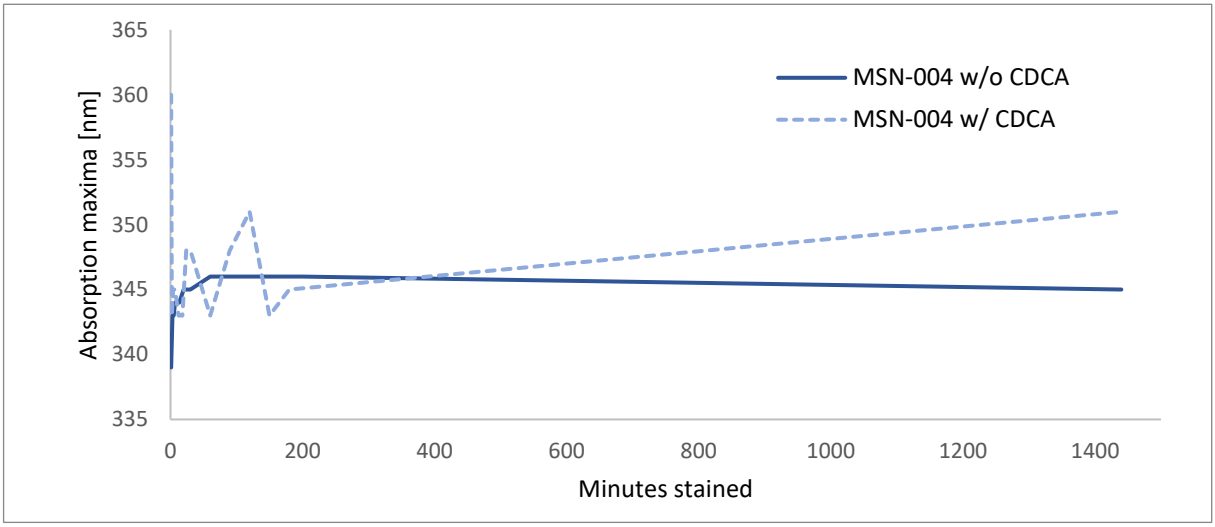

Figure 3.4.4: Absorption maxima measured as function of staining time of **MSN-004** on TiO_2 with and without the addition of CDCA.

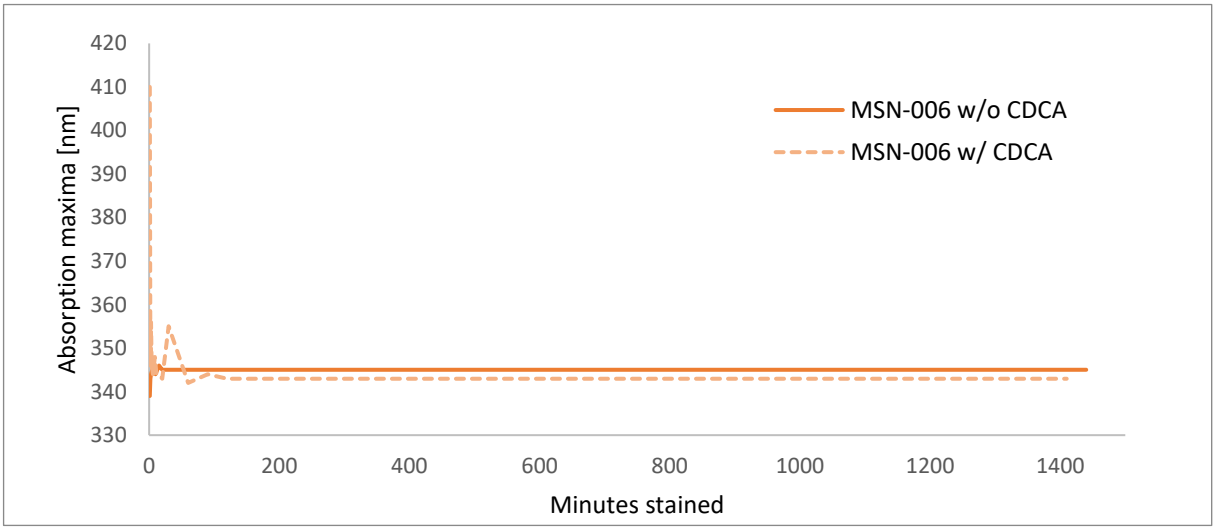

Figure 3.4.5: Absorption maxima measured as function of staining time of **MSN-006** on TiO_2 with and without the addition of CDCA

A common trend is observed for all the dyes where the initial absorption maxima with and without CDCA is either considerably blue- or red-shifted and further normalizes to an in-between absorption maximum as the staining time increases. For **MSN-004** and **MSN-006** an increasing red-shift can be measured when no CDCA is added, indicating that these dyes are more prone to J-aggregation. The opposite effect can be seen for **MSN-003** where a decrease of absorption maxima is observed without the addition of CDCA, indicating a preferential formation of H-aggregates. These trends are highlighted in **Fig. 3.4.6**.

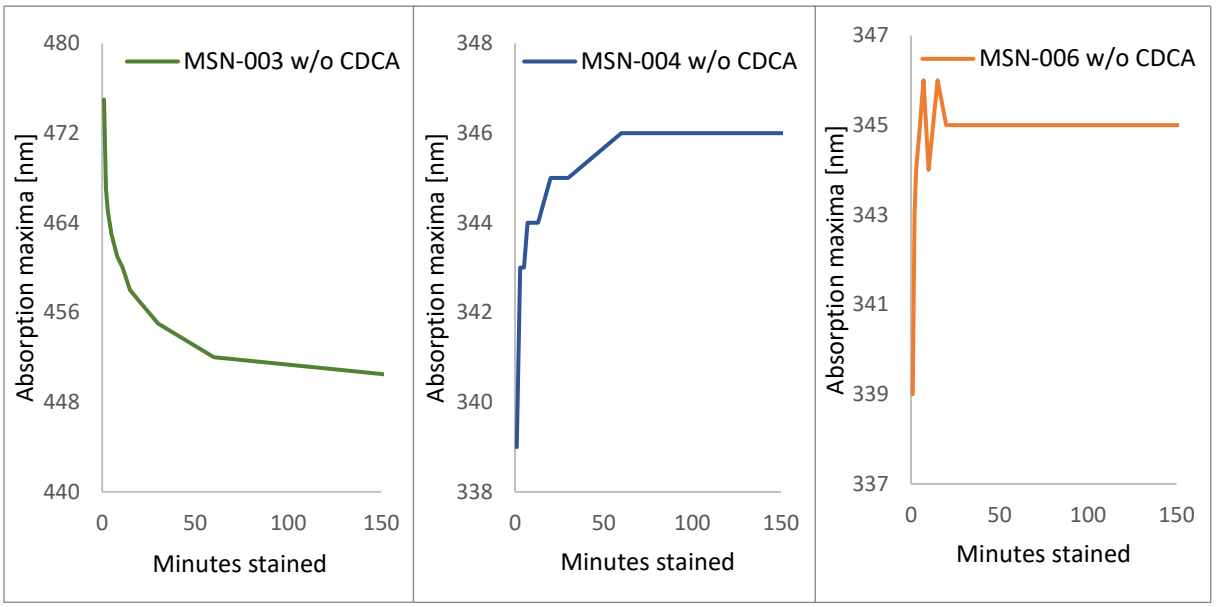

Figure 3.4.6: Excerpt of **Fig. 3.4.3** – **3.4.5** highlighting the initial absorption shift of the dyes **MSN-003**, **MSN-004** and **MSN-006** when adsorbed onto TiO_2 without CDCA.

The observed preferred formation of J-aggregates for **MSN-004** and **MSN-006** on TiO_2 is in accordance with the measured bathochromic shift of absorption maxima when comparing to the dye in solution (**Table 3.4.1**). The hypsochromic shift for **MSN-003** can also be explained by the preferred formation of H-aggregates shown in **Fig. 3.4.6**. This trend suggests that the formation of aggregates on the TiO_2 surface is a main contributor to absorption shift when CDCA is not used as co-adsorbent.

Interestingly, as seen in **Table 3.4.1** and **Fig. 3.4.3**, **MSN-003** exhibits a larger blue-shift when CDCA is added compared to without the addition of CDCA. This is surprising as **MSN-003** shows a preferential towards the formation of H-aggregates, and the expected result by inhibiting dye-dye aggregation with CDCA would be a decrease in the amount of hypsochromic shift. The same trend is observed for **MSN-004** and **MSN-006** as well, where an increasing blue-shift is measured when CDCA is used as co-adsorbent. No explanation for this observed phenomenon was found in the literature. There is however some uncertainty with the measurements in **Table 3.4.1** and **Fig. 3.4.3** – **Fig. 3.4.5** as they were only conducted in one parallel due to time constraints.

3.4.2 Photovoltaic Performance

The photovoltaic devices were manufactured and tested as described in Section 7.12-7.13. Six devices were manufactured for each dye, where three of them were tested with the addition of CDCA and the remaining three without CDCA. The results are reported in **Table 3.4.2** as the average

values of the measurements. The *J-V* curve of the best performing parallel of each dye is shown in **Fig. 3.4.7**.

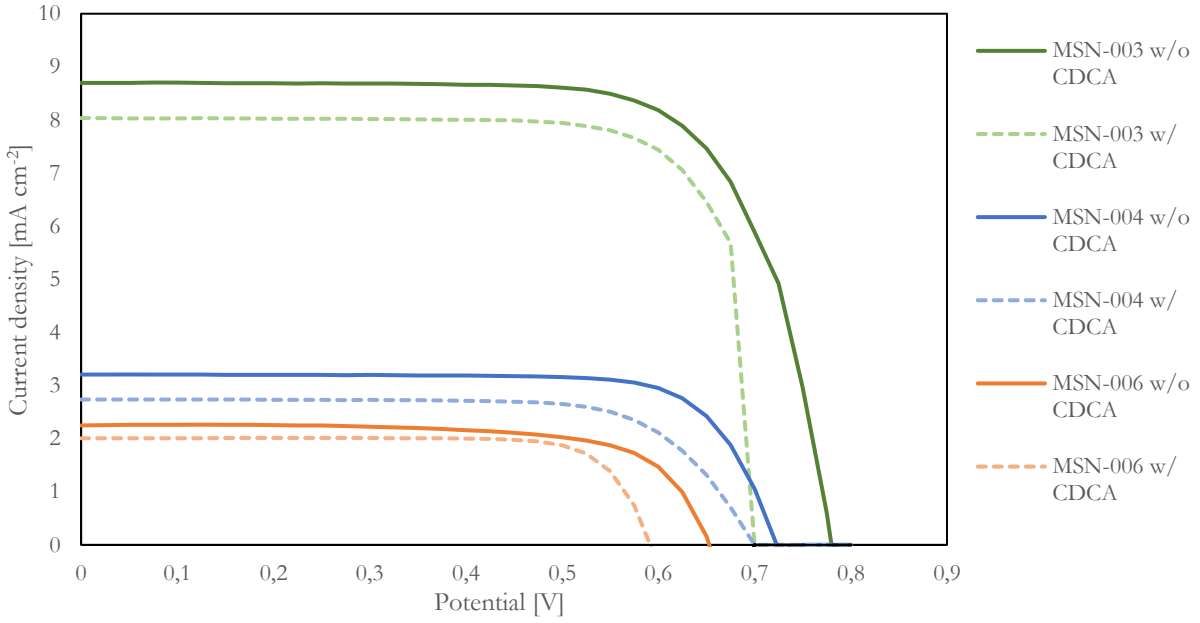

Figure 3.4.7: *J-V* curve of the best performing parallel from **MSN-003**, **MSN-004** and **MSN-006** with and without the addition of CDCA.

Table 3.4.2: Photovoltaic performance of **MSN-003**, **MSN-004** and **MSN-006** with (+) and without (-) the addition of CDCA. Values are given as an average of three parallels.

Dye	J_{SC} [mA cm^{-2}]	V_{OC} [V]	FF	PCE [%]
MSN-003 (+CDCA)	7.96	0.75	0.73	4.38
(-CDCA)	8.17	0.78	0.72	4.56
MSN-004 (+CDCA)	2.58	0.74	0.68	1.30
(-CDCA)	3.03	0.76	0.72	1.65
MSN-006 (+CDCA)	1.99	0.61	0.77	0.93
(-CDCA)	2.00	0.72	0.67	0.96

As seen in the results **MSN-003** clearly outperforms **MSN-004** and **MSN-006** with regards to short circuit current density (J_{SC}) and delivers an efficiency three times higher than the rest. This can be explained by the superior UV-Vis absorption properties of **MSN-003** (**Fig. 3.3.2.1**) allowing for absorption of more photons which ultimately leads to a higher amount of injected electrons and subsequent increased J_{SC}.

Due to **MSN-004** and **MSN-006** exhibiting almost identical UV-Vis absorption maxima the difference in J_{SC} must be explained by other factors. In **Fig. 3.4.2** there can be observed a higher absorption intensity for **MSN-004** compared to **MSN-006**. As the photon density of the absorbed light is ~identical for the dyes (due to similar absorption maxima) the increased performance of **MSN-004** must be due to increased dye loading and stronger dye-TiO_2 anchoring, accounting for the improved solar harvesting.

A decrease in open-circuit voltage (V_{OC}) is attributed to electron recombination from E_{CB} of the TiO_2 to either the electrolyte or oxidized dye molecules. The observed trend of decreasing V_{OC} in the order **MSN-003** > **MSN-004** > **MSN-006** can, again, be explained by **Fig. 3.4.2** which indicates a dye loading in the order of **MSN-003** > **MSN-004** > **MSN-006**. Increased dye loading leads to a more dense monolayer of dye-molecules on the TiO_2 surface which inhibits oxidized electrolyte from reaching the TiO_2 surface and, therefore, preventing the undesired recombination loss mechanism between electrolyte and TiO_2. As **MSN-006** exhibits the lowest dye loading on TiO_2 a higher degree of electrolyte-TiO_2 recombination is expected, leading to the low V_{OC} observed in the results.

A decrease in J_{SC}, V_{OC} and PCE is observed for all the dyes when CDCA is used as a co-adsorbent. A well-reported phenomenon accompanied with the addition of CDCA is the lowering of V_{OC}.[84] The decrease of V_{OC} is due to the carboxylic anchoring groups of CDCA increasing the protonation of the TiO_2 surface which shifts the E_{CB} of the TiO_2 towards a more positive potential, as described in Section 2.4. As expected, there is a balance between two competing processes. For CDCA to have a beneficial effect on the overall photovoltaic performance of the dyes the positive effects of inhibiting dye aggregation must outweigh the negative effects accompanied by the lowering of the V_{OC} and the reduced dye loading. The lower performance of the photovoltaic devices with CDCA as co-adsorbent indicates that the dyes are not especially prone to forming aggregates, and that the inherent reduction of V_{OC} and dye loading nullifies any potential positive effects.

The IPCE-measurements shown in **Fig. 3.4.3** depicts the best performing photovoltaic device out of three parallels for each of the dyes with the addition of CDCA. The measurements were performed as described in Section 7.12.

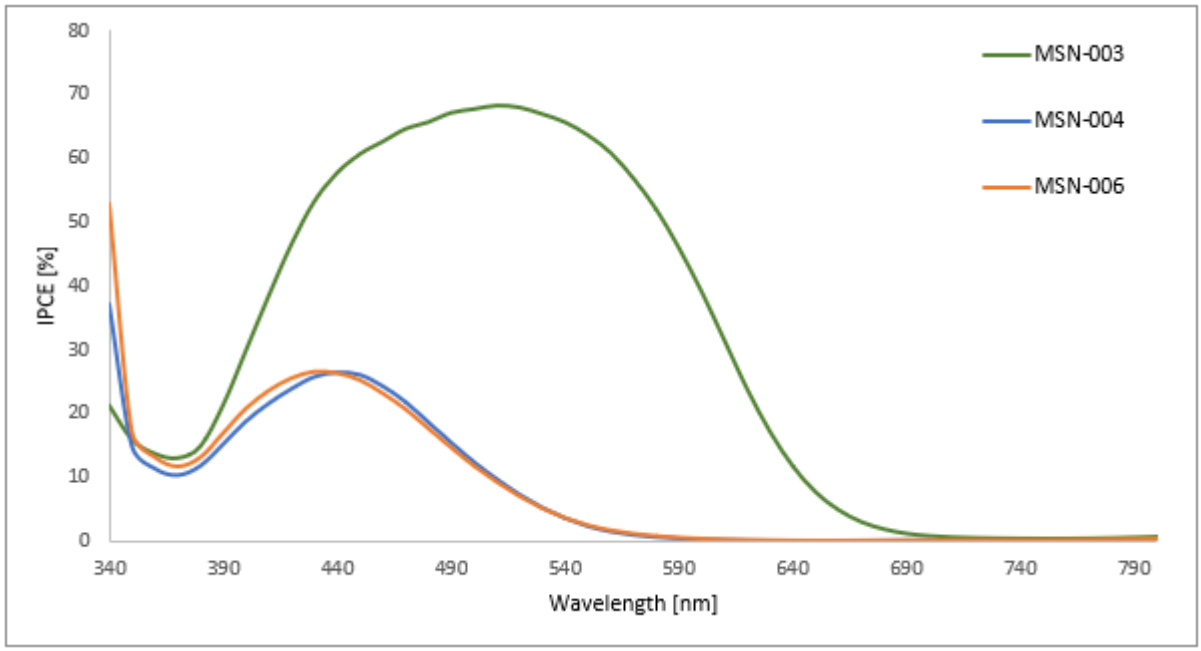

Figure 3.4.3: IPCE measurements of **MSN-003**, **MSN-004** and **MSN-006** with the addition of CDCA.

As seen in **Fig. 3.4.3**, **MSN-003** displays superior absorption properties compared to the rest of the dyes by being more red-shifted while at the same time showing a wider and more intense spectra, accounting for the enhanced photovoltaic performance. **MSN-004** and **MSN-006** display very similar IPCE values which is expected due to the similarities in the UV-Vis-spectra (**Fig. 3.3.2.1**).

6 Conclusion and Further Work

During this project three novel dyes for DSSCs, **MSN-004**, **MSN-005** and **MSN-006**, in addition to the reference dye **MSN-003**, bearing different anchoring groups has been synthesized and analysed in order to understand how the anchoring groups affect the optical properties of the chromophores when attached to the TiO_2 semiconductor.

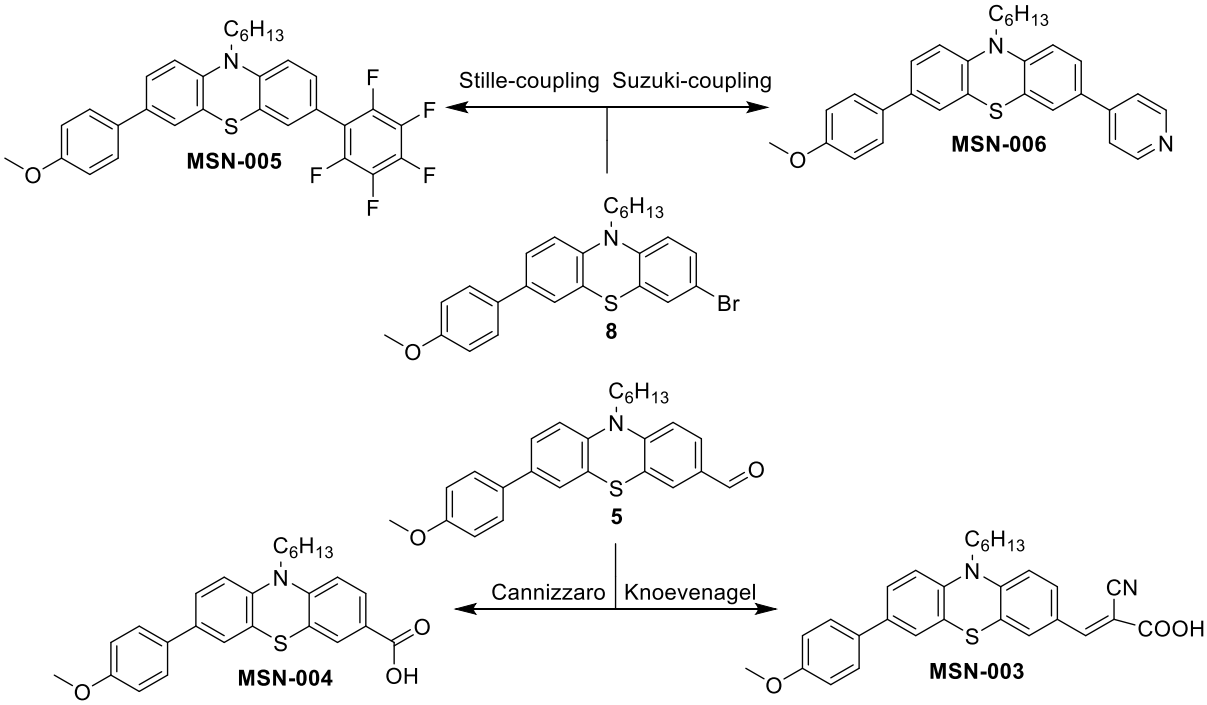

Scheme 6.1: The key intermediates **8** and **5** and the final reactions used to obtain the finished dyes.

The synthetic pathway for the dyes varied by utilizing different intermediates. **MSN-003** and **MSN-004** shared the common building block **8** and were obtained in a total yield of 15 and 3% respectively after a 5-step linear synthesis. **MSN-005** and **MSN-006** used the key intermediate **5** and were synthesized in a total yield of 1 and 10% respectively after a 3-step linear synthesis. The Stille-coupling to synthesize **MSN-005** proved to be especially challenging as three different procedures were attempted where the most successful gave a yield of 4%, leaving significant room for optimization.

UV-Vis analysis of the dyes in solution displayed very comparable absorption maxima for **MSN-004** – **MSN-006**, but a considerable bathochromic absorption shift was observed for **MSN-003**. The observed red-shift can only be attributed to the increased conjugation (extra double bond) of **MSN-003** enhancing the absorption properties of the chromophore.

When adsorbed onto TiO_2 without co-adsorbents the dyes **MSN-004** and **MSN-006** exhibited a bathochromic shift of absorption when compared to the dye in solution, while **MSN-003** revealed a hypsochromic shift of absorption. The results of **MSN-003** and **MSN-006** is in accordance with the predictions by Venkatraman *et al.*, whereas **MSN-004** contradicts the predictions.

It was found a preferential formation of J-aggregates on the TiO_2 surface for **MSN-004** and **MSN-006**, and a preference towards H-aggregates for **MSN-003**. The optical shifts expected with the formation of these aggregates is in accordance with the observed shift of absorption in the results, indicating

that the formation of aggregates is a considerable contributor to absorption shift when anchored onto TiO_2.

The photovoltaic performance of the dyes indicates a PCE in descending order **MSN-003** >> **MSN-004** > **MSN-006**. The superior performance of **MSN-003** is due to its red-shifted absorption spectra and strong dye-TiO_2 anchoring properties allowing for a high dye-loading. **MSN-004** performs slightly better than **MSN-006** which is attributed to higher dye-loading. A drop in PCE was measured for all the dyes when CDCA was used as co-adsorbent, indicating that the negative effects of reduced dye loading and V_{OC} accompanied with its inclusion outweigh any positive effects of inhibiting dye aggregation.

Further work includes the fabrication of devices with **MSN-005** and repeating the analyses conducted on the other dyes. There is also room for optimization for several of the reactions such as the Suzuki-coupling in the synthesis of **8** and **MSN-006**, as well as the Stille-coupling to yield **MSN-005**. For the synthesis of **MSN-004** a different synthetic pathway should be considered as the Cannizzaro reaction has an undesirable maximum yield of 50%.

For further optimization of the photovoltaic performance a screening of different concentrations of CDCA should also be conducted. A 10:1 ratio of CDCA/dye proved to give a drop in performance of the devices, but lower concentrations could give a positive effect. A more in-depth investigation of the observed hypsochromic shift for the dyes when adsorbed onto TiO_2 with CDCA as co-adsorbent should also be conducted.

7 Experimental

7.1 Instruments and Reagents

All solvents and reagents used were purchased from Sigma-Aldrich and were used without further purification. Anhydrous DMF, DCM and acetonitrile were collected from a MB-SPS-800 solvent purification system from MBRAUN. For reactions requiring water- and/or oxygen-free conditions the glassware was dried in an oven at 120 °C overnight and an N_2-atmosphere was established in the reaction environment prior to addition of reagents.

Purification by column chromatography was performed by manually packed columns of silica gel (40-63 μm diameter). Filtration through kieselgur was performed with Celite 545. Thin layer chromatography (TLC) was performed using "Merck Millipore TLC Silica gel 60 F_{254}", and the results were analysed with either UV-Vis or a solution of phosphomolybdic acid.

Melting points were measured using Gellenkemp Melting Point Apparatus.

IR spectra were recorded using a Bruker Alpha ECO-ATR FTIR-spectrometer and processed with OPUS software. The results are reported as wavenumber (cm^{-1}) of the absorption peak and the strength of the signal, w (weak), m (medium), s (strong) and br (broad).

UV-Vis was performed using a Hitachi U-1900 spectrometer with 10 mm light path. Results are reported as wavelength (nm) of absorption maxima (λ_{max}).

Accurate mass determination in positive and negative mode was performed on a "Synapt G2-S" Q-TOF instrument from Water TM. Samples were ionized by the use of ASAP probe (APCI) or ESI probe. No chromatographic separation was used prior to the mass analysis. Calculated exact mass and spectra processing was done by Waters TM Software Masslynx V4.1 SCN871.

NMR-analysis was conducted by either a Bruker Ascend 600 MHz equipped with a TCI CryoProbe (5 mm) or a Bruker Ascend 400 MHz equipped with a SmartProbe (5 mm), both utilizing Avance III HD Nanobay electronics. The samples were analysed in either deuterated chloroform ($CDCl_3$) or deuterated dimethyl sulfoxide (DMSO-d_6). The NMR data is reported as chemical shift in ppm (multiplicity, coupling constant(s), integral of protons, position in structure), ex. 7.2 (m, *J*=8.8 Hz, 3H, H-5). For compounds where full structural elucidation was not performed, position in structure is omitted in the NMR report.

7.2 Synthesis of 10-hexyl-10*H*-phenothiazine (**2**)

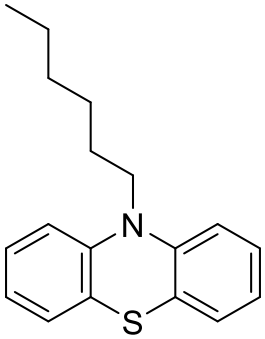

2

10*H*-Phenothiazine (**1**) (5.13 g, 25.7 mmol) and NaH (913 mg, 38.0 mmol) were mixed before dry THF (85 mL) were added under N_2-atmosphere. The mixture was left stirring at 22 °C for 20 minutes, before 1-bromohexane (5.29 mL, 37.7 mmol) was added dropwise over 30 minutes. The reaction was left stirring at room temperature for 20 minutes before heating to reflux. After 24 hours the reaction was cooled to room temperature and quenched with an aqueous NH_4Cl solution (50 mL, 5 wt%). The mixture was extracted with EtOAc (3 x 50 mL), and the combined organic phases were dried over anhydrous Na_2SO_4, filtered and solvents removed in vacuo. The crude product was purified by column chromatography (SiO_2, *n*-pentane, R_f: 0.2) giving the product (**2**) as a yellow oil (2.99 g, 10.55 mmol, 41%). ^{1}H NMR (400 MHz, DMSO-d_6) δ: 7.22-7.18 (m, 2H), 7.16-7.13 (m, 2H), 7.02-7.00 (m, 2H), 6.96-6.92 (m, 2H), 3.86 (t, *J*=6.9 Hz, 2H), 1.68 (quint, *J*=7.4 Hz, 2H), 1.42-1.34 (m, 2H), 1.26-1.22 (m, 4H), 0.82 (m, *J*=7.1 Hz, 3H). ^{1}H NMR recorded was in accordance with previously reported data,[27] and can be seen in Appendix A.1.

The experiment was performed in two parallels, as shown in **Table 7.1**.

Table 7.1: Two parallels for the synthesis of 10-hexyl-10*H*-phenothiazine (**2**).

Parallel	**1** [g, mmol]	NaH [mg, mmol]	1-Bromohexane [mL, mmol]	THF [mL]	Yield [%]
1	5.13, 25.7	913, 38.0	5.29, 37.7	85	41
2	6.97, 34.9	1147, 47.8	7.41, 52.78	120	40

The two parallels were performed identically with the exception of parallel 2 utilizing a solvent gradient (SiO_2, gradient: 0-0.5% EtOAc in *n*-pentane) when purifying with column chromatography.

7.3 Synthesis of 10-hexyl-10*H*-phenothiazine-3-carbaldehyde (**3**)

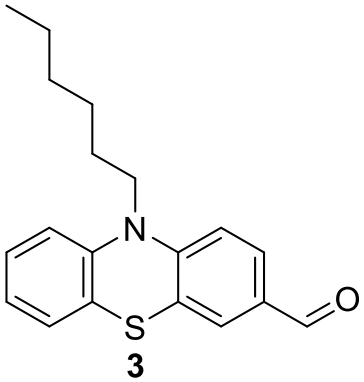

3

10-Hexyl-10*H*-phenothiazine (**2**) (3.93 g, 13.9 mmol) was dissolved in a mixture of dry 1,2-dichloroethane (110 mL) and DMF (5 mL) before cooling to 0 °C. $POCl_3$ (5.5 mL, 59 mmol) was added dropwise over 15 minutes, followed by heating to reflux. After 20 hours water (200 mL) was added, and an aqueous solution of sodium acetate until pH reached ~6. The aqueous phase was extracted with chloroform (4 x 200 mL), and the combined organic phases were dried over Na_2SO_4, filtered and solvents removed in vacuo. The crude product was purified by column chromatography in two parallels (SiO_2, 1:4 EtOAc: petroleum ether, R_f: 0.36) to obtain the product (**3**) as a cognac-coloured oil (3.01 g, 9.62 mmol, 69%). ^{1}H NMR (400 MHz, $CDCl_3$) δ: 9.82 (s, 1H), 7.67 (dd, *J*=8.4, 1.9 Hz, 1H), 7.61 (d, *J*=1.9 Hz, 1H), 7.21-7.17 (m, 1H), 7.14 (dd, *J*=7.6, 1.5 Hz, 1H), 6.99 (td, *J*=7.5, 1.1 Hz, 1H) 6.93-6.89 (m, 2H), 3.91 (t, *J*=7.3 Hz, 2H), 1.84 (quint, *J*=7.4 Hz, 2H), 1.50-1.42 (m, 2H), 1.35-1.31 (m, 4H), 0.90 (t, *J*=7.1 Hz, 3H). ^{1}H NMR recorded was in accordance with previously reported data,[85] and can be seen in Appendix B.1.

The experiment was performed in two parallels, as shown in **Table 7.2**.

Table 7.2: Two parallels for the synthesis of 10-hexyl-10*H*-phenothiazine-3-carbaldehyde (**3**).

Parallel	**2** [g, mmol]	DMF [mL]	Dichloroethane [mL]	$POCl_3$ [mL, mmol]	Yield [%]
1	1.02, 3.58	1.4	30	1.4, 15	17
2	3.92, 13.9	5	110	5.5, 59	69

7.4 Synthesis of 7-bromo-10-hexyl-10*H*-phenothiazine-3-carbaldehyde (**4**)

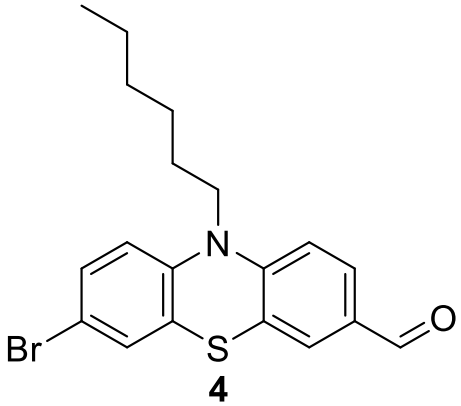

4

10-Hexyl-10*H*-phenothiazine-3-carbaldehyde (**3**) (0.21 g, 0.67 mmol) was dissolved in degassed THF (20 mL) and cooled to 0 °C. NBS (0.14 g, 0.78 mmol) was added followed by heating to 22 °C while stirring. After 20 hours water (20 mL) and an aqueous brine solution (20 mL) was added before extracting the combined aqueous phases with DCM (3 x 30 mL). The combined organic phases were dried over anhydrous Na_2SO_4, filtered, and the solvents removed in vacuo. The crude product was purified by column chromatography (SiO_2, DCM, R_f: 0.43) to obtain the product **4** as a viscous yellow oil (0.21 g, 0.55 mmol, 81%). ^{1}H NMR (400 MHz, $CDCl_3$) δ: 9.82 (s, 1H), 7.68 (dd, *J*=8.4, 1.9 Hz, 1H), 7.60 (d, *J*=1.9 Hz, 1H), 7.29-7.25 (m, 2H), 6.92 (d, *J*=8.5 Hz, 1H), 6.74 (d, *J*=8.6 Hz, 1H), 3.87 (t, *J*=7.3 Hz, 2H), 1.82 (quint, *j*=7.4 Hz, 2H), 1.48-1.41 (m, 2H), 1.34-1.30 (m, 4H), 0.88 (t, *J*=7.1 Hz, 3H). ^{1}H NMR spectra was in accordance with previously reported data,[85] and can be seen in Appendix C.1.

The experiment was performed in two parallels, as shown in **Table 7.3**.

Table 7.3: Two parallels for the synthesis of 7-bromo-10-hexyl-10*H*-phenothiazine-3-carbaldehyde (**4**).

Parallel	**3** [g, mmol]	THF [mL]	NBS [g, mmol]	Yield [%]
1	0.21, 0.67	20	0.14, 0.78	81
2	1.02, 3.26	32	0.67, 3.79	63

7.5 Synthesis of 10-hexyl-7-(4-methoxyphenyl)-10*H*-phenothiazine-3-carbaldehyde (**5**)

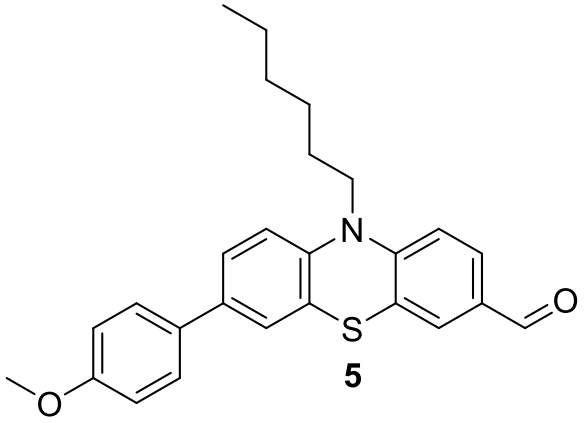

5

7-Bromo-10-hexyl-10*H*-phenothiazine-3-carbaldehyde (**4**) (0.81 g, 2.06 mmol), K_2CO_3 (1.17 g, 8.44 mmol), $Pd(PPh_3)_4$ (30.1 mg, 0.026 mmol) and 4-methoxyphenylboronic acid (0.35 g, 2.27 mmol) were combined before degassed 1,4-dioxane (23 mL) and water (23 mL) was added under N_2-atmosphere. The mixture was heated to 80 °C and left stirring for 3 hours before cooling to room temperature. Water (45 mL) was added, and the aqueous phase was extracted with DCM (3 x 30 mL). The combined organic phases were dried over anhydrous Na_2SO_4, filtered and the solvents removed in vacuo. The crude product was purified by column chromatography (SiO_2, 1:9 EtOAc:*n*-pentane, R_f: 0.46) to obtain the product **5** as an orange oil (0.72 g, 1.72 mmol, 84%). ^{1}H NMR (400 MHz, $CDCl_3$) δ: 9.82 (s, 1H), 7.67 (dd, *J*=8.4, 1.9 Hz, 1H), 7.62 (d, *J*=1.9 Hz, 1H), 7.49-7.47 (m, 2H), 7.36 (dd, *J*=8.4, 2.2 Hz, 1H), 7.32 (d, *J*=2.2 Hz, 1H), 6.99-6.97 (m, 2H), 6.93 (dd, *J*=8.5, 2.4 Hz, 2H), 3.93 (t, *J*=7.3 Hz, 2H), 3.87 (s, 3H), 1.87 (quint, *J*=7.4 Hz, 2H), 1.52-1.45 (m, 2H), 1.37-1.34 (m, 4H), 0.91 (t, *J*=7.1 Hz, 3H). ^{1}H NMR recorded was in accordance with previously reported data,[85] and can be seen in Appendix D.1.

The experiment was performed in two parallels, as shown in **Table 7.4**.

Table 7.4: Two parallels for the synthesis of 10-hexyl-7-(4-methoxyphenyl)-10*H*-phenothiazine-3-carbaldehyde (**5**).

Parallel	**4** [g, mmol]	Boric acid [g, mmol]	K_2CO_3 [g, mmol]	$Pd(PPh_3)_4$ [mg, mmol]	Dioxane [mL]	Water [mL]	Yield [%]
1	0.21, 0.55	0.09, 0.61	0.31, 2.21	6.8, 0.006	6	6	33
2	0.81, 2.06	0.35, 2.27	1.17, 8.44	30.1, 0.026	23	23	84

7.6 Synthesis of 3,7-dibromo-10-hexyl-10*H*-phenothiazine (**7**)

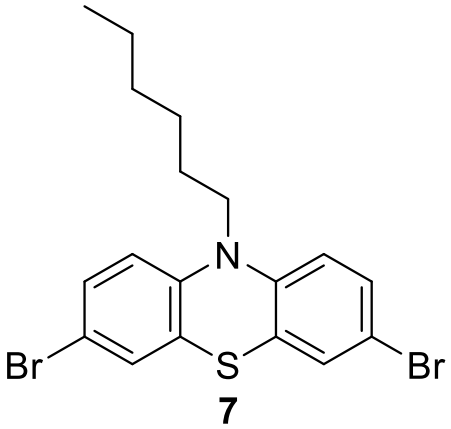

7

3,7-Dibromo-10*H*-phenothiazine (**6**) (10.33 g, 28.92 mmol) and NaH (1.03 g, 43.00 mmol) were mixed before dry THF (115 mL) was added under N_2-atmosphere. The reaction was left stirring at 22 °C for 15 minutes before 1-bromohexane (6.05 mL, 43.00 mmol) was added dropwise over 40 minutes. The reaction was heated to reflux for 22 hours, before cooling to room temperature and quenching with an aqueous NH_4Cl solution (5% wt, 50 mL). The aqueous phase was extracted with EtOAc (4 x 50 mL), and the combined organic phases were dried over anhydrous $MgSO_4$, filtered and the solvents were removed in vacuo. No further purification of the product was deemed necessary. Compound **7** was obtained as a brown solid (12.20 g, 27.64 mmol, 96%). ^{1}H NMR (400 MHz, DMSO-d_6) δ: 7.36-7.34(m, 4H), 6.95-6.93 (m, 2H), 1.61 (quint, *J*=7.2 Hz, 2H), 1.40-1.29 (m, 2H), 1.29-1.16 (m, 4H), 0.83-0.79 (m, 3H). ^{1}H NMR was in accordance with reported data,[27] and can be seen in Appendix E.1.

The experiment was performed in two parallels, as shown in **Table 7.5**.

Table 7.5: Two parallels for the synthesis of 3,7-dibromo-10-hexyl-10*H*-phenothiazine (**7**).

Parallel	**6** [g, mmol]	NaH [g, mmol]	1-Bromohexane [mL, mmol]	THF [mL]	Yield [%]
1	9.68, 27.10	0.93, 38.76	5.33, 37.94	110	56
2	10.33, 28.92	1.03, 43.00	6.05, 43.00	115	96

7.7 Synthesis of 3-bromo-10-hexyl-7-(4-methoxyphenyl)-10*H*-phenothiazine (**8**)

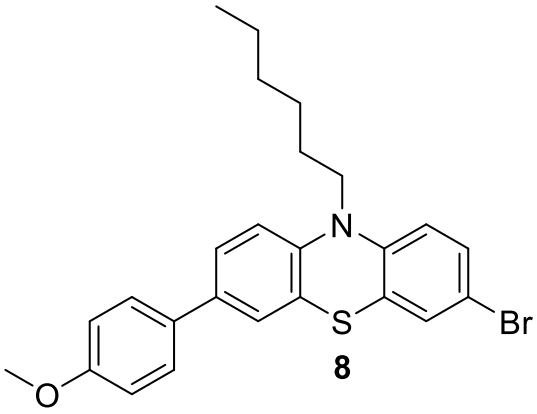

8

3,7-Dibromo-10-hexyl-10*H*-phenothiazine (**7**) (3.96 g, 8.98 mmol), 4-methoxyphenylboronic acid (1.50 g, 9.86 mmol), $Pd(PPh_3)_4$ (104 mg, 0.09 mmol) and K_2CO_3 (4.99 g, 36.09 mmol) were mixed before degassed 1,4-dioxane (30 mL) and water (30 mL) was added under N_2-atmosphere. The mixture was heated to 80 °C and left stirring for 19 hours before cooling to room temperature. Water (50 mL) was added, followed by an extraction with EtOAc (3 x 50 mL). The combined organic phases were dried over anhydrous Na_2SO_4, filtered, and the solvents were removed in vacuo. The crude product was purified by column chromatography (SiO_2, 1:9 EtOAc:*n*-pentane, R_f: 0.56) to obtain the product **8** as a yellow oil (1.00 g, 2.14 mmol, 24%). ^{1}H NMR (400 MHz, $CDCl_3$) δ: 7.48-7.46 (m, 2H), 7.36-7.34 (m, 1H), 7.32 (m, 1H), 7.28-7.24 (m, 2H), 6.98-6.96 (m, 2H), 6.90 (d, *J*=3.4 Hz, 1H), 6.72 (d, *J*=8.4 Hz, 1H), 3.86-3.82 (m, 5H), 1.85-1.78 (quint, *J*=7.4 Hz, 2H), 1.49-1.42 (m, 2H), 1.34-1.31 (m, 4H), 0.90 (t, *J*=7.1 Hz, 3H). ^{1}H NMR was in accordance with reported data,[27] and can be seen in Appendix F.1.

7.8 Synthesis of (*E*)-2-cyano-3-(10-hexyl-7-(4-methoxyphenyl)-10*H*-phenothiazin-3-yl)acrylic acid (MSN-003)

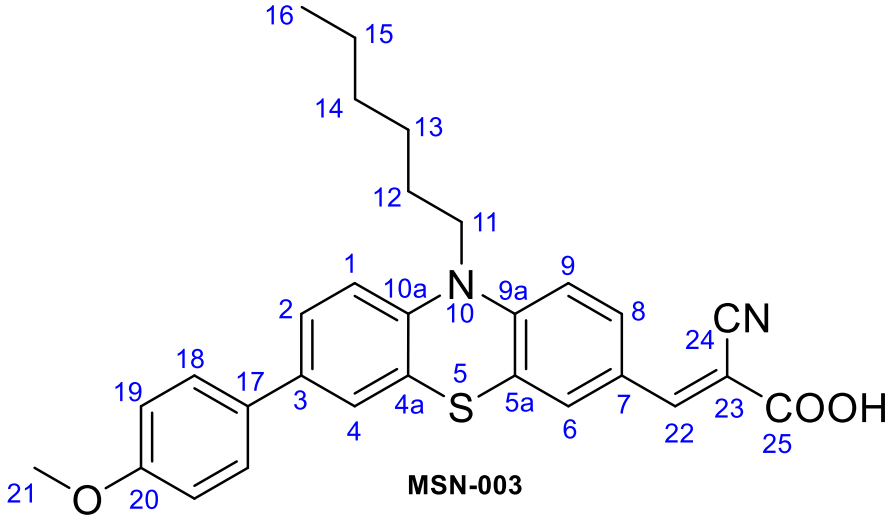

MSN-003

10-Hexyl-7-(4-methoxyphenyl)-10*H*-phenothiazine-3-carbaldehyde (**5**) (0.21 g, 0.50 mmol) and cyanoacetic acid (0.86 g, 10.14 mmol) were dissolved in degassed acetonitrile (55 mL) under N_2-atmosphere. Piperidine (0.6 mL, 6.06 mmol) was added and the reaction mixture was heated to 80 °C for 45 minutes. The mixture was then cooled to room temperature, and subsequently quenched with aqueous HCl (2M, 150 mL). EtOAc (60 mL) was added and the organic phase was washed with water (8 x 100 mL) and saturated brine solution (1 x 50 mL), before drying over anhydrous Na_2SO_4, filtered and the solvents were removed in vacuo. No further purification of the product was deemed necessary. **MSN-003** was obtained as a dark solid (0.19 g, 0.39 mmol, 78%), mp. 205-208 °C (lit. 204-208).[27] ^{1}H NMR (600 MHz, DMSO-d_6) δ: 13.78 (s, 1H, H-25), 8.21 (s, 1H, H-22), 7.97 (dd, *J*=8.7, 2.1 Hz, 1H, H-8), 7.88 (d, *J*=2.1 Hz, 1H, H-6), 7.63 (d, *J*=8.8 Hz, 2H, H-18), 7.51 (dd, *J*=8.5, 2.2 Hz, 1H, H-2), 7.46 (d, *J*=2.2 Hz, 1H, H-4), 7.21 (d, *J*=8.7 Hz, 1H, H-9), 7.16 (d, *J*=8.5 Hz, 1H, H-1), 7.04 (d, *J*=8.8 Hz, 2H, H-19), 4.01 (t, *J*=7.1 Hz, 2H, H-11), 3.84 (s, 3H, H-21), 1.76 (quint., *J*=7.7 Hz, 2H, H-12), 1.49-1.43 (m, 2H, H-13), 1.36-1.28 (m, 4H, H-14, H-15), 0.89 (t, *J*=6.9 Hz, 3H, H-16). ^{13}C NMR (150 MHz, DMSO-d_6) δ: 163.12 (C-25), 158.16 (C-20), 151.80 (C-22), 147.97 (C-9a), 140.52 (C-10a), 134.63 (C-3), 130.99 (C-8), 130.26 (C-17), 128.41 (C-6), 126.56 (C-18), 124.88 (C-2), 124.81 (C-7), 123.91 (C-4), 122.08 (C-5a), 121.90 (C-4a), 116.17 (C-24), 116.02 (C-1), 114.85 (C-9), 113.68 (C-19), 98.95 (C-23), 54.50 (C-21), 46.29 (C-11), 30.13 (C-14), 25.39 (C-12), 25.03 (C-13), 21.41 (C-15), 13.16 (C-16). IR (neat) (cm^{-1}): 2954 (m), 2930 (m), ~2200 (w), 1689 (m), 1570 (s), 1497 (s), 1209 (s), 1177 (s), 808 (m). HRMS (ASAP-TOF+): *m/z*: $[M+H]^+$ calculated for $C_{29}H_{29}N_2O_3S$: 485.1899, found 485.1898. UV-Vis (DCM, 22 °C) λ_{max} (nm): 447.

The spectroscopic data for **MSN-003** are shown in Appendix G.1-G.5. See Section 3.3.1.2 for structure elucidation and assigning of shifts.

7.9 Synthesis of 10-hexyl-7-(4-methoxyphenyl)-10H-phenothiazine-3-carboxylic acid (MSN-004)

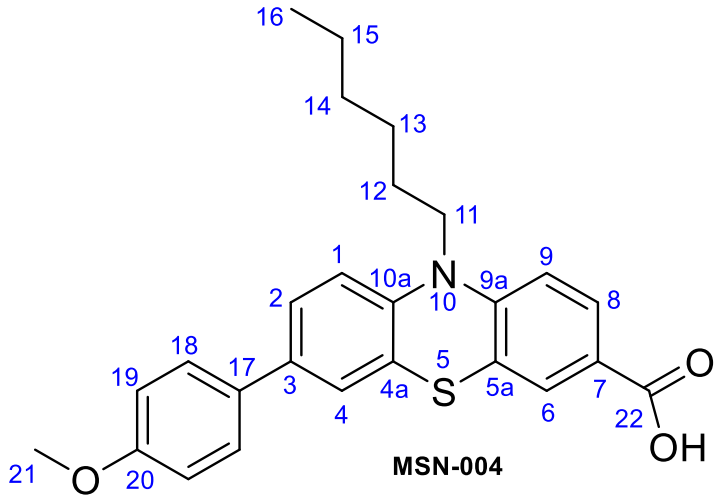

MSN-004

10-Hexyl-7-(4-methoxyphenyl)-10*H*-phenothiazine-3-carbaldehyde (**5**) (0.12 g, 0.29 mmol) and *t*-BuOK (0.13 g, 1.19 mmol) were mixed before THF (6 mL, 0 °C) was added, and the reaction mixture was left stirring at room temperature. After 43 hours additional *t*-BuOK (0.05 g, 0.44 mmol) was added, and the reaction was heated to 60 °C and let stir for an additional 23 hours before cooling to room temperature. Water (20 mL) was added followed by acetic acid (glacial) until neutral pH was reached. The mixture was extracted with EtOAc (4 x 15 mL), the combined organic phases were dried over anhydrous Na_2SO_4, filtered, and the solvents were removed in vacuo. The crude product was purified by column chromatography (SiO_2, gradient: 0-15% MeOH in DCM) to obtain the product **MSN-004** as a dark solid (0.02 g, 0.05 mmol, 17%), mp. 137-139 °C. ^{1}H NMR (400 MHz, $CDCl_3$) δ: 7.88 (dd, *J*=8.6, 2.0 Hz, 1H, H-8), 7.82 (d, *J*=2.0 Hz, 1H, H-6), 7.45 (d, *J*=8.8 Hz, 2H, H-18), 7.32 (dd, *J*=8.4, 2.1 Hz, 1H, H-2), 7.29 (d, *J*=2.1 Hz, 1H, H-4), 6.95 (d, *J*=8.8 Hz, 2H, H-19), 6.89 (d, *J*=8.4 Hz, 2H, H-1), 6.84 (d, *J*=8.6 Hz, 1H, H-9), 3.88 (t, *J*=7.3 Hz, 2H, H-11), 3.84 (s, 3H, H-21), 1.83 (quint., *J*=7.4 Hz, 2H, H-12), 1.50-1.40 (m, 2H, H-13), 1.36-1.28 (m, 4H, H-14, H-15), 0.89 (t, *J*=7.1 Hz, 3H, H-16). ^{13}C NMR (100 MHz, $CDCl_3$) δ: 171.15 (C-22), 159.09 (C-20), 149.96 (C-9a), 142.36 (C-10a), 136.14 (C-3), 132.29 (C-17), 130.13 (C-8), 129.25 (C-6), 127.56 (C-18), 125.62 (C-2/C-4), 125.48 (C-2/C-4), 124.30 (C-4a), 123.88 (C-5a), 122.83 (C-7), 115.91 (C-1), 114.35 (C-9), 114.27 (C-19), 55.37 (C-21), 47.93 (C-11), 31.43 (C-14), 26.72 (C-12), 26.58 (C-13), 22.60 (C-15), 14.00 (C-16). IR (neat) (cm^{-1}): 2916 (s), 2849 (m), 1683 (s), 1582 (m), 1466 (s), 1240 (s), 1024 (s), 801 (s). HRMS (ASAP-TOF+): *m/z*: $[M+H]^+$ calculated for $C_{26}H_{28}NO_3S$: 434.1790, found 434.1782. UV-Vis (DCM, 22 °C) λ_{max} (nm): 333.

The spectroscopic data for **MSN-004** are shown in Appendix H.1-H.5 and have not been published previously. See Section 3.3.1.1 for structure elucidation and assigning of shifts.

7.10 Synthesis of 10-hexyl-3-(4-methoxyphenyl)-7-(perfluorophenyl)-10H-phenothiazine (MSN-005)

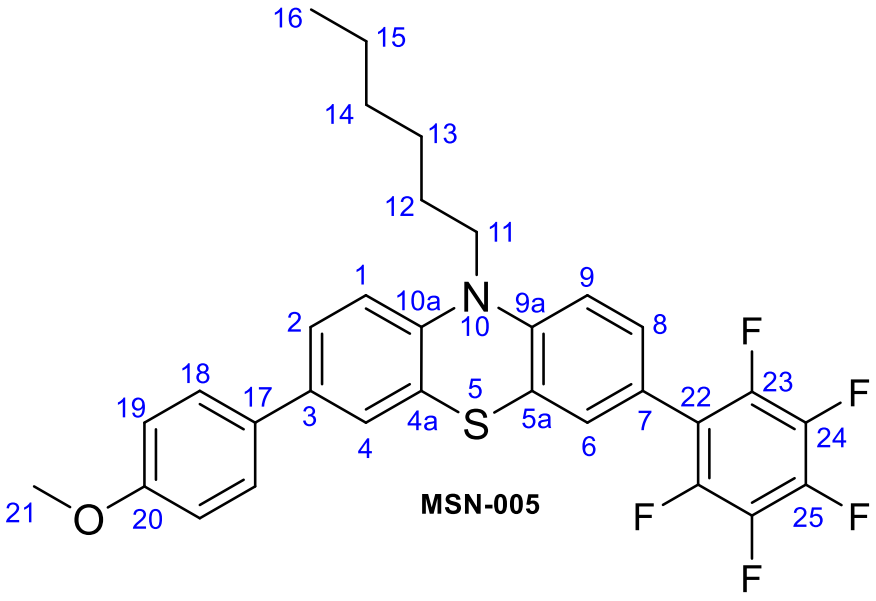

10-Hexyl-3-(4-methoxyphenyl)-7-(perfluorophenyl)-10H-phenothiazine (**MSN-005**) was attempted synthesized following three different procedures.

Procedure 1

This procedure was described by Gao *et al.*[74] $Pd_2(dba)_3$ (12.3 mg, 0.013 mmol) and $P(o\text{-}tol)_3$ (22.0 mg, 0.072 mmol) were mixed before tributyl(pentafluorophenyl)stannane (**9**) (0.14 mL, 0.398 mmol) and 3-bromo-10-hexyl-7-(4-methoxyphenyl)-10*H*-phenothiazine (**8**) (0.1206 g, 0.257 mmol) dissolved in degassed 1,2-dichlorobenzene (2.8 mL) was added under N_2-atmosphere. The reaction mixture was heated to 80 °C under stirring. The reaction was stopped after 72 hours, EtOAc (20 mL) and water (20 mL) was added and the organic phase was separated. The organic phase was washed with an aqueous KF solution (1M, 5 x 15 mL) and finally with a saturated brine solution (2 x 20 mL). The organic phase was dried over anhydrous $MgSO_4$ and the solvents were removed in vacuo. The crude product was attempted purified by column chromatography (SiO_2, 1:6 EtOAc:n-pentane), but no formation of **MSN-005** was identified.

Procedure 2

For the second attempt the procedure of Mee *et al.*[58] was followed with the exception of 1,2-dichlorobenzene being used as solvent instead of DMF. $Pd(PPh_3)_4$ (22.7 mg, 0.0197 mmol), CuI (8 mg, 0.042 mmol) and CsF (70 mg, 0.46 mmol) were mixed before **9** (0.13 mL, 0.369 mmol) and **8** (0.0823 g, 0.176 mmol) dissolved in degassed 1,2-dichlorobenzene (3.5 mL) was added under N_2-atmosphere. The reaction mixture was heated to 80 °C under stirring. After 27 hours additional $Pd(PPh_3)_4$ (10.0 mg, 0.0868 mmol), **9** (0.05 mL, 0.149 mmol) and 1,2-dichlorobenzene (1 mL) was added. The mixture was stopped after a total reaction time of 100 hours. EtOAc (20 mL) and water (20 mL) was added and the organic phase was separated. The organic phase was washed with an aqueous KF solution (1M, 7 x 15 mL) and finally with a saturated brine solution (1 x 15 mL). The organic phase was dried

over anhydrous $MgSO_4$ and the solvents were removed in vacuo. The crude product was attempted purified by column chromatography (SiO_2, 1:10 EtOAc:n-pentane), but no formation of **MSN-005** was identified.

Procedure 3

For the third attempt the procedure of Littke *et al.*[75] was followed, except for 1,4-dioxane being used as solvent instead of NMP. $Pd_2(dba)_3$ (9.0 mg, 0.0098 mmol), $P(t\text{-}Bu)_3$ (7.3 mg, 0.014 mmol), CsF (0.027 mL, 0.724 mmol) and **8** (0.1706 g, 0.364 mmol) were mixed and dissolved in degassed 1,4-dioxane (10 mL) before **9** (0.15 mL, 0.426 mmol) was added under N_2-atmosphere. The reaction was heated to 80 °C and let stir for 44 hours. EtOAc (20 mL) and water (20 mL) was added and the organic phase was separated. The organic phase was washed with an aqueous KF solution (1M, 4 x 15 mL) and finally with a saturated brine solution (1 x 15 mL). The organic phase was dried over anhydrous Na_2SO_4 and the solvents were removed in vacuo. The crude product was purified by column chromatography (SiO_2, 1:30 EtOAc:n-pentane, R_f:0.16) to obtain the product **MSN-005** as a brown solid (8.4 mg, 0.015 mmol, 4%). Melting point analysis could not be conducted due to insufficient amounts of product. ^{1}H NMR (600 MHz, $CDCl_3$) δ: 7.45 (d, *J*=8.8 Hz, 2H, H-18), 7.33 (dd, *J*=8.4, 2.2 Hz, 1H, H-2), 7.32 (d, *J*=2.0 Hz, 1H, H-4), 7.22-7.18 (m, 2H, H-6, H-8), 6.95 (d, *J*=8.6, 2H, H-19), 6.93 (d, 1H, H-9), 6.91 (d, *J*=8.4 Hz, 1H, H-1), 3.89 (t, *J*=7.2 Hz, 2H, H-11), 3.84 (s, 3H, H-21), 1.86 (quint., *J*=7.5 Hz, 2H, H-12), 1.50-1.44 (m, 2H, H-13), 1.36-1.31 (m, 4H, H-14, H-15), 0.89 (t, *J*=7.0 Hz, 3H, H-16). ^{13}C NMR (150 MHz, $CDCl_3$) δ: 159.03 (C-20), 146.12 (C-9a), 143.18 (C-10a), 135.73 (C-3), 132.47 (C-17), 129.19 (C-6/C-8), 128.76 (C-6/C-8), 127.75 (C-22), 127.56 (C-18), 125.66 (C-2/C-4), 125.66 (C-2/C-4), 124.85 (C-5a), 124.46 (C-4a), 119.98 (C-7), 115.69 (C-1), 115.07 (C-9), 114.25 (C-19), 55.36 (C-21), 47.66 (C-11), 31.48 (C-14), 26.84 (C-12), 26.69 (C-13), 26.62 (C-15), 13.99 (C-16). ^{19}F NMR (400 MHz, $CDCl_3$) δ: -143.21 (1F), -156.11 (2F), -162.32 (2F). IR (neat) (cm^{-1}): 2954 (s), 2920 (s), 2852 (m), 1605 (m), 1520 (s), 1241 (s), 1111 (s), 983 (s), 811 (s). HRMS (ASAP-TOF+): *m/z*: $[M+H]^+$ calculated for $C_{31}H_{27}NOF_5S$: 556.1734, found 556.1724. UV-Vis (DCM, 22 °C) λ_{max} (nm): 331.

The spectroscopic data for **MSN-005** are shown in Appendix I.1-I.6 and have not been published previously. See Section 3.3.1.4 for structure elucidation and assigning of shifts.

7.11 Synthesis of 10-hexyl-3-(4-methoxyphenyl)-7-(pyridine-4-yl)-10*H*-phenothiazine (MSN-006)

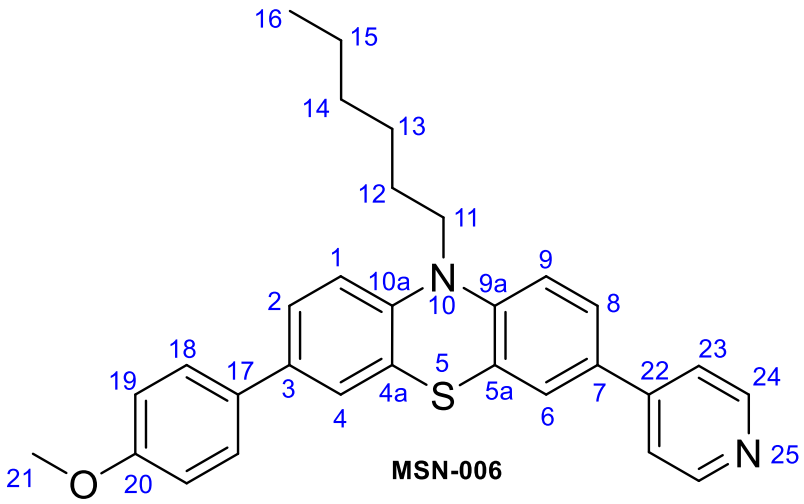

$Pd(PPh_3)_4$ (9.6 mg, 0.008 mmol), K_2CO_3 (0.07 g, 0.51 mmol) and pyridin-4-ylboronic acid (**10**) (0.03 g, 0.25 mmol) were mixed together before 3-bromo-10-hexyl-7-(4-methoxyphenyl)-10*H*-phenothiazine (**8**) (0.08 g, 0.17 mmol) dissolved in a solution of degassed water (2 mL) and 1,4-dioxane (4 mL) was added. The reaction mixture was heated to 80 °C and left stirring for 19 hours under N_2-atmosphere. After cooling to room temperature water (10 mL) was added, followed by an extraction with EtOAc (4 x 15 mL). The combined organic phases were dried over anhydrous $MgSO_4$, filtered, and the solvents were removed in vacuo. The crude product was purified by column chromatography (SiO_2, 1:29 MeOH:DCM, R_f: 0.23) to obtain the product **MSN-006** as a dark-orange semi-solid (0.036 g, 0.077 mmol, 45%). ^{1}H NMR (600 MHz, $CDCl_3$) δ: 8.60 (d, *J*=6.0 Hz, 2H, H-24), 7.45 (d, *J*=8.7 Hz, 2H, H-18), 7.44-7.39 (m, 4H, H-6, H-8, H-23), 7.34-7.31 (m, 2H, H-2, H-4), 6.94 (d, *J*=8.7 Hz, 2H, H-19), 6.90 (d, *J*=8.4 Hz, 1H, H-9) 6.88 (d, *J*=8.3 Hz, 1H, H-1), 3.87 (t, *J*=7.2 Hz, 2H, H-11), 3.83 (s, 3H, H-21), 1.83 (quint., *J*=7.4 Hz, 2H, H-12), 1.49-1.42 (m, 2H, H-13), 1.36-1.28 (m, 4H, H-14, H-15), 0.88 (t, *J*=6.9 Hz, 3H, H16). ^{13}C NMR (150 MHz, $CDCl_3$) δ: 159.00 (C-20), 150.24 (C-24), 146.94 (C-22), 146.01 (C-9a), 143.14 (C-10a), 135.58 (C-3), 132.42 (C-17), 131.82 (C-7), 127.51 (C-18), 125.88, 125.61, 125.57, 125.44, 125.19 (C-5a), 124.32 (C-4a), 120.70 (C-23), 115.62 (C-1/C-9), 115.46 (C-1/C-9), 114.23 (C-19), 55.32 (C-21), 47.65 (C-11), 31.45 (C-14), 26.79 (C-12), 26.63 (C-13), 22.60 (C-15), 13.99 (C-16). IR (neat) (cm^{-1}): 2922 (m), 2850 (m), 1593 (s), 1462 (s), 1240 (s) 1178 (s), 803 (s). HRMS (ASAP-TOF+): *m/z*: $[M+H]^+$ calculated for $C_{30}H_{31}N_2OS$: 467.2157, found 467.2161. UV-Vis (DCM, 22 °C) λ_{max} (nm): 340.

The spectroscopic data for **MSN-006** are shown in Appendix J.1-J.5 and have not been published previously. See Section 3.3.1.3 for structure elucidation and assigning of shifts.

The experiment was performed in two parallels, as shown in **Table 7.6**.

Table 7.6: Two parallels for the synthesis of 10-hexyl-3-(4-methoxyphenyl)-7-(pyridine-4-yl)-10*H*-phenothiazine (**MSN-006**).

Parallel	**8** [g, mmol]	**10** [g, mmol]	K_2CO_3 [g, mmol]	$Pd(PPh_3)_4$ [mg, mmol]	Dioxane [mL]	Water [mL]	Yield [%]
1	0.08, 0.17	0.03, 0.25	0.07, 0.51	9.6, 0.008	4	2	45
2	0.28, 0.59	0.12, 0.94	0.22, 1.58	31.9, 0.028	14	6	14

7.12 Fabrication of Photovoltaic Devices

The fabrication procedure is based on the previously reported procedures by Buene *et al*.[27] and Hora *et al*.[86]

The anodes were manufactured from FTO glass (TEC10, Sigma-Aldrich) which was cleaned by a solution of KOH (150 g/L) in 70 wt.% ethanol under sonication for 45 minutes. A blocking layer was deposited onto the FTO by immersion of the glass in an aqueous $TiCl_4$-solution (40 mM) at 70 °C for 2 × 45 minutes, followed by rinsing with water (deionized) and ethanol. The TiO_2-layer formed was sintered at 500 °C for an hour.

A total of three layers of TiO_2 were screen printed onto the FTO (54 mesh count, 64 mm thread diameter, 0.2826 cm^2 area). The first two layers (18NR-T, Dyesol) were printed with 10 minutes heating on a hotplate at 120 °C after each layer. Finally, a scattering layer (WER2-O, Dyesol) was printed, and the TiO_2 electrode was sintered in a programmable furnace (Nabertherm LT 9/12) at set temperatures of 125, 250, 325, 450, and 500 °C for 5, 5, 5, 15, and 15 minutes with a ramping time of 10 minutes. The electrodes were annealed at 500 °C for 30 minutes using a hot air gun before staining.

The counter electrodes were manufactured from TEC10 FTO glass supplied by Sigma-Aldrich. Immersing the electrodes in water and using a diamond drill bit, holes were drilled into the electrodes from the FTO-side. The counter electrodes were subsequently cleaned using an aqueous solution of Deconex 21 (2 g/L), water (deionized), ethanol, and acetone in an ultrasonic bath for 15 minutes each. A solution of H_2PtCl_6 (10 mM in 2-propanol) was dropcast (5 µL/cm^2) on the FTO-side of the counter electrode before heating at 400 °C for 15 minutes with a hot air gun, forming the catalytic layer of Pt.

The photoanodes were immersed in the dye staining solution while still hot (~80 °C) from the annealing-procedure, and stored overnight in an oven holding 30 °C. The dye staining solutions were prepared using a mixture of acetonitrile and THF (43/57, v/v) to make a solution of dye and co-adsorbent CDCA, at concentrations of 0.5 mM and 5 mM respectively. After 15 hours of staining the electrodes were rinsed in acetonitrile for 2 minutes before being sealed to the counter electrode using Surlyn (25 µm, Solaronix). The cells were sufficiently sealed by using a 50 W PTC heat element (4 x 20 seconds treatment). The electrolyte was vacuum backfilled into the device followed by sealing the filling-hole with Surlyn and a glass cover disk. Finally, the electrodes were painted with silver paint (Electrolube, SCP) for increased conductivity. The electrolyte employed was the A6141 electrolyte, consisting of butylmethylimidazolium iodide (0.60 M), I_2 (0.03 M), guanidinium thiocyanate (0.1 M), and t-butylpyridine (0.50 M) dissolved in acetonitrile/valeronitrile (85/15, v/v).[17]

7.13 Characterization of Photovoltaic Devices

The DSSCs *J-V* characteristics were measured with a Keithley 2450 under a Sciencetech SP300B solar simulator with an AM 1.5 G filter, calibrated to 100 mW/cm^2 with a Newport Reference Solar Cell and Meter (91150V). All cells were masked with a 0.159 cm^2 black mask before characterization. IPCE measurements were obtained from a device fabricated with a halogen lamp (Ocean Optics HL-2000), a monochromator (Spectral Products CM110), connected to the Keithley 2450. The light intensity was determined using a NIST traceable calibrated photodiode (Thorlabs, FDS100-CAL).

7.14 Optical Measurements of TiO_2 Electrodes

The transparent electrodes were manufactured in the same manner as the photoanodes described in Section 7.12, with the exception of only one layer of TiO_2 (18NR-T, Dyesol) being screen printed and the exclusion of the scattering layer. The electrodes were not annealed before staining.

The dye staining solutions were prepared using a mixture of acetonitrile and THF (43/57, v/v) to make a solution of dye at 0.5 mM concentration. CDCA was added at 5 mM concentration when applicable. The electrodes were immersed in the dye staining solutions for fixed amounts of time before being washed in acetonitrile for 1 minute and air-dried. The electrodes were then analysed with UV-Vis before being immersed in the dye staining solution for another set amount of time.

7.15 Cyclic Voltammetry

Electrochemistry studies were performed using a standard three-electrode cell under argon (Ar) atmosphere. All measurements were performed with Ar bubbling into the electrochemical cell for 15 minutes 10 seconds prior to the measurements; the Ar was turned to "blanket-mode". Platinum wires (99.99%) were used as working and pseudo-reference electrodes and platinum gauze (55 mesh, 99.9%) as counter electrode. Tetrabutylammonium hexafluorophosphate ($TBAPF_6$, 98%) was used as the electrolyte and was recrystallized three times from acetone and dried in vacuum at 100 °C before each experiment. Measurements were recorded using an EG&G Princeton Applied Research potentiostat/galvanostat Model Verstastat 3 connected to a personal computer running VersaStudio software. The scan rate was kept constant for all CV runs at 100 mV/s. All results were calibrated using commercially available ferrocene (purified by sublimation) as internal standard. All samples were studied in anhydrous DCM solution. To calculate HOMO/LUMO levels, using the potentials obtained the following equations from Cardona et al. were used:[87]

$E_{HOMO} = 2\ (E_{[ox\ vs.\ Fc/Fc+]} + 5.1)\ (eV)$ $E_{LUMO} = 2\ (E_{[red\ vs.\ Fc/Fc+]} + 5.1)\ (eV)$

For HOMO–LUMO estimations, the $E_{1/2}$ of the reversible process was considered. For conversions to NHE, a value of -4.5 eV was used as equivalent to 0.0 V vs. NHE.[88]

Bibliography

1. EIA projects nearly 50% increase in world energy usage by 2050, led by growth in Asia; U.S Energy Department, (Accessed 28.05.2020). **2019**.
2. Markandya A, Wilkinson P. Electricity generation and health. The Lancet. **2007**;370(9591):979-90.
3. Buene AF. Molecular Engineering and Photovoltaic Evaluation of Phenothiazine and Triarylamine Dyes for Dye-Sensitized Solar Cells: PhD Thesis, Department of Chemistry NTNU (Trondheim); **2019**.
4. Burschka J, Pellet N, Moon SJ, Humphry-Baker R, Gao P, Nazeeruddin MK, et al. Sequential deposition as a route to high-performance perovskite-sensitized solar cells. *Nature*. **2013**;499(7458):316-9.
5. Tibbits TND, Beutel P, Grave M, Karcher C, Oliva E, Siefer G, et al. NEW EFFICIENCY FRONTIERS WITH WAFER-BONDED MULTI-JUNCTION SOLAR CELLS. **2014**.
6. Hagfeldt A, Boschloo G, Sun L, Kloo L, Pettersson H. Dye-Sensitized Solar Cells. *Chem. Rev.*. **2010**;110(11):6595-663.
7. Becquerel AE. Recherches sur les effets de la radiation chimique de la lumiere solaire au moyen des courants electriques. *C. R. Acad. Sci*. **1839**;9.
8. Fraas L. Chapter 1: History of Solar Cell Development. **2014**.
9. Einstein A. Über einen die Erzeugung und Verwandlung des Lichtes betreffenden heuristischen Gesichtspunkt. *Ann. Phys*. **1905**;322(6):132-48.
10. Hagfeldt A, Graetzel M. Light-Induced Redox Reactions in Nanocrystalline Systems. *Chem. Rev*. **1995**;95(1):49-68.
11. Ramamurthy V, Schanze KS. Semiconductor photochemistry and photophysics. New York: Marcel Dekker; **2003**.
12. Kohjiro Hara NK. Organic Dyes for Efficient and Stable Dye-Sensitized Solar Cells. *Material Matters*. **2009**;4(4):92.
13. Huang Z-S, Meier H, Cao D. Phenothiazine-based Dyes for Efficient Dye-Sensitized Solar Cells. *J. Mater. Chem. C*. **2016**;4.
14. Shafiee A, Mat Salleh M, Yahaya M. Determination of HOMO and LUMO of [6,6]-Phenyl C61-butyric Acid 3-ethylthiophene Ester and Poly (3-octyl-thiophene-2, 5-diyl) through Voltametry Characterization. *Sains. Malays*. **2011**;40:173-6.
15. O'Regan B, Grätzel M. A low-cost, high-efficiency solar cell based on dye-sensitized colloidal TiO2 films. *Nature*. **1991**;353(6346):737-40.
16. Amadelli R, Argazzi R, Bignozzi CA, Scandola F. Design of antenna-sensitizer polynuclear complexes. Sensitization of titanium dioxide with [Ru(bpy)2(CN)2]2Ru(bpy(COO)2)22. *J. Am. Chem. Soc.* **1990**;112(20):7099-103.
17. Nazeeruddin M, Angelis F, Fantacci S, Selloni A, Viscardi G, Liska P, et al. Combined Experimental and DFT-TDDFT Computational Study of Photoelectrochemical Cell Ruthenium Sensitizers. *J. Am. Chem. Soc*. **2006**;127:16835-47.
18. Antonia Luque SH. Dye-sensitized solar cells. Handbook of Photovoltaic Science and Engineering: John Wiley & Sons; **2003**. p. 663-700.
19. Błaszczyk A. Strategies to improve the performance of metal-free dye-sensitized solar cells. *Dyes Pigm*. **2018**;149:707-18.
20. Wild M, Griebel J, Hajduk A, Friedrich D, Stark A, Abel B, et al. Efficient synthesis of triarylamine-based dyes for p-Type dye-sensitized solar cells. *Sci. Rep*. **2016**;6:26263.
21. Al-horaibi SA, Asiri AM, El-Shishtawy RM, Gaikwad ST, Rajbhoj AS. Synthesis and characterization of new squaraine dyes with bis-pendent carboxylic groups for dye-sensitized solar cells. *J. Mol. Struct.* **2019**;1195:850-8.

22. Sánchez-de-Armas R, San Miguel MÁ, Oviedo J, Sanz JF. Coumarin derivatives for dye sensitized solar cells: a TD-DFT study. *Phys. Chem.* **2012**;14(1):225-33.
23. Ohlow MJ, Moosmann B. Phenothiazine: the seven lives of pharmacology's first lead structure. *Drug Discov. Today*. **2011**;16(3):119-31.
24. Tian H, Yang X, Chen R, Pan Y, Li L, Hagfeldt A, et al. Phenothiazine derivatives for efficient organic dye-sensitized solar cells. *Chem. Comm*. **2007**(36):3741-3.
25. Basheer B, Mathew D, George BK, Reghunadhan Nair CP. An overview on the spectrum of sensitizers: The heart of Dye Sensitized Solar Cells. *Sol. Energy*. **2014**;108:479-507.
26. Li C-T, Kuo Y-L, Kumar CHP, Huang P-T, Lin JT. Tetraphenylethylene tethered phenothiazine-based double-anchored sensitizers for high performance dye-sensitized solar cells. *J. Mat. Chem. A*. **2019**;7(40):23225-33.
27. Buene AF, Boholm N, Hagfeldt A, Hoff BH. Effect of furan π-spacer and triethylene oxide methyl ether substituents on performance of phenothiazine sensitizers in dye-sensitized solar cells. *New J. Chem*. **2019**;43(24):9403-10.
28. Marszalek M, Nagane S, Ichake A, Humphry-Baker R, Paul V, Zakeeruddin SM, et al. Tuning spectral properties of phenothiazine based donor–π–acceptor dyes for efficient dye-sensitized solar cells. *J. Mat. Chem*. **2012**;22(3):889-94.
29. Hagberg DP, Marinado T, Karlsson KM, Nonomura K, Qin P, Boschloo G, et al. Tuning the HOMO and LUMO Energy Levels of Organic Chromophores for Dye Sensitized Solar Cells. *J. Org. Chem*. **2007**;72(25):9550-6.
30. Luo J-S, Wan Z-Q, Jia C-Y. Recent advances in phenothiazine-based dyes for dye-sensitized solar cells. *Chinese Chem. Lett*. **2016**;27(8):1304-18.
31. Wu K-j, Shen K, Yu Y, Wang D-l. Effect of Surface Protonation on Device Performance and Dye Stability of Dye-sensitized TiO2 Solar Cell. *Chinese J. Chem.Phys*. **2012**;25(6):733-8.
32. Kalyanasundaram K, Grätzel M. Applications of functionalized transition metal complexes in photonic and optoelectronic devices. *Coord. Chem. Rev*. **1998**;177(1):347-414.
33. Zhang L, Cole JM. Anchoring Groups for Dye-Sensitized Solar Cells. *ACS Appl. Mater. Inter.* **2015**;7(6):3427-55.
34. Ooyama Y, Furue K, Enoki T, Kanda M, Adachi Y, Ohshita J. Development of type-I/type-II hybrid dye sensitizer with both pyridyl group and catechol unit as anchoring group for type-I/type-II dye-sensitized solar cell. *Phys. Chem*. **2016**;18(44):30662-76.
35. Chen W-C, Nachimuthu S, Jiang J-C. Revealing the influence of Cyano in Anchoring Groups of Organic Dyes on Adsorption Stability and Photovoltaic Properties for Dye-Sensitized Solar Cells. *Sci. Rep*. **2017**;7(1):4979.
36. Ooyama Y, Uenaka K, Kamimura T, Ozako S, Kanda M, Koide T, et al. Dye-sensitized solar cell based on an inclusion complex of a cyclic porphyrin dimer bearing four 4-pyridyl groups and fullerene C60. *RSC Adv*. **2016**;6(20):16150-8.
37. Shibayama N, Ozawa H, Abe M, Ooyama Y, Arakawa H. A new cosensitization method using the Lewis acid sites of a TiO2 photoelectrode for dye-sensitized solar cells. *Chem. Comm*. **2014**;50(48):6398-401.
38. Venkatraman V, Yemene AE, de Mello J. Prediction of Absorption Spectrum Shifts in Dyes Adsorbed on Titania. *Sci. Rep*. **2019**;9(1):16983.
39. Kumar D, Thomas KRJ, Lee C-P, Ho K-C. Novel Pyrenoimidazole-Based Organic Dyes for Dye-Sensitized Solar Cells. *Org. Lett.* **2011**;13(10):2622-5.
40. Hua Y, Chang S, Wang H, Huang D, Zhao J, Chen T, et al. New phenothiazine-based dyes for efficient dye-sensitized solar cells: Positioning effect of a donor group on the cell performance. *J. Power Sources*. **2013**;243:253-9.
41. Zhang L, Cole JM. Dye aggregation in dye-sensitized solar cells. *J. Mat. Chem. A*. **2017**;5(37):19541-59.
42. Francis A. Carey RJS. Advanced Organic Chemistry Part B: Reactions and Synthesis. 5 ed. University of Virginia: Springer; **2007**.
43. Solomons TWG, Fryhle CB. Organic chemistry. 10 ed: John Wiley & Sons; **2011**.

44. Jutz C, Müller W. Über die Vilsmeier-Formylierung von ungesättigten Kohlenwasserstoffen, II. *Chem. Ber*. **1967**;100(5):1536-43.
45. Dewick PM. Essentials of organic chemistry : for students of pharmacy, medicinal chemistry and biological chemistry. **2006**.
46. Cioffi CL, Spencer WT, Richards JJ, Herr RJ. Generation of 3-Pyridyl Biaryl Systems via Palladium-Catalyzed Suzuki Cross-Couplings of Aryl Halides with 3-Pyridylboroxin. *J. Org. Chem.* **2004**;69(6):2210-2.
47. Hassan J, Sévignon M, Gozzi C, Schulz E, Lemaire M. Aryl−Aryl Bond Formation One Century after the Discovery of the Ullmann Reaction. *Chem. Rev*. **2002**;102(5):1359-470.
48. Lennox AJJ, Lloyd-Jones GC. Transmetalation in the Suzuki–Miyaura Coupling: The Fork in the Trail. *Angew. Chem. Int. Ed*. **2013**;52(29):7362-70.
49. Amatore C, Jutand A, Le Duc G. Kinetic Data for the Transmetalation/Reductive Elimination in Palladium-Catalyzed Suzuki–Miyaura Reactions: Unexpected Triple Role of Hydroxide Ions Used as Base. *Chem. Eur*. **2011**;17(8):2492-503.
50. Martin R, Buchwald SL. Palladium-Catalyzed Suzuki−Miyaura Cross-Coupling Reactions Employing Dialkylbiaryl Phosphine Ligands. *Acc. Chem. Res.* **2008**;41(11):1461-73.
51. Busch M, Wodrich MD, Corminboeuf C. A Generalized Picture of C–C Cross-Coupling. *ACS Catal*. **2017**;7(9):5643-53.
52. Suzuki A. Recent advances in the cross-coupling reactions of organoboron derivatives with organic electrophiles, 1995–1998. *J. Organomet. Chem*. **1999**;576(1):147-68.
53. Lima CFRAC, Rodriguez-Borges JE, Santos LMNBF. Exploring the selectivity of the Suzuki–Miyaura cross-coupling reaction in the synthesis of arylnaphthalenes. *Tetrahedron*. **2011**;67(4):689-97.
54. Khare R, Pandey J, Smriti S, Ruchi R. The Importance and Applications of Knoevenagel Reaction (Brief Review). *Orient. J. Chem*. **2019**;35:423-9.
55. Stenhouse J. Ueber die entfärbenden und desinficirenden Eigenschaften der Holzkohle, nebst Beschreibung eines Kohle-Respirators zur Reinigung der Luft durch Filtration. *Justus Liebigs Ann. Chem*. **1854**;90(2):186-90.
56. Kellogg RM. 1.3 - Reduction of CX to CHXH by Hydride Delivery from Carbon. In: Trost BM, Fleming I, editors. Comprehensive Organic Synthesis. Oxford: Pergamon; **1991**. p. 79-106.
57. Stille JK. The Palladium-Catalyzed Cross-Coupling Reactions of Organotin Reagents with Organic Electrophiles [New Synthetic Methods (58)]. *Angew. Chem. Int. Ed*. **1986**;25(6):508-24.
58. Mee SPH, Lee V, Baldwin JE. Significant Enhancement of the Stille Reaction with a New Combination of Reagents—Copper(I) Iodide with Cesium Fluoride. *Chem. Eur*. **2005**;11(11):3294-308.
59. Negishi E, Takahashi T, Baba S, Van Horn DE, Okukado N. Nickel- or palladium-catalyzed cross coupling. 31. Palladium- or nickel-catalyzed reactions of alkenylmetals with unsaturated organic halides as a selective route to arylated alkenes and conjugated dienes: scope, limitations, and mechanism. *J. Am. Chem. Soc*. **1987**;109(8):2393-401.
60. Mee SPH, Lee V, Baldwin JE. Stille Coupling Made Easier—The Synergic Effect of Copper(I) Salts and the Fluoride Ion. *Angew. Chem. Int. Ed.* **2004**;43(9):1132-6.
61. Nagaraju S, Ravindran E, Varathan E, Subramanian V, Somanathan N. White electroluminescence from a single polymer system: phenothiazine derivatives as a red emissive dopant and polyfluorene as a blue host. *RSC Adv*. **2016**;6(95):92778-85.
62. Buene AF, Uggerud N, Economopoulos SP, Gautun OR, Hoff BH. Effect of π-linkers on phenothiazine sensitizers for dye-sensitized solar cells. *Dyes Pigm*. **2018**;151:263-71.
63. Hua Y, Chang S, Huang D, Zhou X, Zhu X, Zhao J, et al. Significant Improvement of Dye-Sensitized Solar Cell Performance Using Simple Phenothiazine-Based Dyes. *Chem. Mater.* **2013**;25(10):2146-53.
64. Almenningen DM. Synthesis of Phenothiazine Dyes for Dye-Sensitized Solar Cells (DSSC): Masters Thesis, Department of Chemistry, NTNU (Trondheim); **2016**.
65. Vold M. Syntese of karakterisering av nye fenotiazin-fargestoffer til Dye-Sensitized Solar Cells (DSSC): Masters Thesis, Department of Chemistry, NTNU (Trondheim); **2017**.

66. Bejan A, Shova S, Damaceanu M-D, Simionescu BC, Marin L. Structure-Directed Functional Properties of Phenothiazine Brominated Dyes: Morphology and Photophysical and Electrochemical Properties. *Cryst. Growth Des.* **2016**;16(7):3716-30.
67. Jayaraman A, East ALL. The Mechanism of Permanganate Oxidation of Sulfides and Sulfoxides. *J. Org. Chem*. **2012**;77(1):351-6.
68. Sato K, Hyodo M, Aoki M, Zheng X-Q, Noyori R. Oxidation of sulfides to sulfoxides and sulfones with 30% hydrogen peroxide under organic solvent- and halogen-free conditions. *Tetrahedron*. **2001**;57(13):2469-76.
69. Purrington ST, Glenn AG. MILD SELECTIVE OXIDATION OF SULFIDES TO SULFONES. *Org. Prep. Proced. Int*. **1985**;17(3):227-30.
70. Irimie F-D, Paizs C, Tosa M, Majdik C, Moldovan P, Caprioara M, et al. Cannizzaro reaction in the phenothiazine series. Stud Univ Babes-Bolyai, *Chem*. **2000**;45(1-2):39-46.
71. Weiss J. Mechanism of the Cannizzaro reaction and some allied processes. *Trans. Faraday Soc*. **1941**;37(0):782-91.
72. Martinelli C, Cardone A, Pinto V, Mastropasqua Talamo M, D'arienzo ML, Mesto E, et al. Synthesis and Structure of Conjugated Molecules with the Benzofulvene Core. *Org. Lett*. **2014**;16(13):3424-7.
73. Cochran JC. The Stille Reaction (Farina, Vittorio; Krishnamurthy, Venkat; Scott, William J.). *J. Chem. Educ*. **1999**;76(10):1344.
74. Gao J, Wang W, Zhang S, Xiao S, Zhan C, Yang M, et al. Distinction between PTB7-Th samples prepared from Pd(PPh3)4 and Pd2(dba)3/P(o-tol)3 catalysed stille coupling polymerization and the resultant photovoltaic performance. *J. Mat. Chem. A*. **2018**;6(1):179-88.
75. Littke AF, Schwarz L, Fu GC. Pd/P(t-Bu)3: A Mild and General Catalyst for Stille Reactions of Aryl Chlorides and Aryl Bromides. *J. Am. Chem. Soc*. **2002**;124(22):6343-8.
76. De Meijere A, Bräse S, Oestreich M. Metal Catalyzed Cross-Coupling Reactions and More : 3 Volume Set. **2014**.
77. Jia H-L, Peng Z-J, Chen Y-C, Huang C-Y, Guan M-Y. Highly efficient stereoscopic phenothiazine dyes with different anchors for dye-sensitized solar cells. *New J. Chem*. **2018**;42(23):18702-7.
78. Kudo N, Perseghini M, Fu GC. A Versatile Method for Suzuki Cross-Coupling Reactions of Nitrogen Heterocycles. *Angew. Chem. Int. Ed*. **2006**;45(8):1282-4.
79. Kinzel T, Zhang Y, Buchwald SL. A New Palladium Precatalyst Allows for the Fast Suzuki−Miyaura Coupling Reactions of Unstable Polyfluorophenyl and 2-Heteroaryl Boronic Acids. *J. Am. Chem. Soc*. **2010**;132(40):14073-5.
80. Silverstein R, Webster F, Kiemle D, Bryce D. Spectrometric Identification of Organic Compounds. Eight ed: Wiley; **2015**.
81. Blanch JH. Determination of the Hammett substituent constants for the 2-, 3-, and 4-pyridyl and -pyridinium groups. *J. Chem. Soc. B*. **1966**(0):937-9.
82. Perrin DD, Dempsey B, Serjeant EP. PKa prediction for organic acids and bases. London; New York: Chapman and Hall; **1981**.
83. Elsayed MA. Successive advanced oxidation of pyridine by ultrasonic irradiation: effect of additives and kinetic study. *Desalination Water Treat*. **2015**;53(1):57-65.
84. Buene AF, Almenningen DM, Hagfeldt A, Gautun OR, Hoff BH. First Report of Chenodeoxycholic Acid–Substituted Dyes Improving the Dye Monolayer Quality in Dye-Sensitized Solar Cells. *Sol. RRL*. **2020**;4(4):1900569.
85. Kringhaug HH. Synthesis and Characterization of New Organic Dyes for Dye-Sensitized Solar Cells (DSSC): Masters Thesis, Department of Chemistry NTNU (Trondheim); **2016**.
86. Hora C, Santos F, Sales MGF, Ivanou D, Mendes A. Dye-Sensitized Solar Cells for Efficient Solar and Artificial Light Conversion. *ACS Sustain. Chem. Eng*. **2019**;7(15):13464-70.
87. Cardona CM, Li W, Kaifer AE, Stockdale D, Bazan GC. Electrochemical Considerations for Determining Absolute Frontier Orbital Energy Levels of Conjugated Polymers for Solar Cell Applications. *Adv. Mater*. **2011**;23(20):2367-71.

88. Allen J. Bard and Larry R. Faulkner, Electrochemical Methods: Fundamentals and Applications, New York: Wiley, 2001, 2nd ed. *Russ. J. Electrochem*. **2002**;38(12):1364-5.

Appendix

A 10-hexyl-10*H*-phenothiazine (2)

A.1 ^{1}H NMR of 2

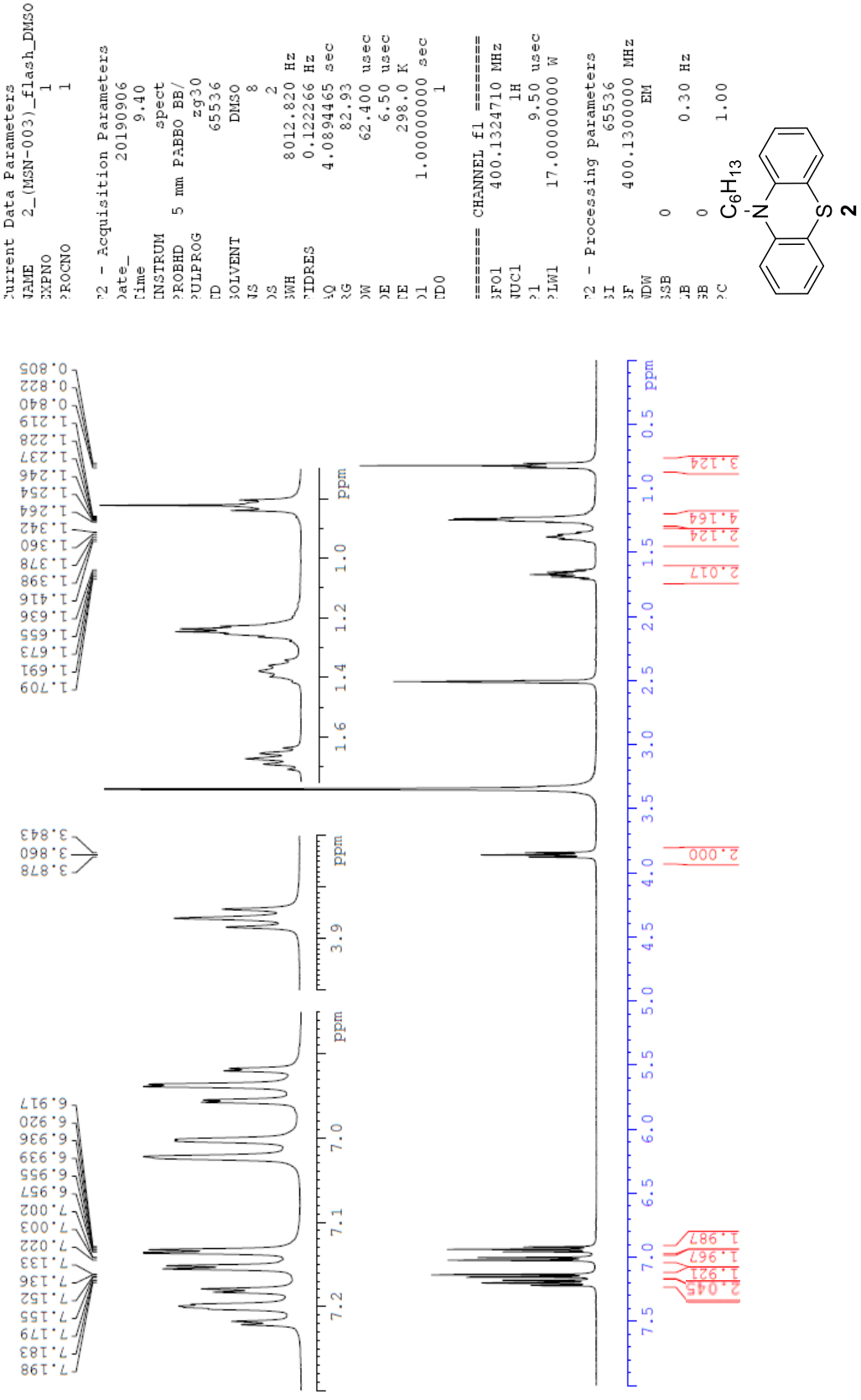

B 10-hexyl-10*H*-phenothiazine-3-carbaldehyde (3)

B.1 ^{1}H NMR of 3

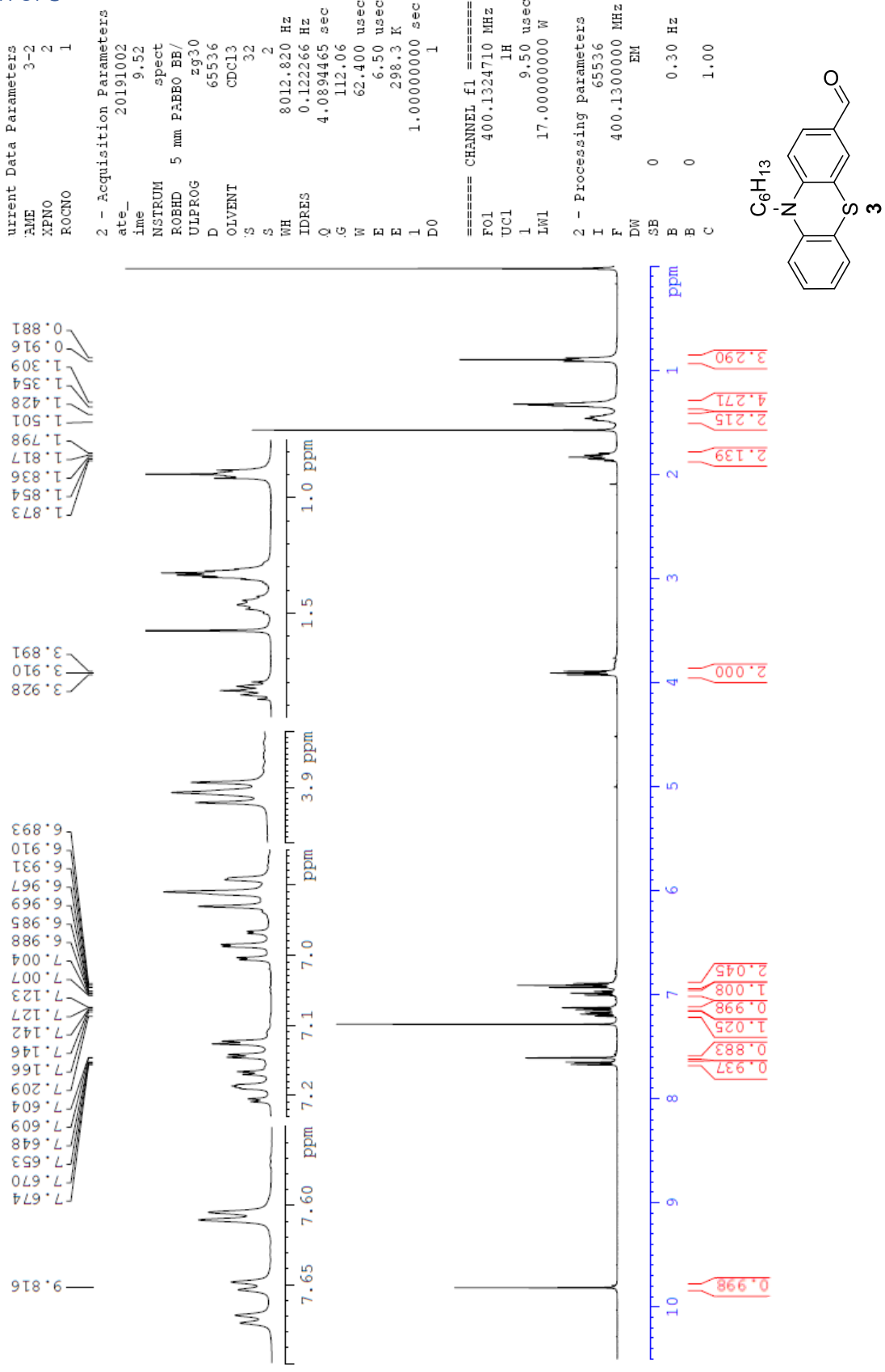

C 7-bromo-10-hexyl-10H-phenothiazine-3-carbaldehyde (4)

C.1 ^{1}H NMR of 4

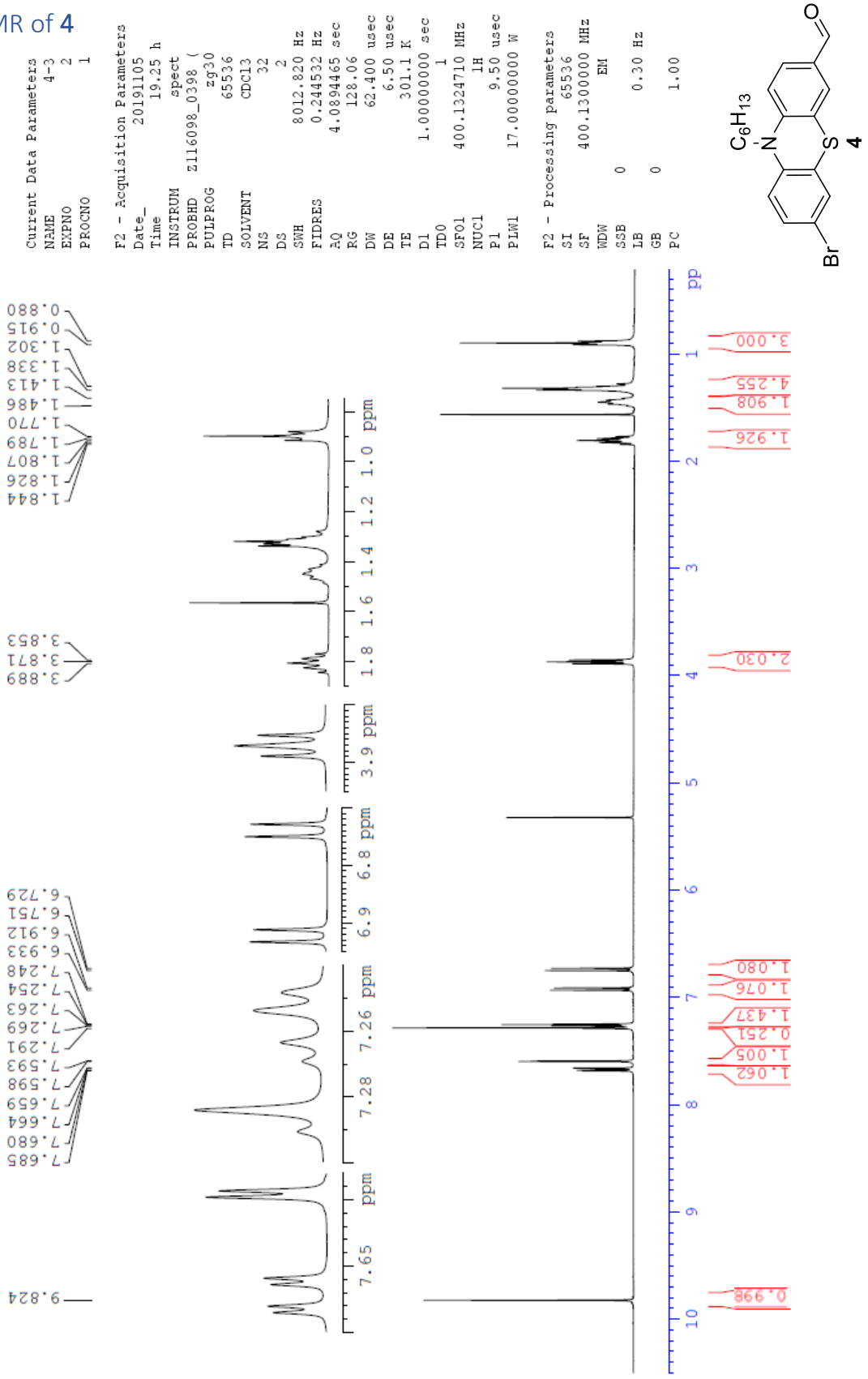

D 10-hexyl-7-(4-methoxyphenyl)-10*H*-phenothiazine-3-carbaldehyde (5)

D.1 ^{1}H NMR of **5**

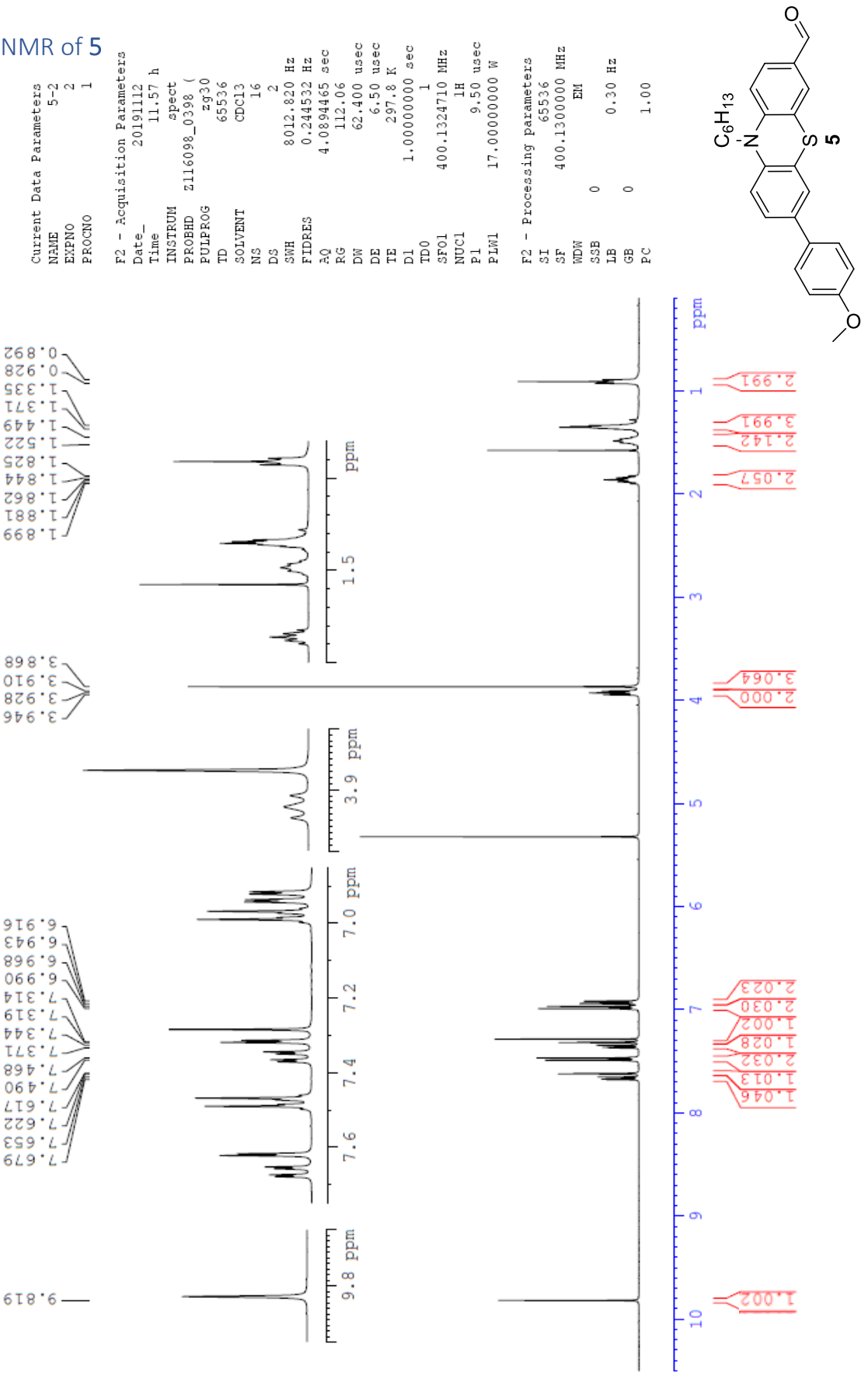

E 3,7-dibromo-10-hexyl-10*H*-phenothiazine (**7**)

E.1 ^{1}H NMR of **7**

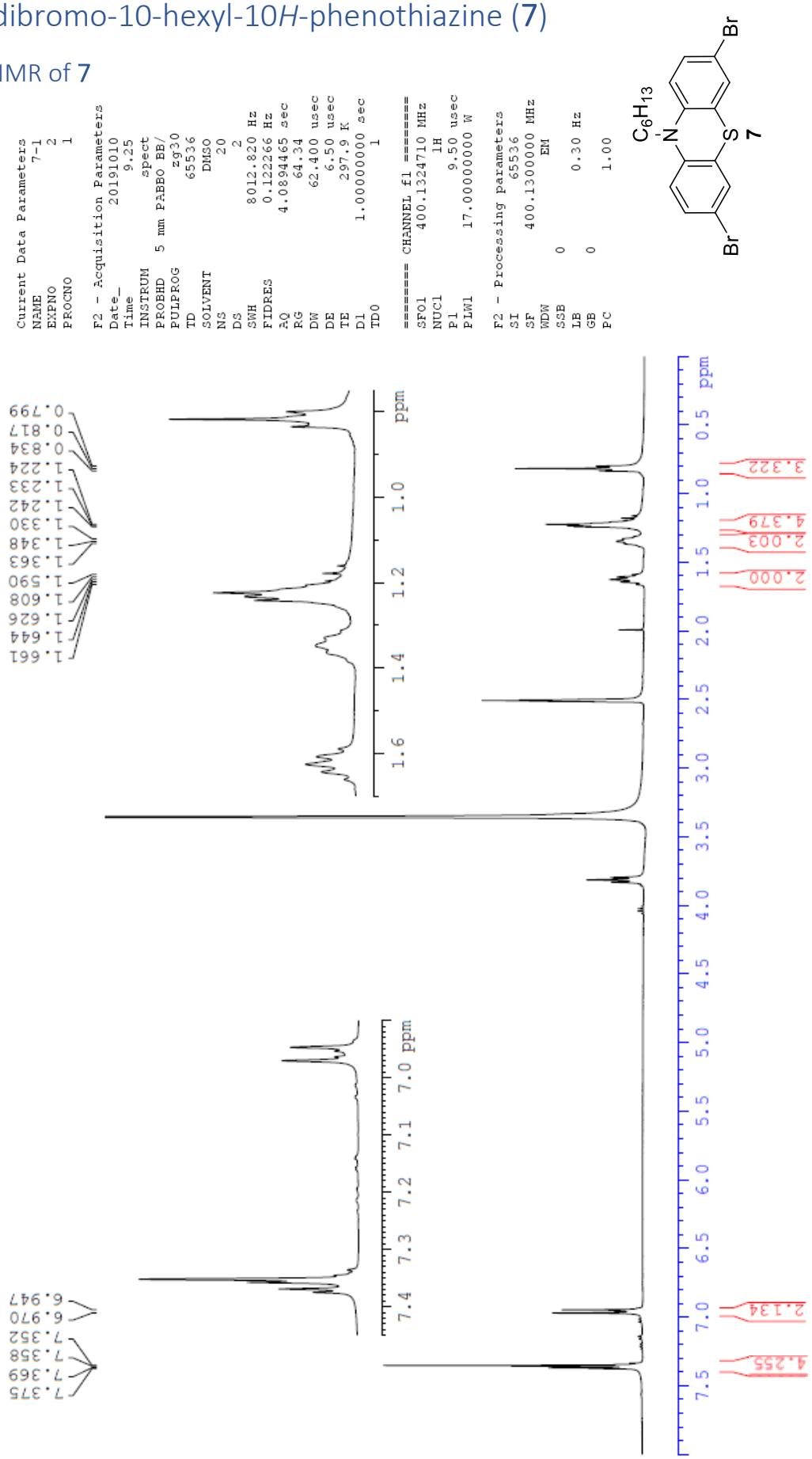

F 3-bromo-10-hexyl-7-(4-methoxyphenyl)-10*H*-phenothiazine (8)

F.1 ^{1}H NMR of 8

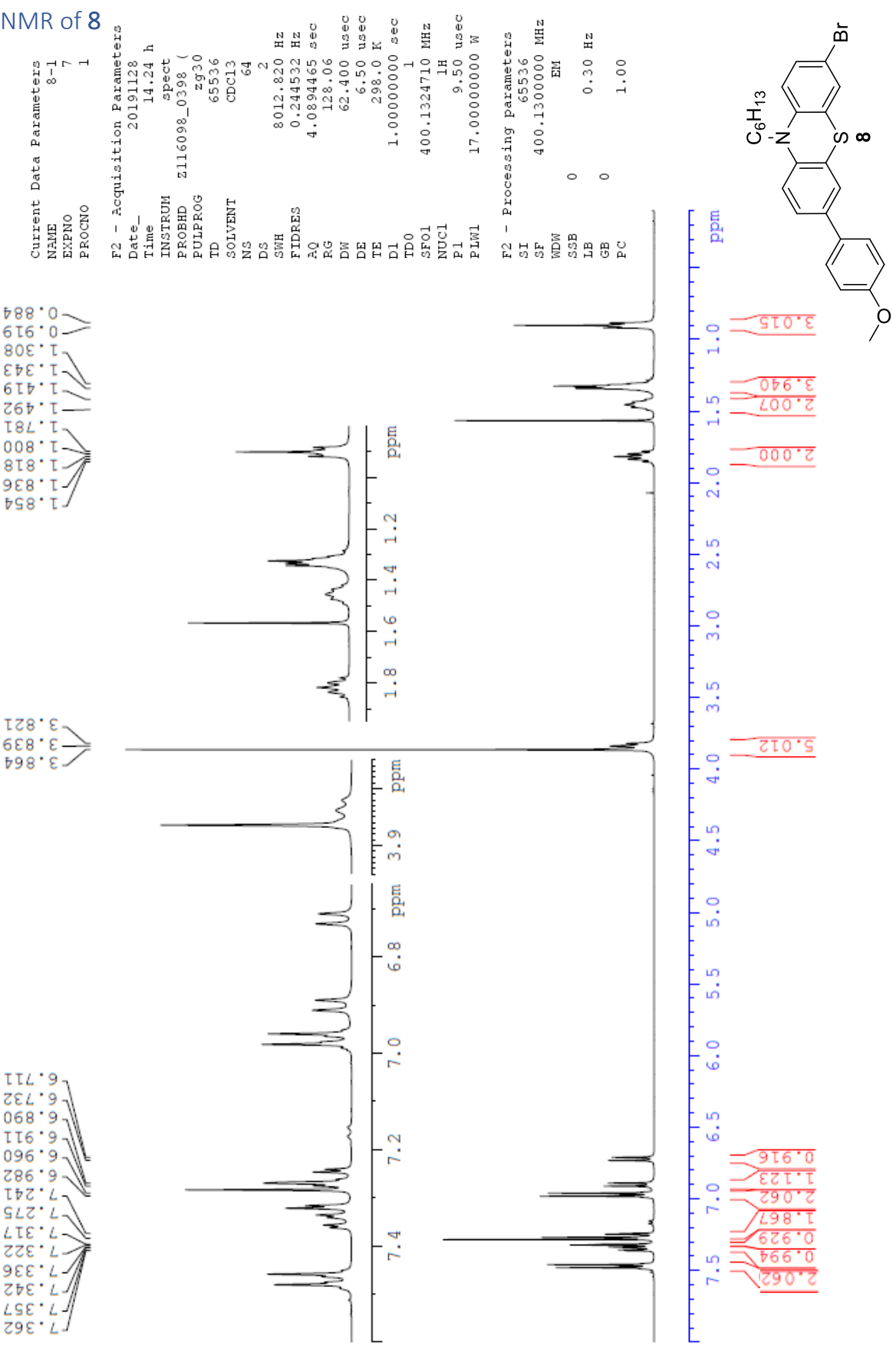

G (*E*)-2-cyano-3-(10-hexyl-7-(4-methoxyphenyl)-10*H*-phenothiazin-3-yl)acrylic acid (**MSN-003**)

G.1 ^{1}H NMR of **MSN-003**

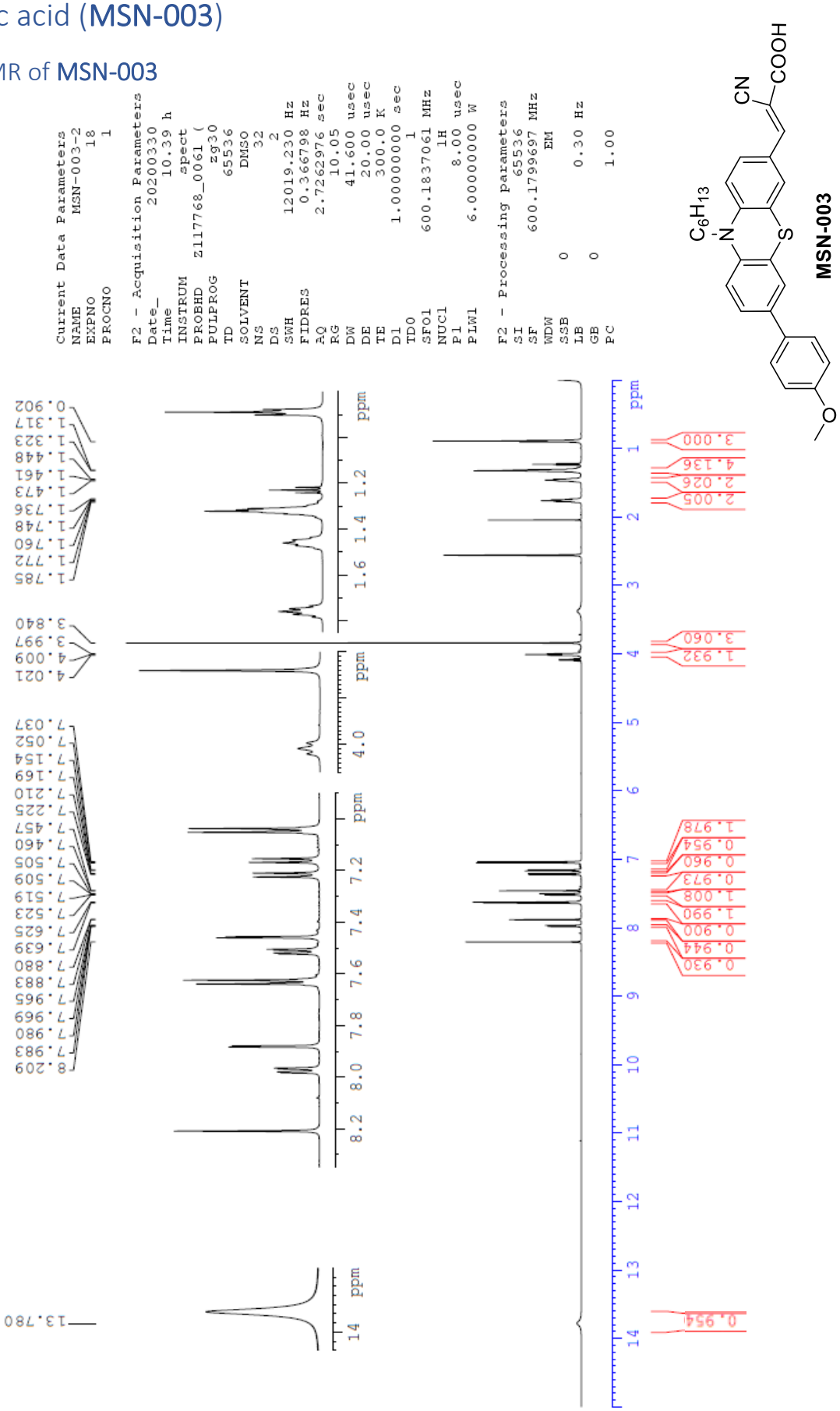

G.2 ^{13}C NMR of **MSN-003**

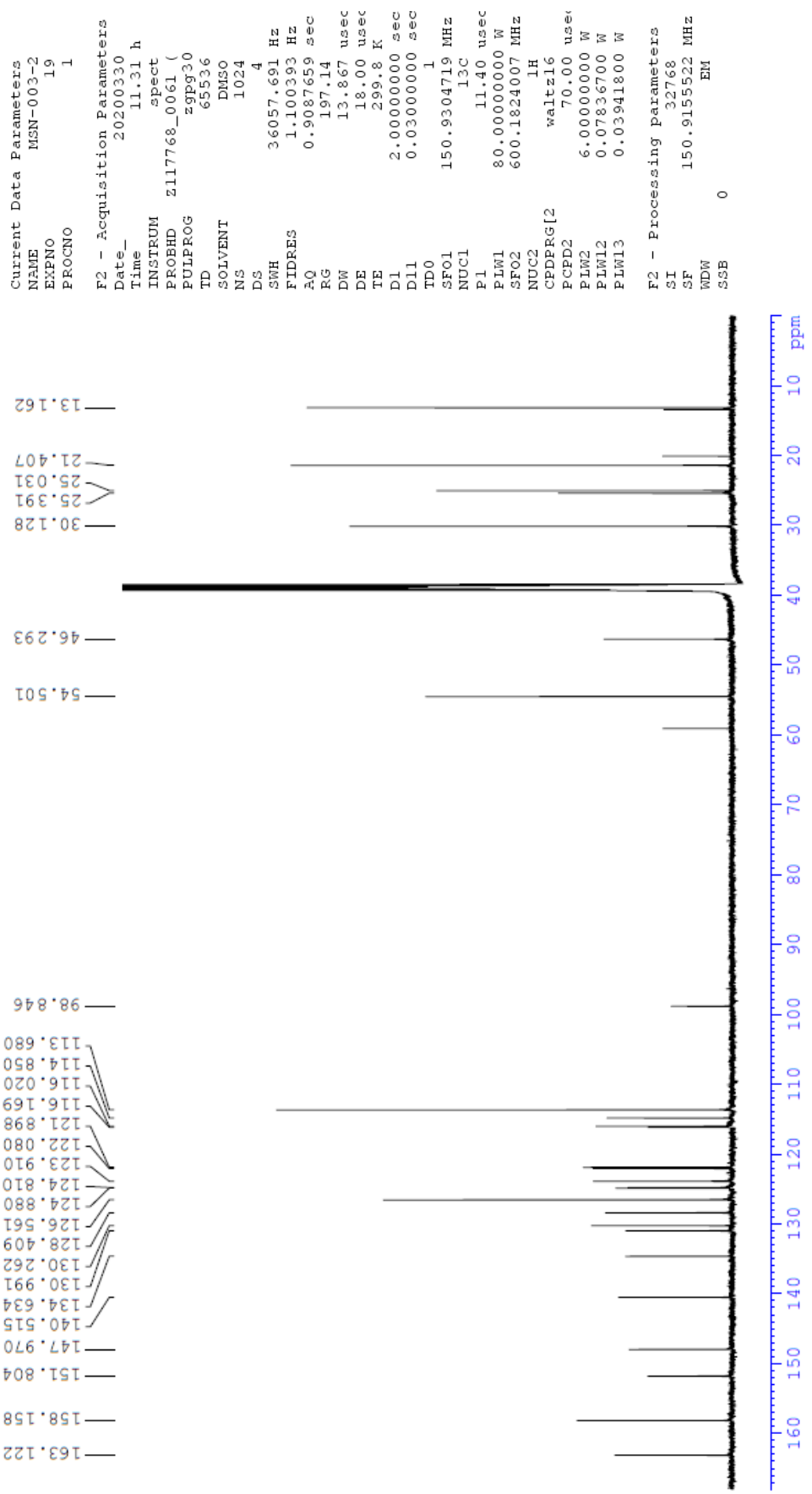

G.3 ^{1}H-^{1}H COSY of **MSN-003**

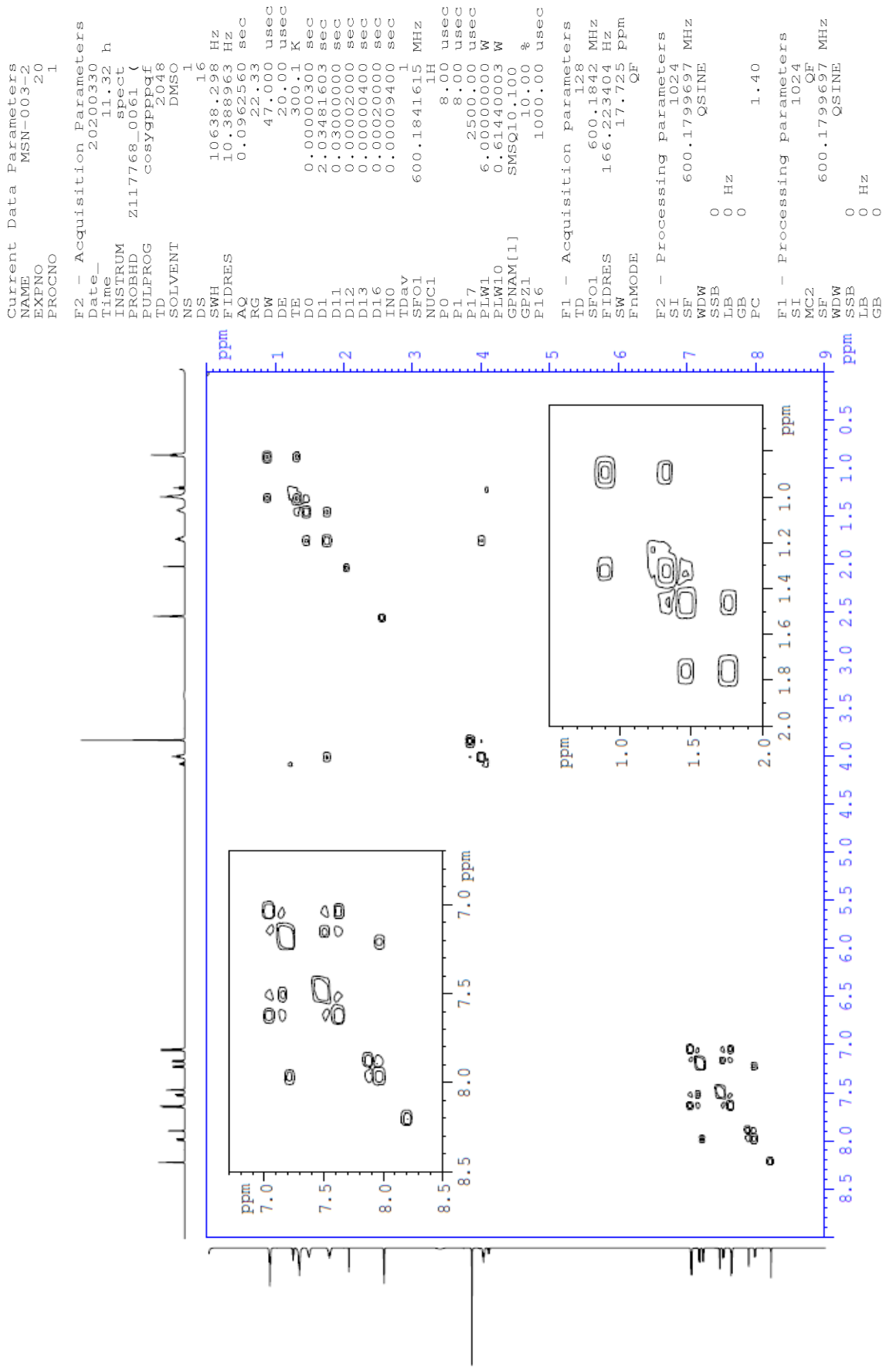

G.4 ^{1}H-^{13}C HSQC of **MSN-003**

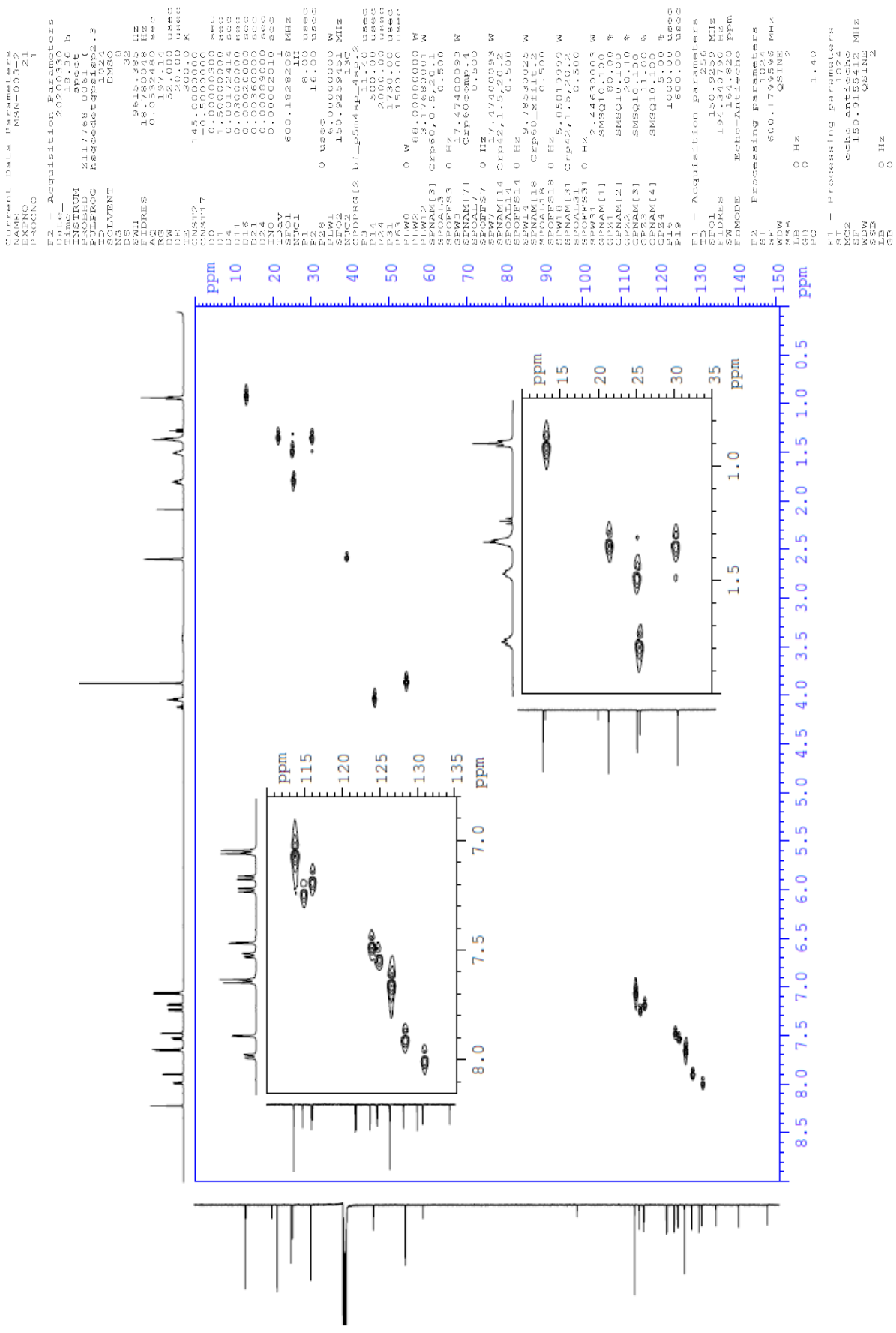

G.5 ^{13}C-^{13}C HMBC of MSN-003

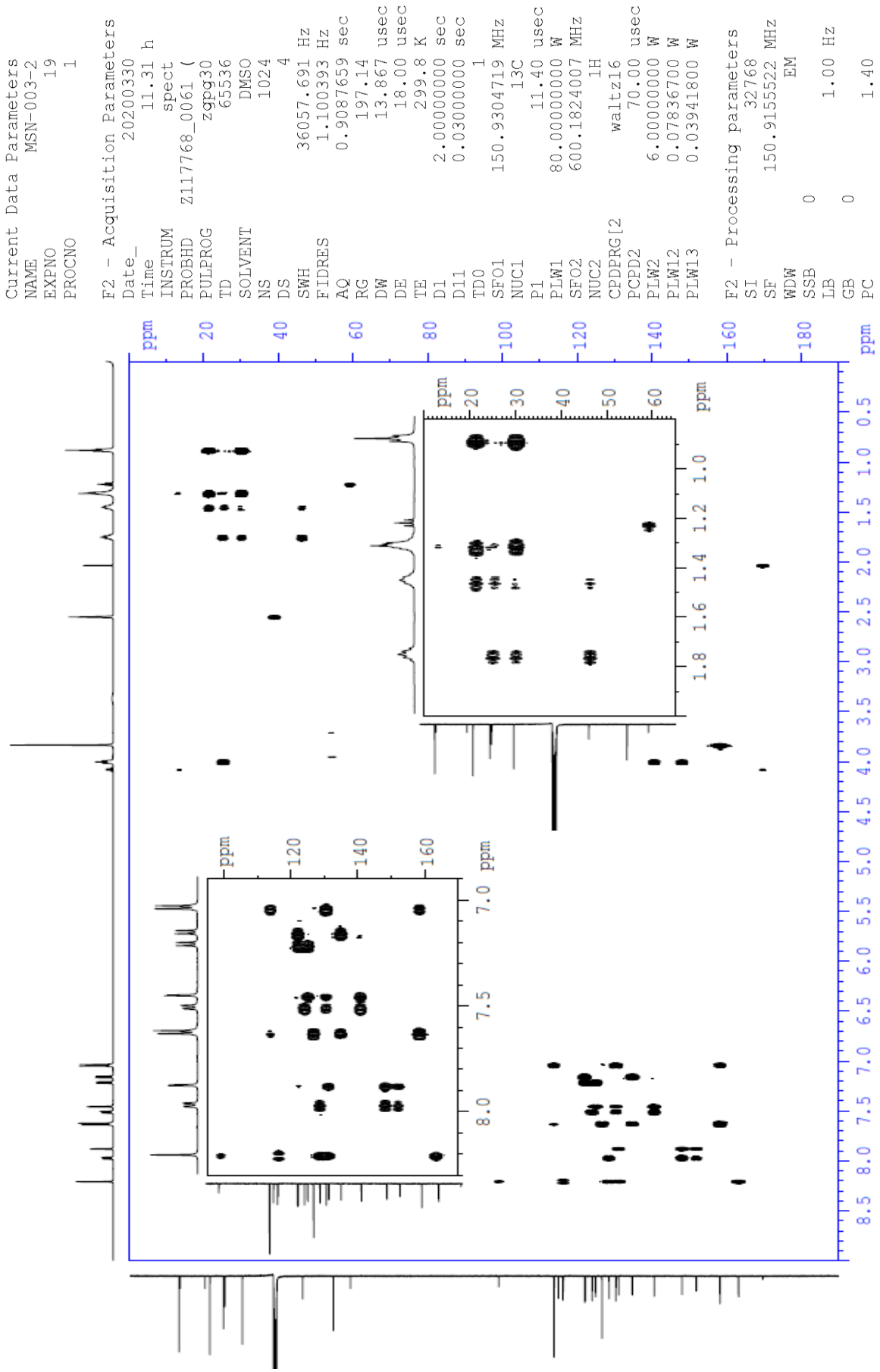

G.6 HRMS of MSN-003

Elemental Composition Report **Page 1**

Single Mass Analysis
Tolerance = 2.0 PPM / DBE: min = -50.0, max = 50.0
Element prediction: Off
Number of isotope peaks used for i-FIT = 3

Monoisotopic Mass, Even Electron Ions
4186 formula(e) evaluated with 7 results within limits (all results (up to 1000) for each mass)
Elements Used:
C: 0-100 H: 0-100 N: 0-10 O: 0-10 S: 0-3
2019-769 261 (5.082) AM2 (Ar,35000.0,0.00,0.00); Cm (257:261)
1: TOF MS ASAP+

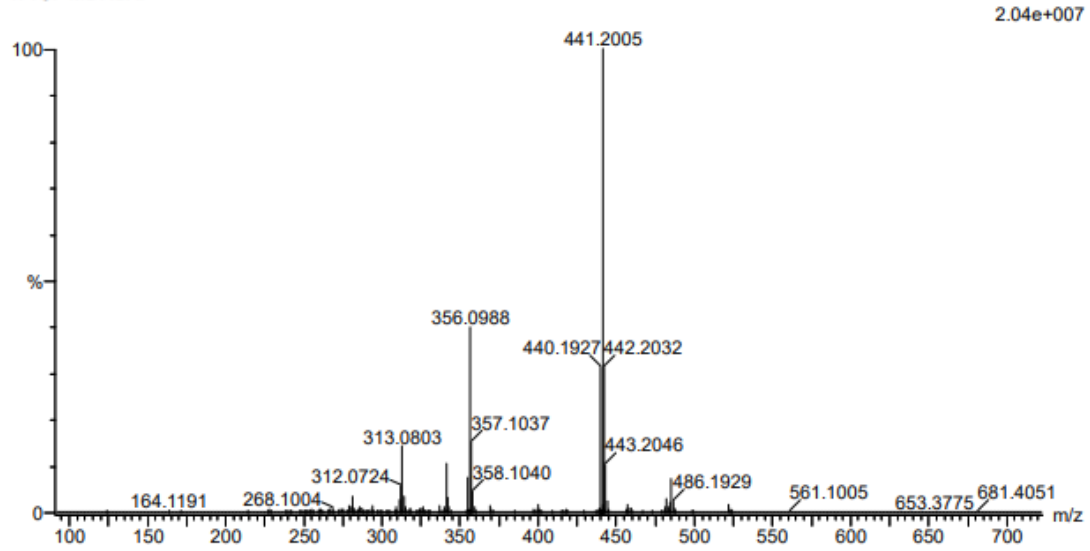

Minimum:				-50.0				
Maximum:		5.0	2.0	50.0				
Mass	Calc. Mass	mDa	PPM	DBE	i-FIT	Norm	Conf(%)	Formula
485.1898	485.1897	0.1	0.2	13.5	1020.5	12.400	0.00	C21 H25 N8 O6
	485.1899	-0.1	-0.2	3.5	1023.3	15.202	0.00	C14 H33 N10 O3 S3
	485.1899	-0.1	-0.2	16.5	1008.1	0.000	99.99	C29 H29 N2 O3 S
	485.1892	0.6	1.2	7.5	1019.5	11.463	0.00	C21 H33 N4 O5 S2
	485.1905	-0.7	-1.4	25.5	1021.4	13.355	0.00	C37 H25 O
	485.1891	0.7	1.4	4.5	1020.3	12.218	0.00	C13 H29 N10 O8 S
	485.1906	-0.8	-1.6	12.5	1018.3	10.205	0.00	C22 H29 N8 O S2

G.7 FT-IR of MSN-003 (neat)

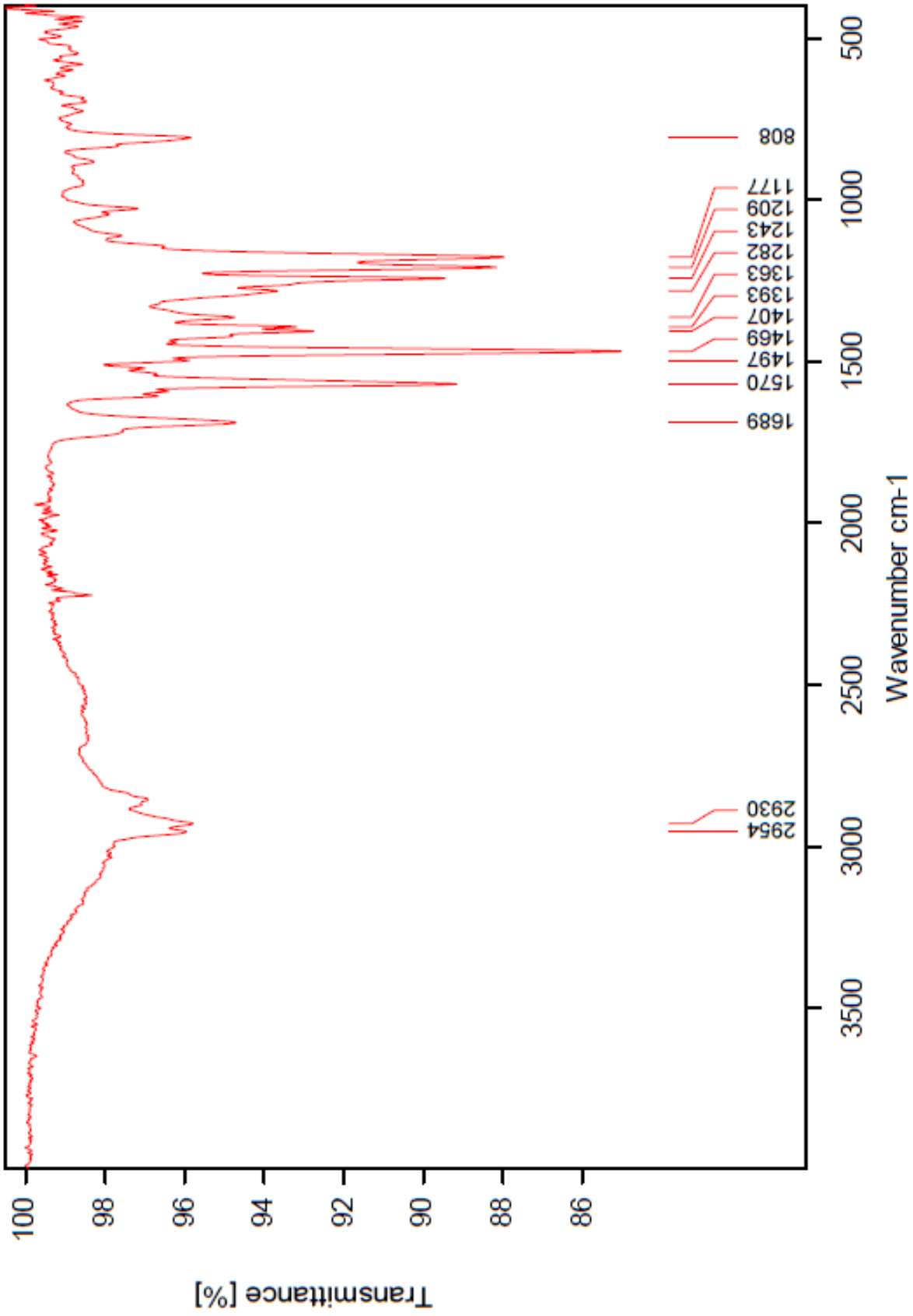

G.8 UV-Vis of MSN-003 in DCM

Report Date: 12:41:54, 12/02/2019

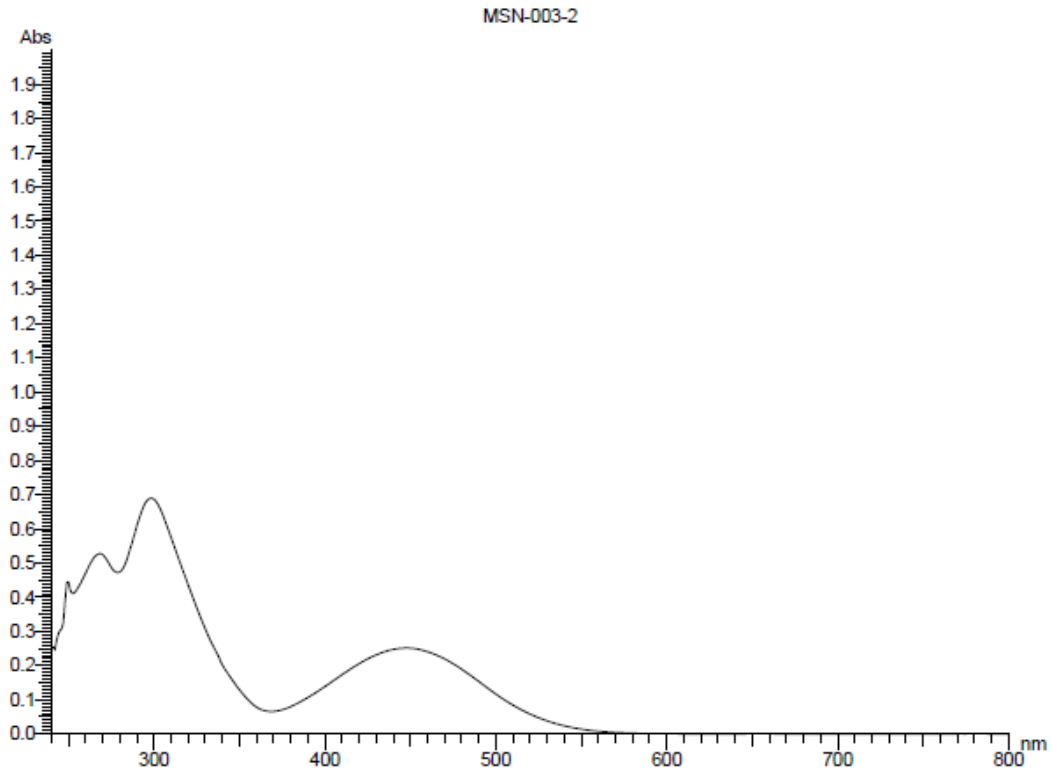

Sample: MSN-003-2
File name:
Run Date: 12:38:21, 12/02/2019
Operator: user
Comment:

Instrument
Model: U-1900 Spectrophotometer
Serial Number:
ROM Version: 3J05300 02

Instrument Parameters

Measurement Type:	Wavelength Scan
Data Mode:	Abs
Starting Wavelength:	800.0 nm
Ending Wavelength:	240.0 nm
Scan Speed:	400 nm/min
Sampling Interval:	1.0 nm
Slit Width:	4.00 nm
Lamp change mode:	Auto
Auto change wavelength:	340.0 nm
Baseline Correction:	User
Wait time:	0 s
Cycle Time:	0 min
Replicates:	1
Response:	Medium
Path Length:	10.0 mm

(Abs values are corrected to 10 mm path length)

Peak Integration

Method:	Rectangular
Sensitivity:	1
Threshold:	0.0100

Peaks

Peak #	Start (nm)	Apex (nm)	End (nm)	Height (Abs)	Area (Abs*nm)	Valley (nm)	Valley (Abs
1	800.0	447.0	368.0	0.252	26.386	368.0	0.065
2	368.0	298.0	279.0	0.690	33.590	279.0	0.472
3	279.0	268.0	240.0	0.528	17.159	240.0	0.252

G.9 UV-Vis of MSN-003 adsorbed on TiO_2 w/ CDCA

Report Date: 11:18:32, 12/04/2019

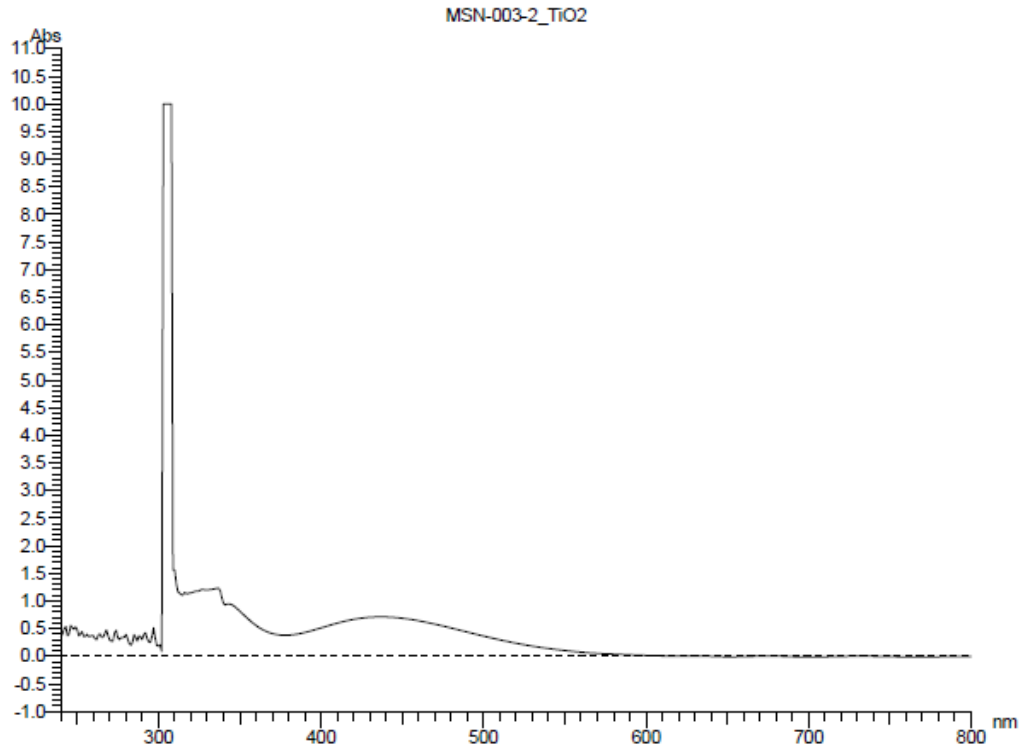

Sample: MSN-003-2_TiO2
File name:
Run Date: 11:15:45, 12/04/2019
Operator: user
Comment:

Instrument
Model: U-1900 Spectrophotometer
Serial Number:
ROM Version: 3J05300 02

Instrument Parameters

Measurement Type:	Wavelength Scan
Data Mode:	Abs
Starting Wavelength:	800.0 nm
Ending Wavelength:	240.0 nm
Scan Speed:	400 nm/min
Sampling Interval:	1.0 nm
Slit Width:	4.00 nm
Lamp change mode:	Auto
Auto change wavelength:	340.0 nm
Baseline Correction:	User
Wait time:	0 s
Cycle Time:	0 min
Replicates:	1
Response:	Medium
Path Length:	10.0 mm

(Abs values are corrected to 10 mm path length)

Peak Integration

Method:	Rectangular
Sensitivity:	1
Threshold:	0.0100

Peaks

Peak #	Start (nm)	Apex (nm)	End (nm)	Height (Abs)	Area (Abs*nm)	Valley (nm)	Valley (Abs
1	800.0	730.0	702.0	0.002	-0.524	702.0	-0.013
2	702.0	675.0	652.0	0.004	-0.185	652.0	-0.009
3	652.0	437.0	378.0	0.713	83.330	378.0	0.382
4	378.0	337.0	315.0	1.232	53.999	315.0	1.110
5	315.0	306.0	302.0	10.000	69.054	302.0	0.090
6	302.0	292.0	283.0	0.427	6.027	283.0	0.200
7	283.0	274.0	272.0	0.466	3.978	272.0	0.273

G.10 UV-Vis of MSN-003 adsorbed on TiO_2 w/o CDCA

Report Date: 11:01:46, 02/04/2020

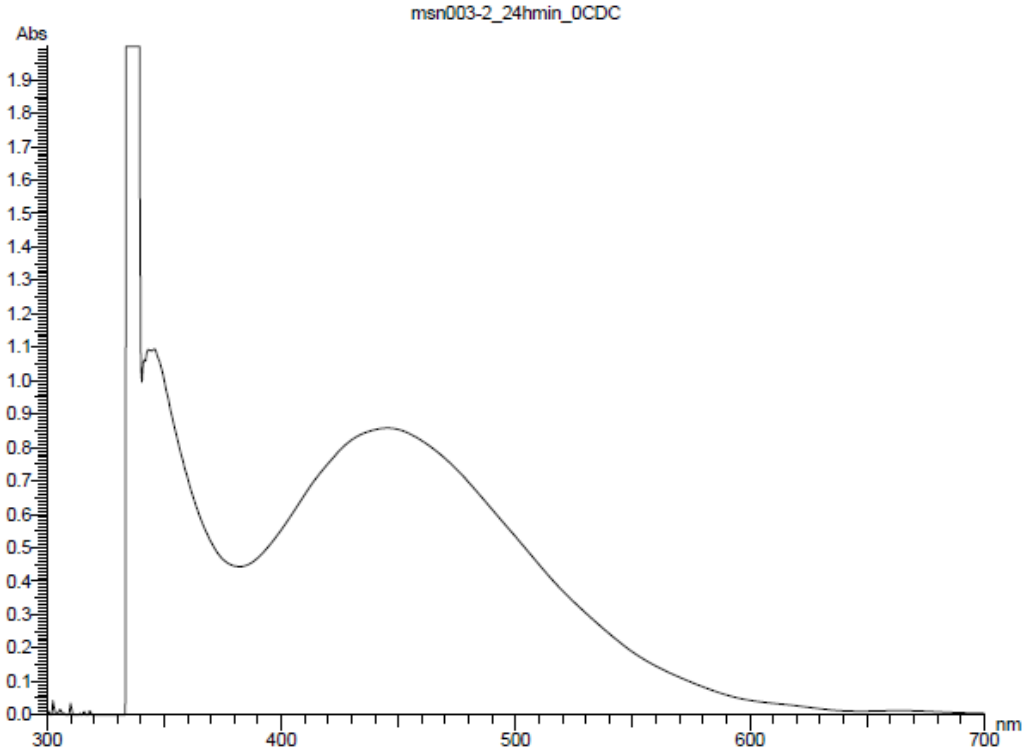

Sample: msn003-2_24hmin_0CDC
File name:
Run Date: 10:59:42, 02/04/2020
Operator: user
Comment:

Instrument
Model: U-1900 Spectrophotometer
Serial Number:
ROM Version: 3J05300 02

Instrument Parameters

Measurement Type:	Wavelength Scan
Data Mode:	Abs
Starting Wavelength:	700.0 nm
Ending Wavelength:	300.0 nm
Scan Speed:	400 nm/min
Sampling Interval:	0.5 nm
Slit Width:	4.00 nm
Lamp change mode:	Auto
Auto change wavelength:	340.0 nm
Baseline Correction:	User
Wait time:	0 s
Cycle Time:	0 min
Replicates:	1
Response:	Medium
Path Length:	10.0 mm

(Abs values are corrected to 10 mm path length)

Peak Integration

Method:	Rectangular
Sensitivity:	1
Threshold:	0.0100

Peaks

Peak #	Start (nm)	Apex (nm)	End (nm)	Height (Abs)	Area (Abs*nm)	Valley (nm)	Valley (Abs
1	700.0	445.5	382.0	0.858	106.793	382.0	0.443
2	382.0	346.0	340.5	1.094	30.571	340.5	0.996
3	340.5	338.0	332.5	10.000	56.348	332.5	-0.666
4	332.5	310.0	308.5	0.035	-1.420	308.5	-0.009

H Synthesis of 10-hexyl-7-(4-methoxyphenyl)-10*H*-phenothiazine-3-carboxylic acid (**MSN-004**)

H.1 ^{1}H NMR of **MSN-004**

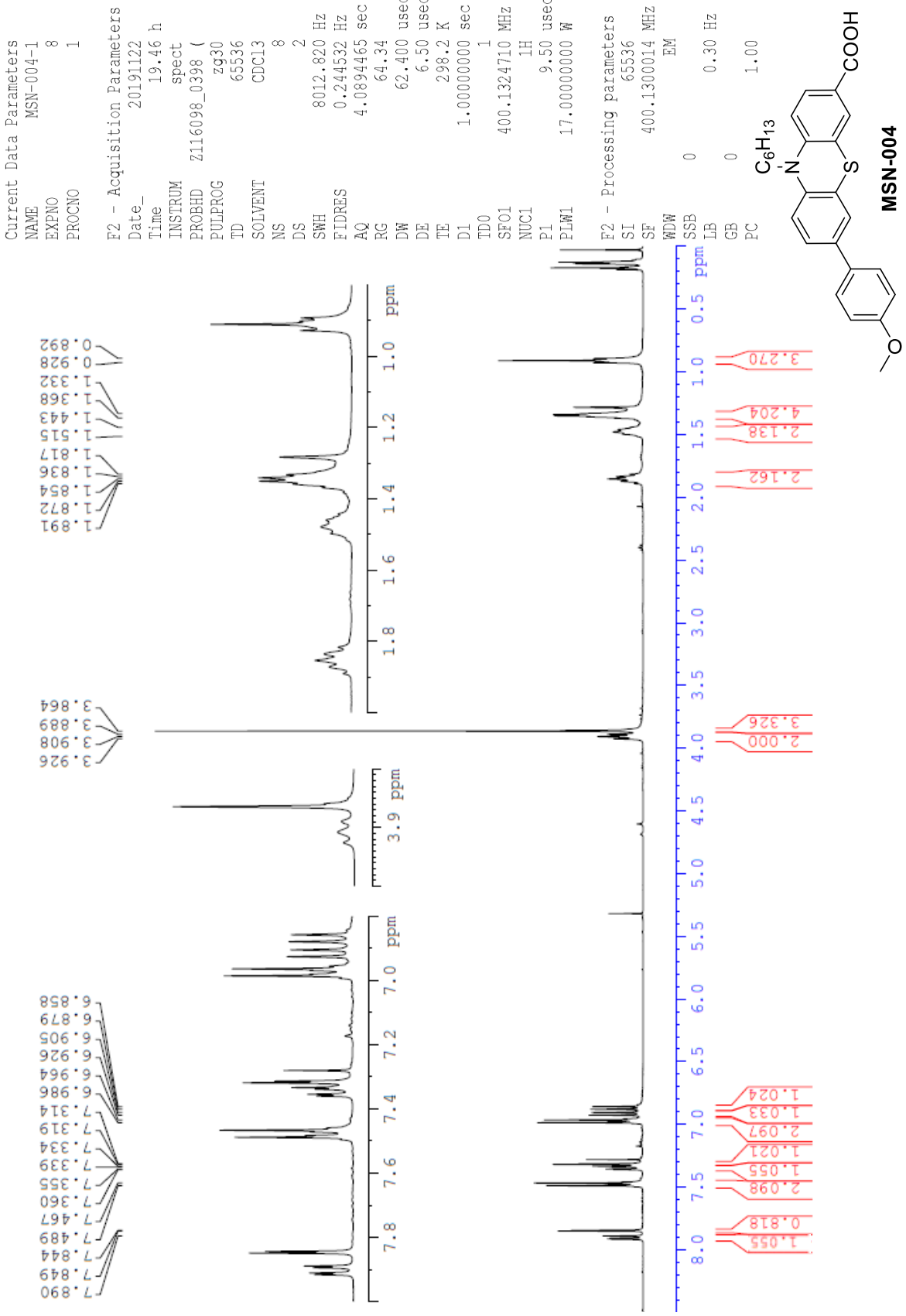

H.2 ^{13}C NMR of **MSN-004**

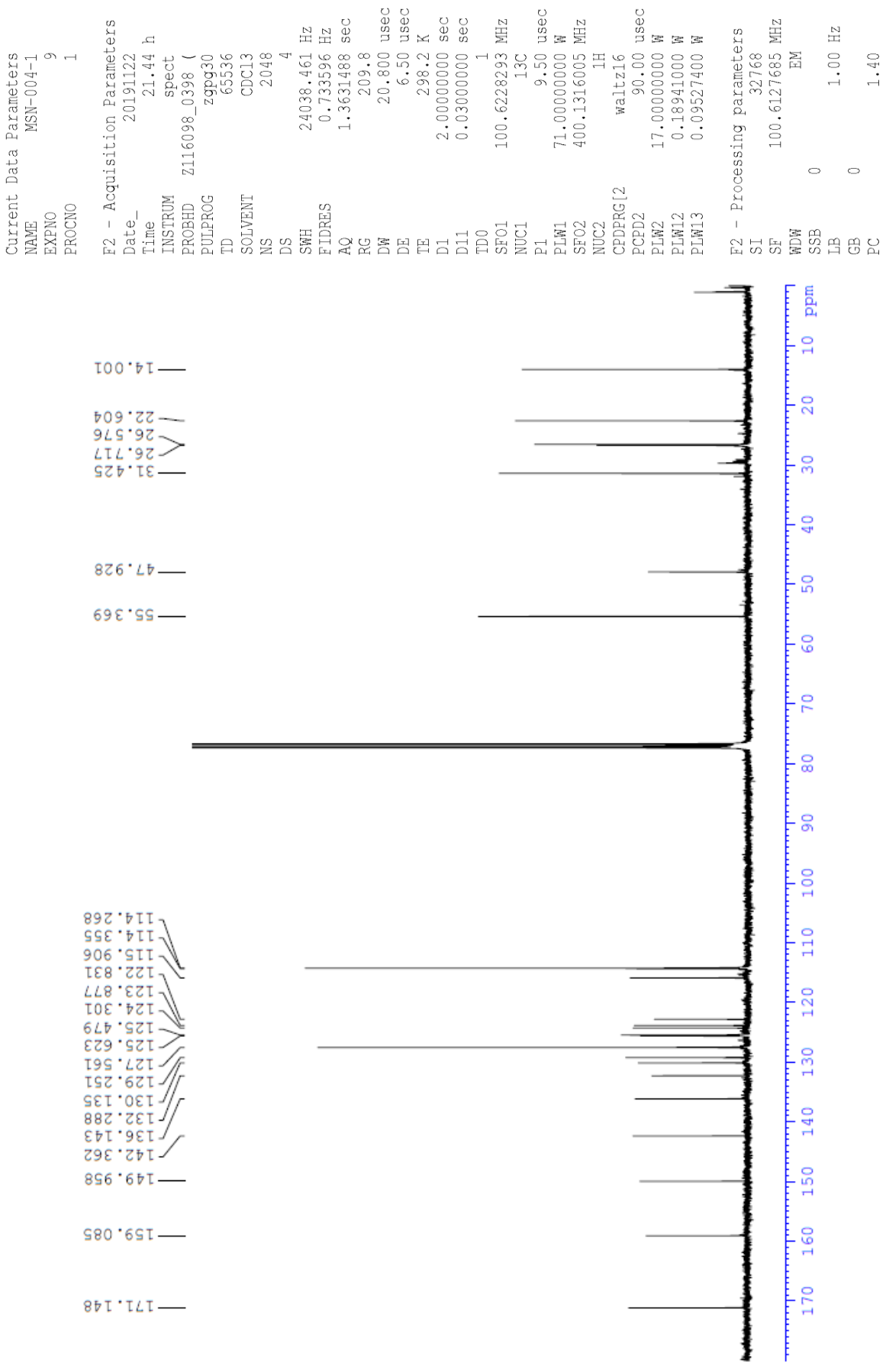

H.3 ^{1}H-^{1}H COSY of MSN-004

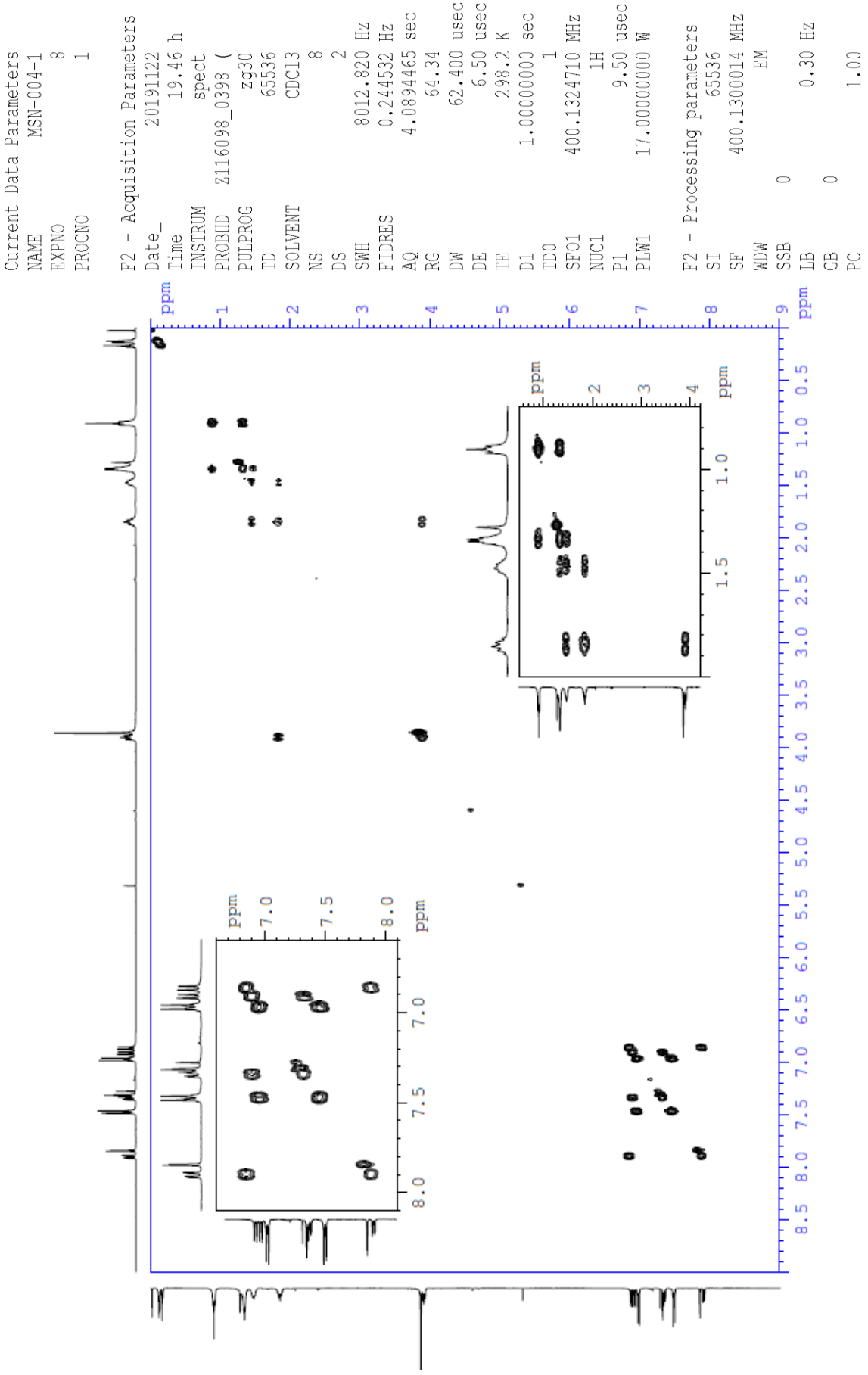

H.4 ^{1}H-^{13}C HSQC of **MSN-004**

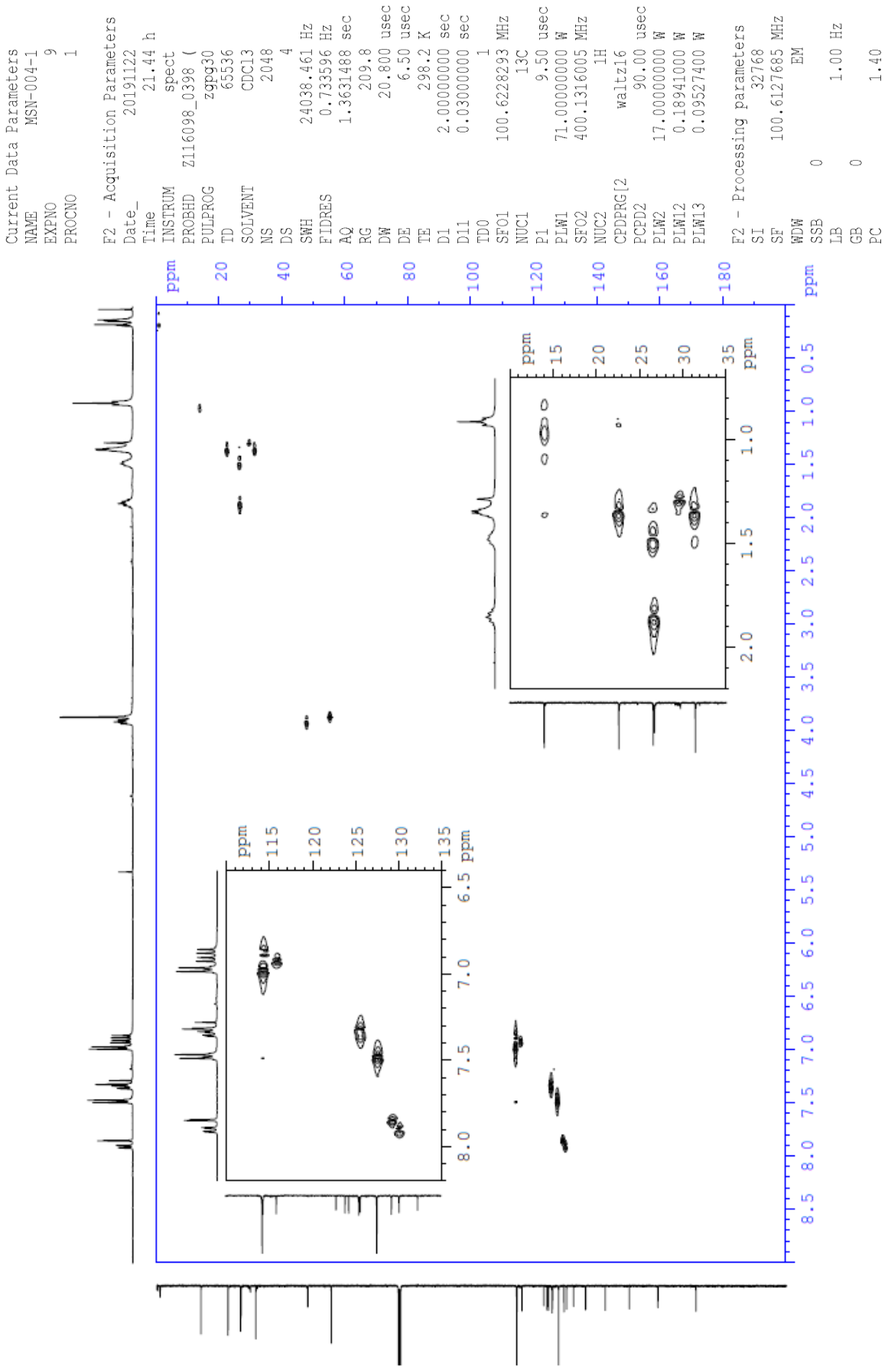

H.5 ^{1}H-^{13}C HMBC of **MSN-004**

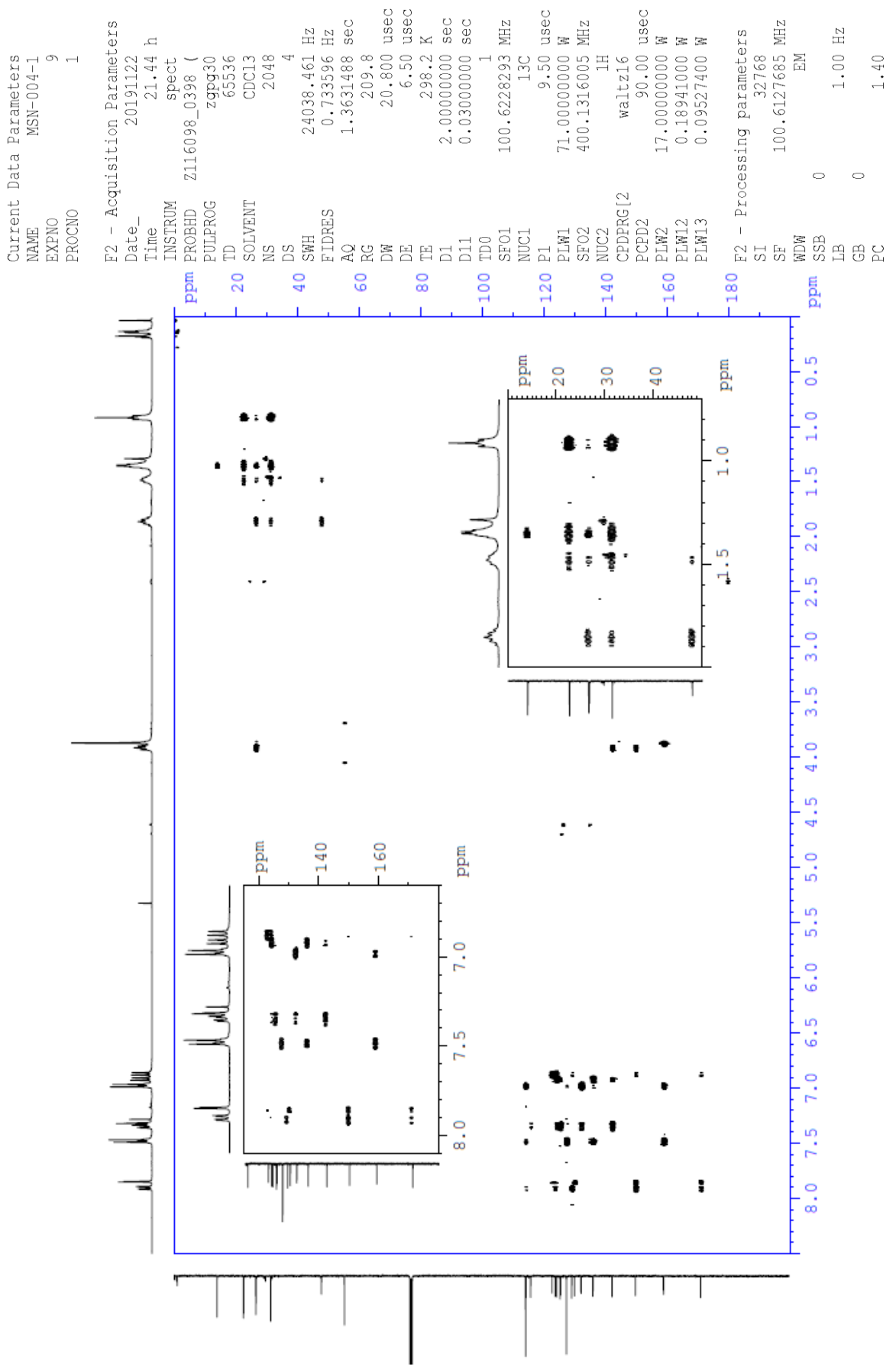

H.6 HRMS of MSN-004

Elemental Composition Report **Page 1**

Single Mass Analysis
Tolerance = 2.0 PPM / DBE: min = -5.0, max = 50.0
Element prediction: Off
Number of isotope peaks used for i-FIT = 3

Monoisotopic Mass, Even Electron Ions
4353 formula(e) evaluated with 8 results within limits (all results (up to 1000) for each mass)
Elements Used:
C: 0-100 H: 0-100 N: 0-10 O: 0-10 Na: 0-1 S: 0-3
2019_804 106 (1.186) AM2 (Ar,35000.0,0.00,0.00); Cm (103:106)
1: TOF MS ES+

2.99e+005

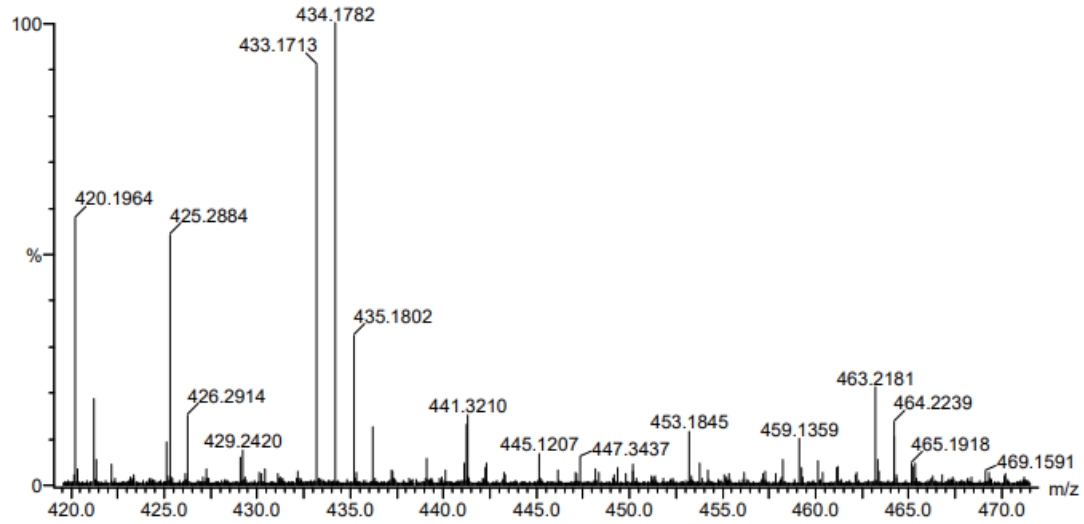

Minimum:				-5.0				
Maximum:		5.0	2.0	50.0				
Mass	Calc. Mass	mDa	PPM	DBE	i-FIT	Norm	Conf(%)	Formula
434.1782	434.1790	-0.8	-1.8	13.5	1099.4	0.053	94.83	C26 H28 N O3 S
	434.1775	0.7	1.6	5.5	1103.0	3.600	2.73	C17 H28 N3 O10
	434.1788	-0.6	-1.4	10.5	1103.6	4.225	1.46	C18 H24 N7 O6
	434.1783	-0.1	-0.2	4.5	1104.3	4.968	0.70	C18 H32 N3 O5 S2
	434.1784	-0.2	-0.5	-2.5	1106.0	6.637	0.13	C12 H33 N3 O10 Na S
	434.1782	0.0	0.0	1.5	1106.3	6.994	0.09	C10 H28 N9 O8 S
	434.1790	-0.8	-1.8	0.5	1107.1	7.765	0.04	C11 H32 N9 O3 S3
	434.1777	0.5	1.2	-4.5	1107.9	8.575	0.02	C10 H36 N5 O7 S3

H.7 FT-IR of MSN-004 (neat)

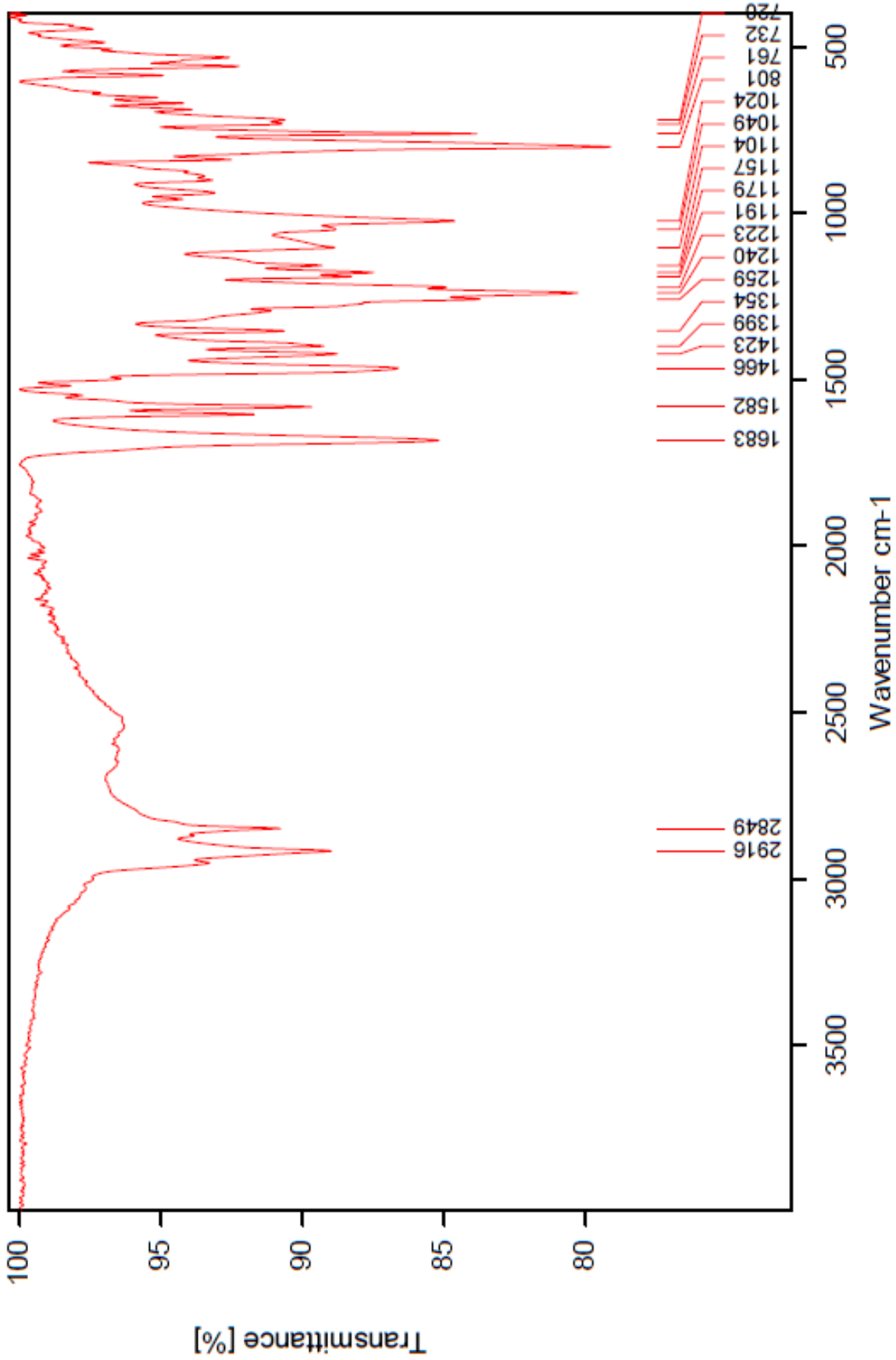

H.8 UV-Vis of MSN-004 in DCM

Report Date: 12:56:23, 12/02/2019

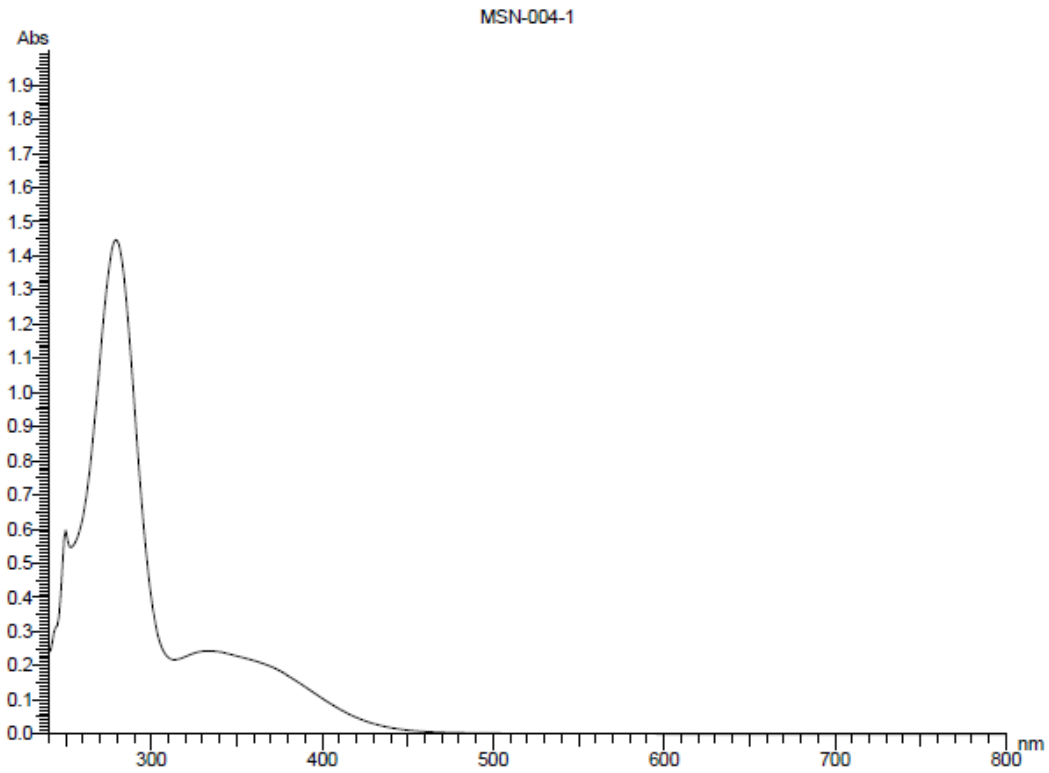

Sample: MSN-004-1
File name:
Run Date: 12:52:59, 12/02/2019
Operator: user
Comment:

Instrument
Model: U-1900 Spectrophotometer
Serial Number:
ROM Version: 3J05300 02

Instrument Parameters

Measurement Type:	Wavelength Scan
Data Mode:	Abs
Starting Wavelength:	800.0 nm
Ending Wavelength:	240.0 nm
Scan Speed:	400 nm/min
Sampling Interval:	1.0 nm
Slit Width:	4.00 nm
Lamp change mode:	Auto
Auto change wavelength:	340.0 nm
Baseline Correction:	User
Wait time:	0 s
Cycle Time:	0 min
Replicates:	1
Response:	Medium
Path Length:	10.0 mm

(Abs values are corrected to 10 mm path length)

Peak Integration

Method:	Rectangular
Sensitivity:	1
Threshold:	0.0100

Peaks

Peak #	Start (nm)	Apex (nm)	End (nm)	Height (Abs)	Area (Abs*nm)	Valley (nm)	Valley (Abs
1	800.0	333.0	314.0	0.243	20.049	314.0	0.217
2	314.0	279.0	240.0	1.447	53.917	240.0	0.251

H.9 UV-Vis of MSN-004 adsorbed on TiO_2 w/ CDCA

Report Date: 11:10:15, 12/04/2019

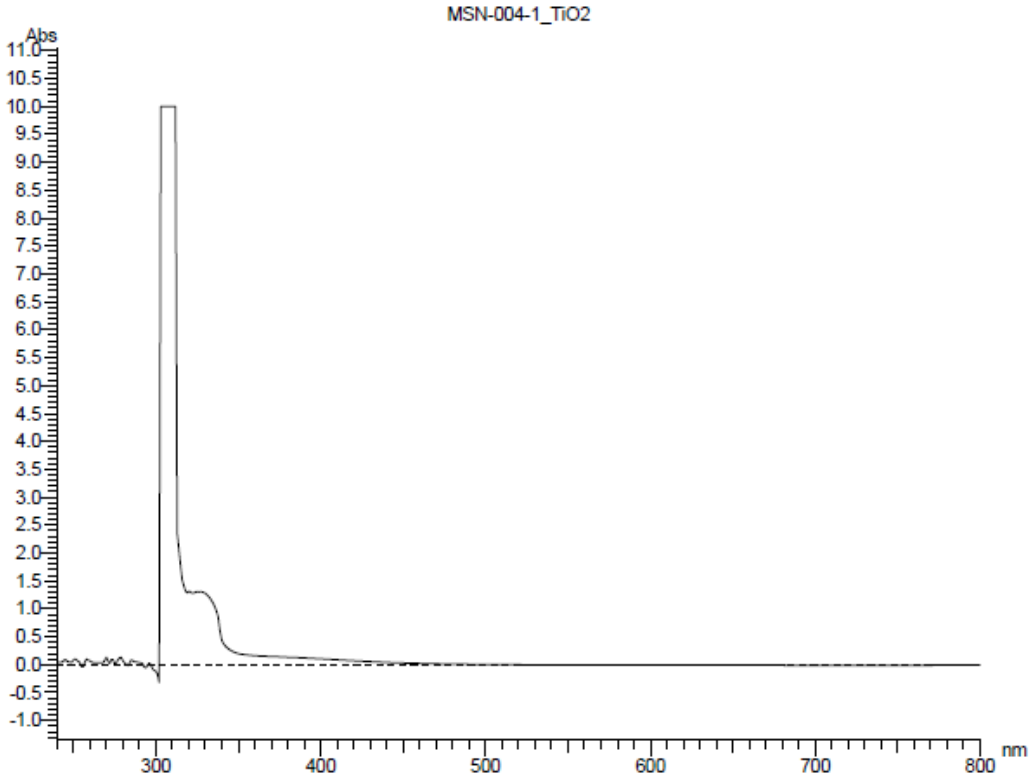

Sample: MSN-004-1_TiO2
File name:
Run Date: 11:07:23, 12/04/2019
Operator: user
Comment:

Instrument
Model: U-1900 Spectrophotometer
Serial Number:
ROM Version: 3J05300 02

Instrument Parameters

Measurement Type:	Wavelength Scan
Data Mode:	Abs
Starting Wavelength:	800.0 nm
Ending Wavelength:	240.0 nm
Scan Speed:	400 nm/min
Sampling Interval:	1.0 nm
Slit Width:	4.00 nm
Lamp change mode:	Auto
Auto change wavelength:	340.0 nm
Baseline Correction:	User
Wait time:	0 s
Cycle Time:	0 min
Replicates:	1
Response:	Medium
Path Length:	10.0 mm

(Abs values are corrected to 10 mm path length)

Peak Integration

Method:	Rectangular
Sensitivity:	1
Threshold:	0.0100

Peaks

Peak #	Start (nm)	Apex (nm)	End (nm)	Height (Abs)	Area (Abs*nm)	Valley (nm)	Valley (Abs
1	800.0	310.0	302.0	10.000	146.116	302.0	-0.318
2	302.0	285.0	283.0	0.081	-0.473	283.0	-0.014
3	283.0	279.0	265.0	0.130	1.073	265.0	0.032
4	265.0	258.0	256.0	0.098	0.434	256.0	-0.038
5	256.0	251.0	240.0	0.102	0.766	240.0	0.017

H.10 UV-Vis of MSN-004 adsorbed on TiO_2 w/o CDCA

Report Date: 11:39:26, 01/31/2020

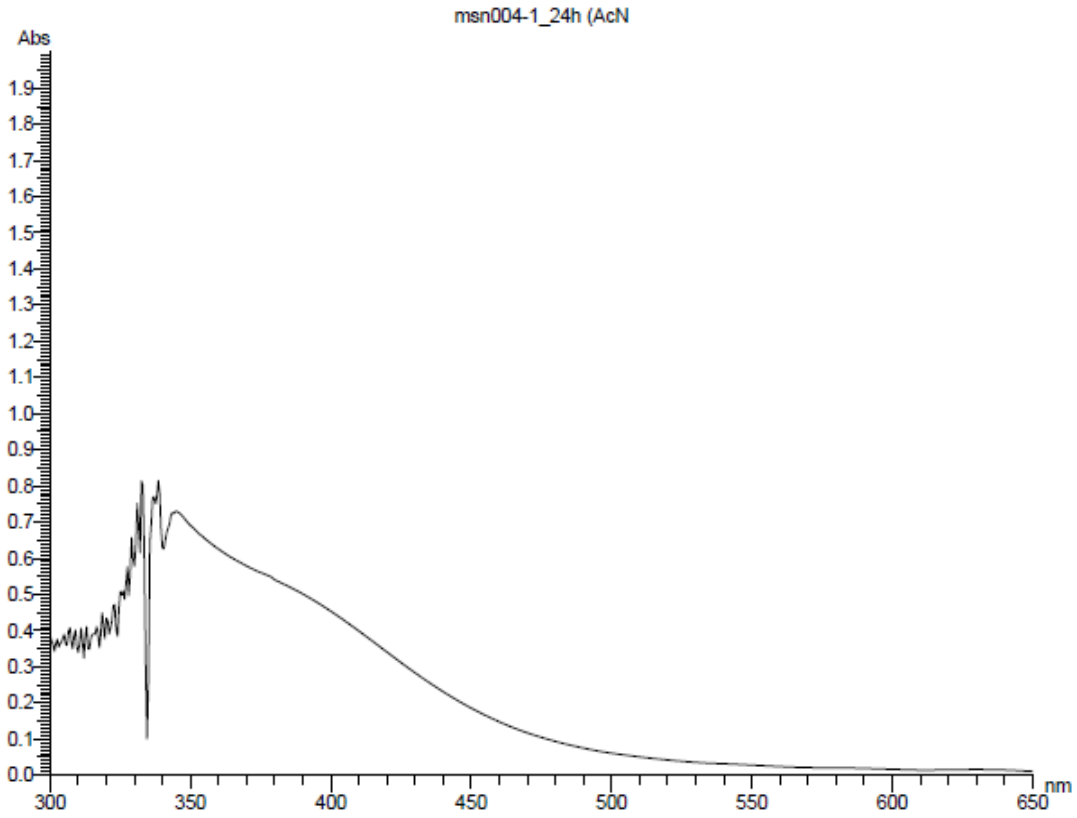

Sample: msn004-1_24h (AcN
File name:
Run Date: 11:37:22, 01/31/2020
Operator: user
Comment:

Instrument
Model: U-1900 Spectrophotometer
Serial Number:
ROM Version: 3J05300 02

Instrument Parameters

Measurement Type:	Wavelength Scan
Data Mode:	Abs
Starting Wavelength:	650.0 nm
Ending Wavelength:	300.0 nm
Scan Speed:	400 nm/min
Sampling Interval:	0.5 nm
Slit Width:	4.00 nm
Lamp change mode:	Auto
Auto change wavelength:	340.0 nm
Baseline Correction:	User
Wait time:	0 s
Cycle Time:	0 min
Replicates:	1
Response:	Medium
Path Length:	10.0 mm

(Abs values are corrected to 10 mm path length)

Peak Integration

Method:	Rectangular
Sensitivity:	1
Threshold:	0.0100

Peaks

Peak #	Start (nm)	Apex (nm)	End (nm)	Height (Abs)	Area (Abs*nm)	Valley (nm)	Valley (Abs
1	650.0	345.0	340.5	0.730	60.135	340.5	0.626
2	340.5	338.5	334.5	0.814	4.146	334.5	0.101
3	334.5	332.5	310.0	0.813	11.624	310.0	0.340
4	310.0	307.0	300.0	0.407	3.700	300.0	0.385

I 10-hexyl-3-(4-methoxyphenyl)-7-(perfluorophenyl)-10*H*-phenothiazine (**MSN-005**)

I.1 ^{1}H NMR of **MSN-005**

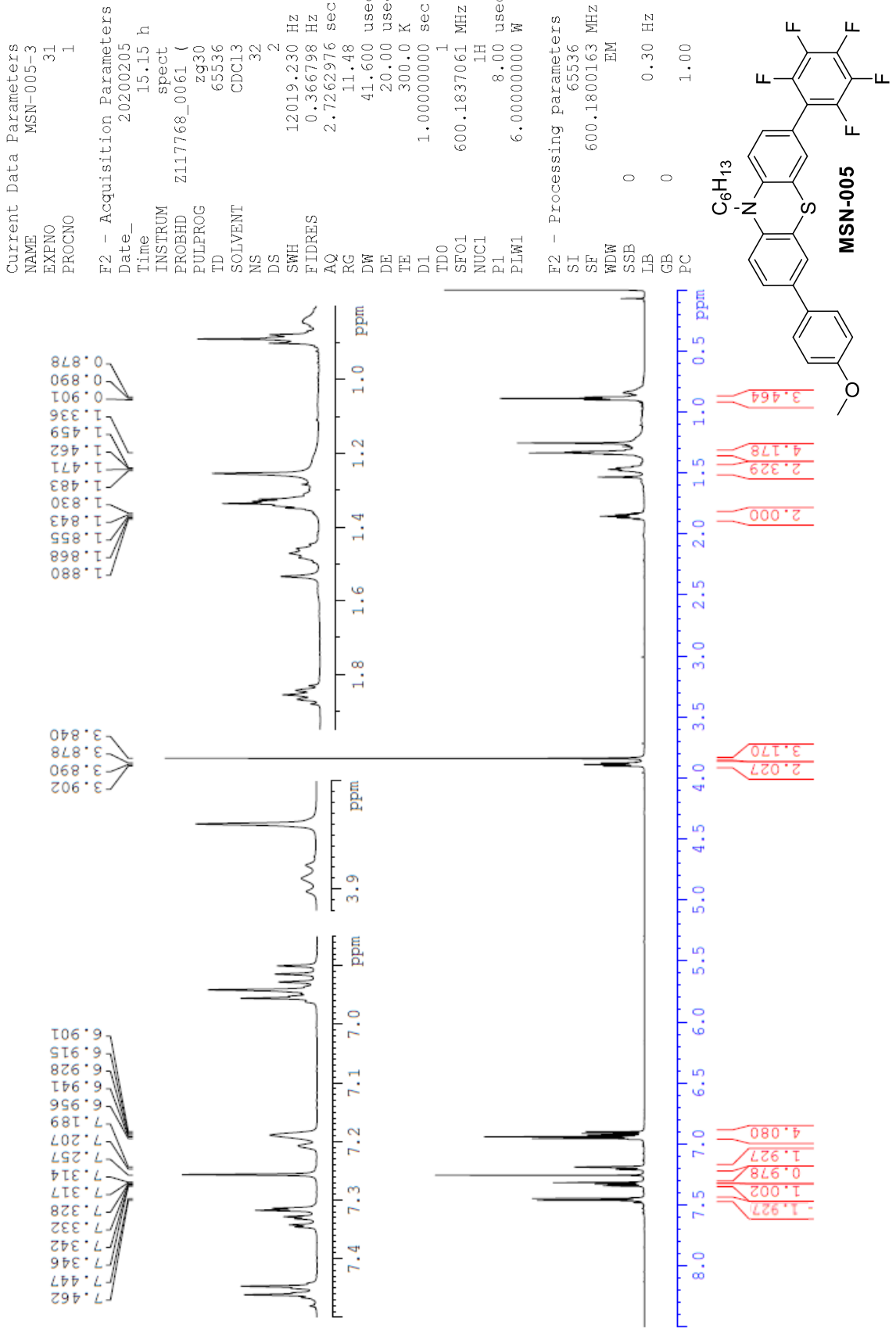

I.2 ^{13}C NMR of **MSN-005**

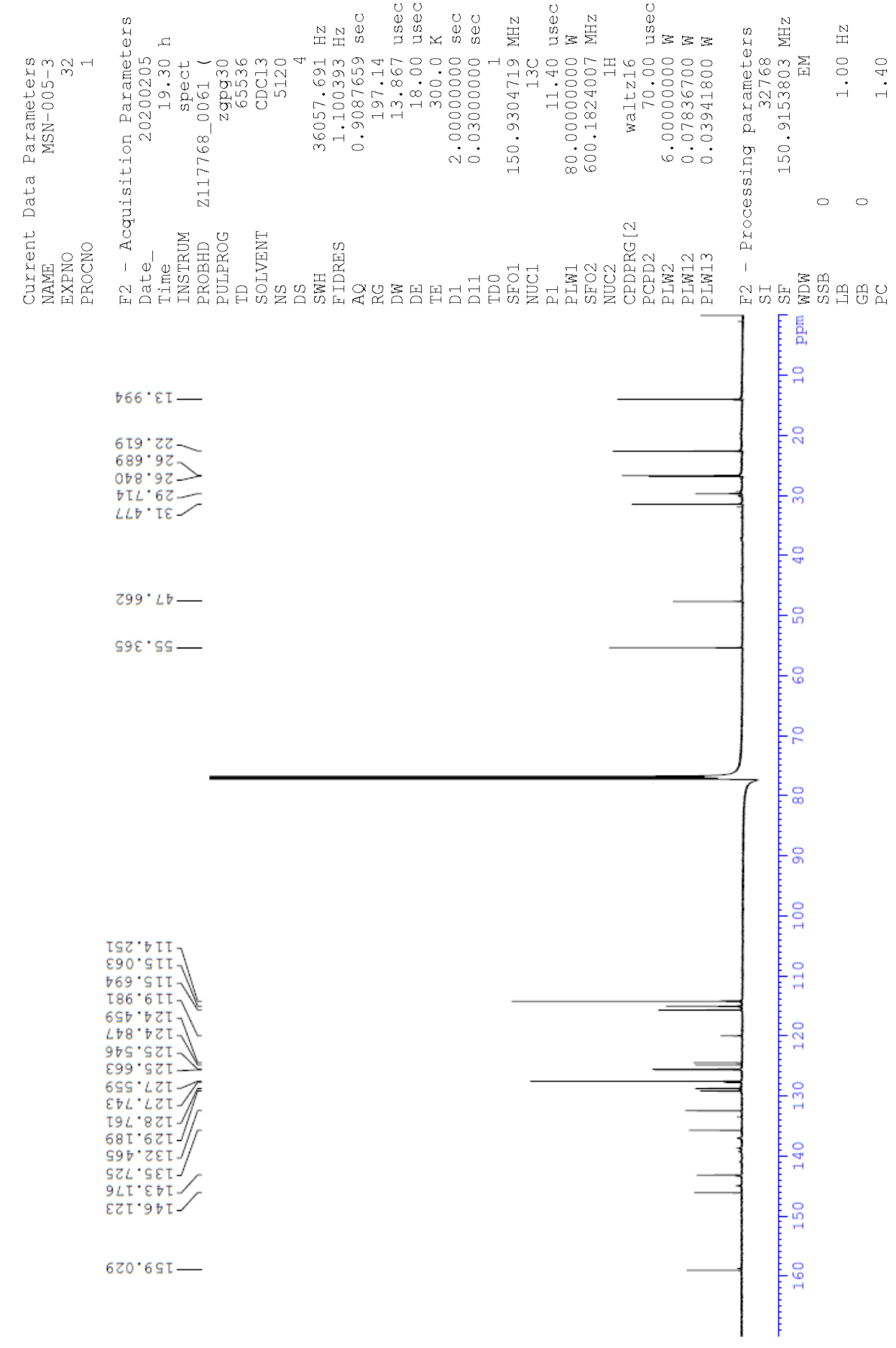

I.3 ^{19}F NMR of **MSN-005**

```
Current Data Parameters
NAME          MSN-005-3
EXPNO                 5
PROCNO                1

F2 - Acquisition Parameters
Date_          20191128
Time              13.19 h
INSTRUM             spect
PROBHD   Z116098_0398 (
PULPROG           zgflqn
TD                131072
SOLVENT            CDCl3
NS                    64
DS                     4
SWH           89285.711 Hz
FIDRES         1.362392 Hz
AQ             0.73400032 sec
RG                 209.8
DW                 5.600 usec
DE                 6.50 usec
TE                 300.0 K
D1             1.00000000 sec
TD0                    1
SFO1         376.4607164 MHz
NUC1                 19F
P1                17.50 usec
PLW1          19.00000000 W

F2 - Processing parameters
SI                 65536
SF           376.4983662 MHz
WDW                   EM
SSB                    0
LB                  0.30 Hz
GB                     0
PC                  1.00
```

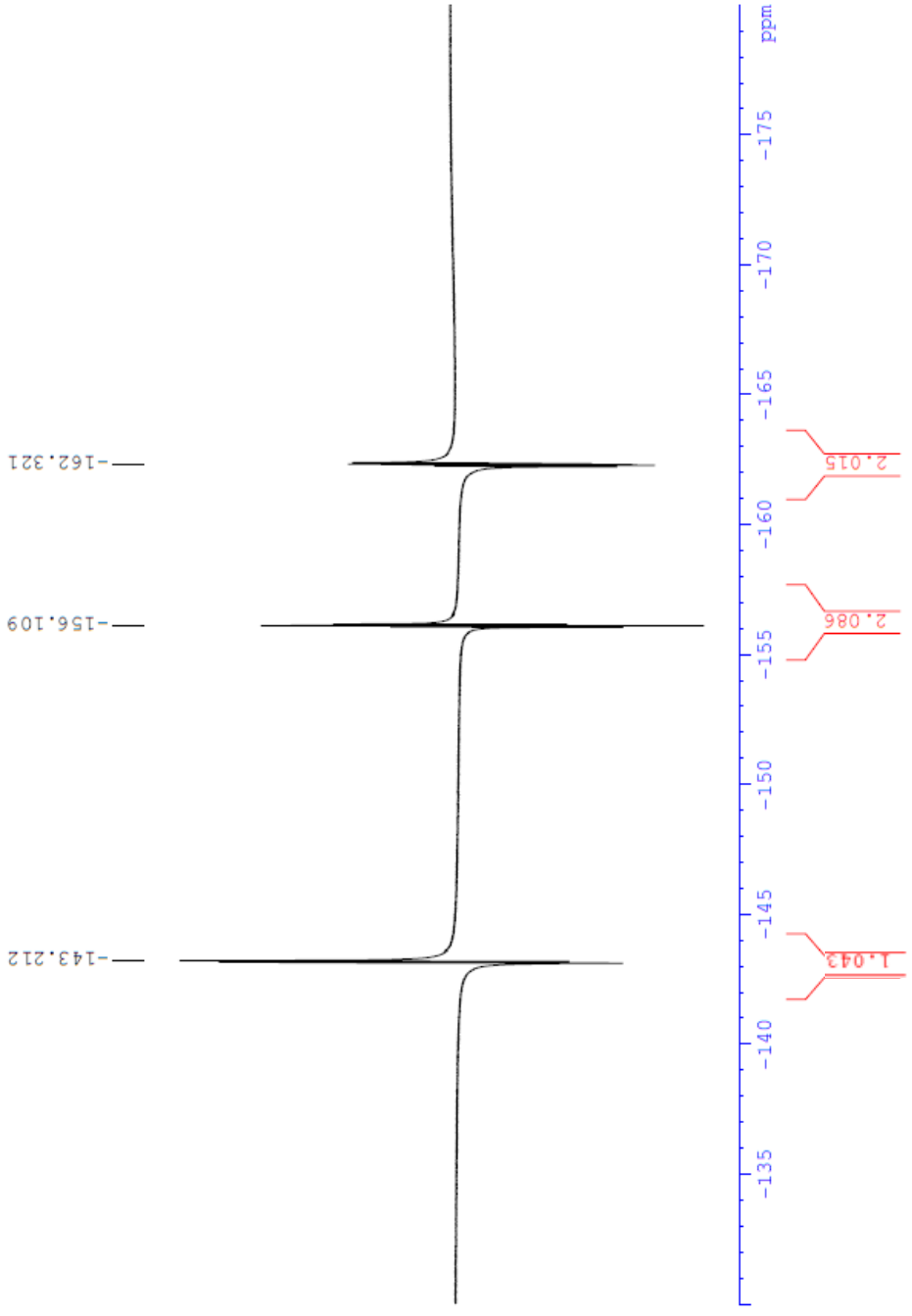

I.4 ^{1}H-^{1}H COSY of **MSN-005**

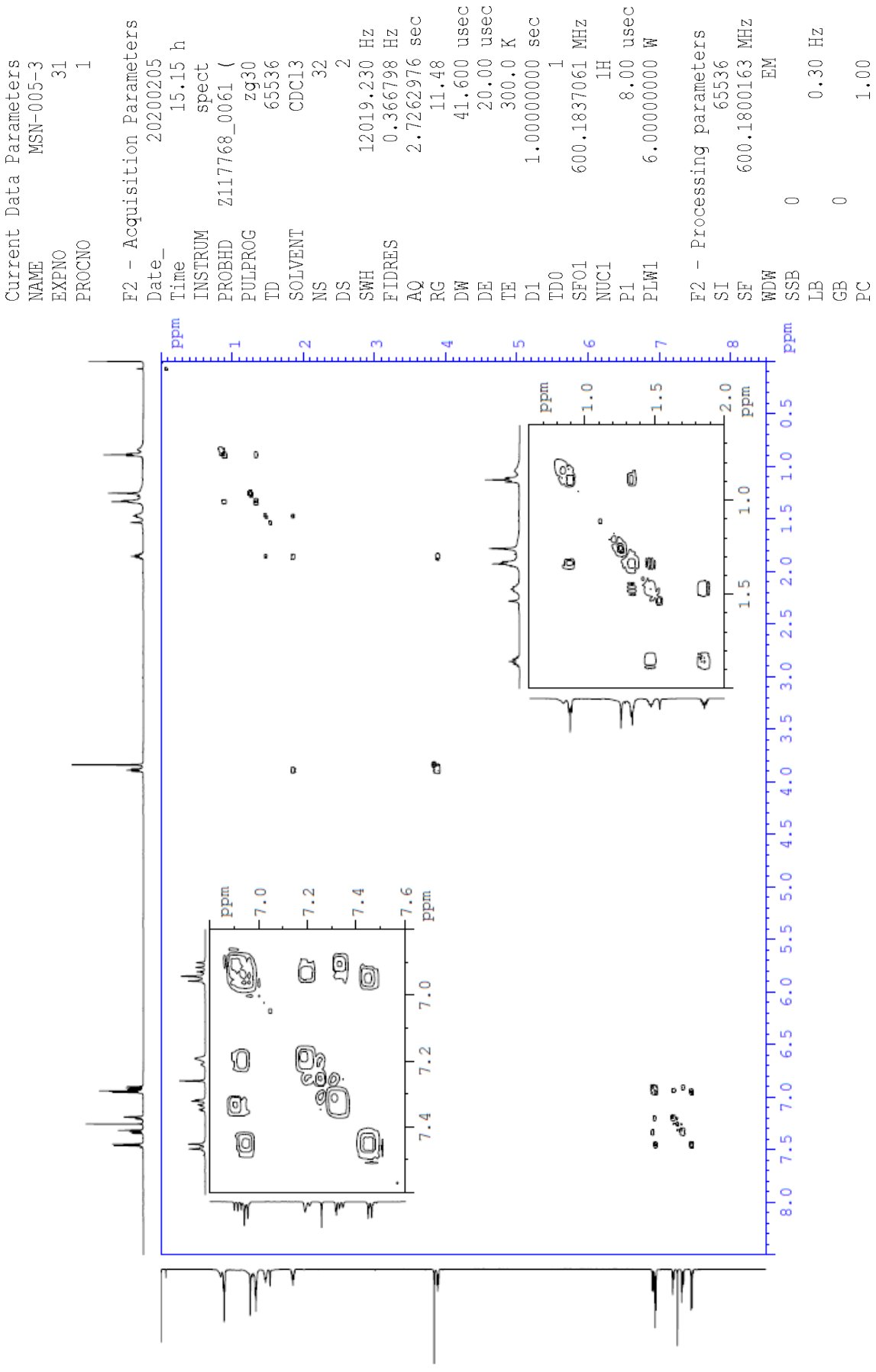

I.5 ^{1}H-^{13}C HSQC of **MSN-005**

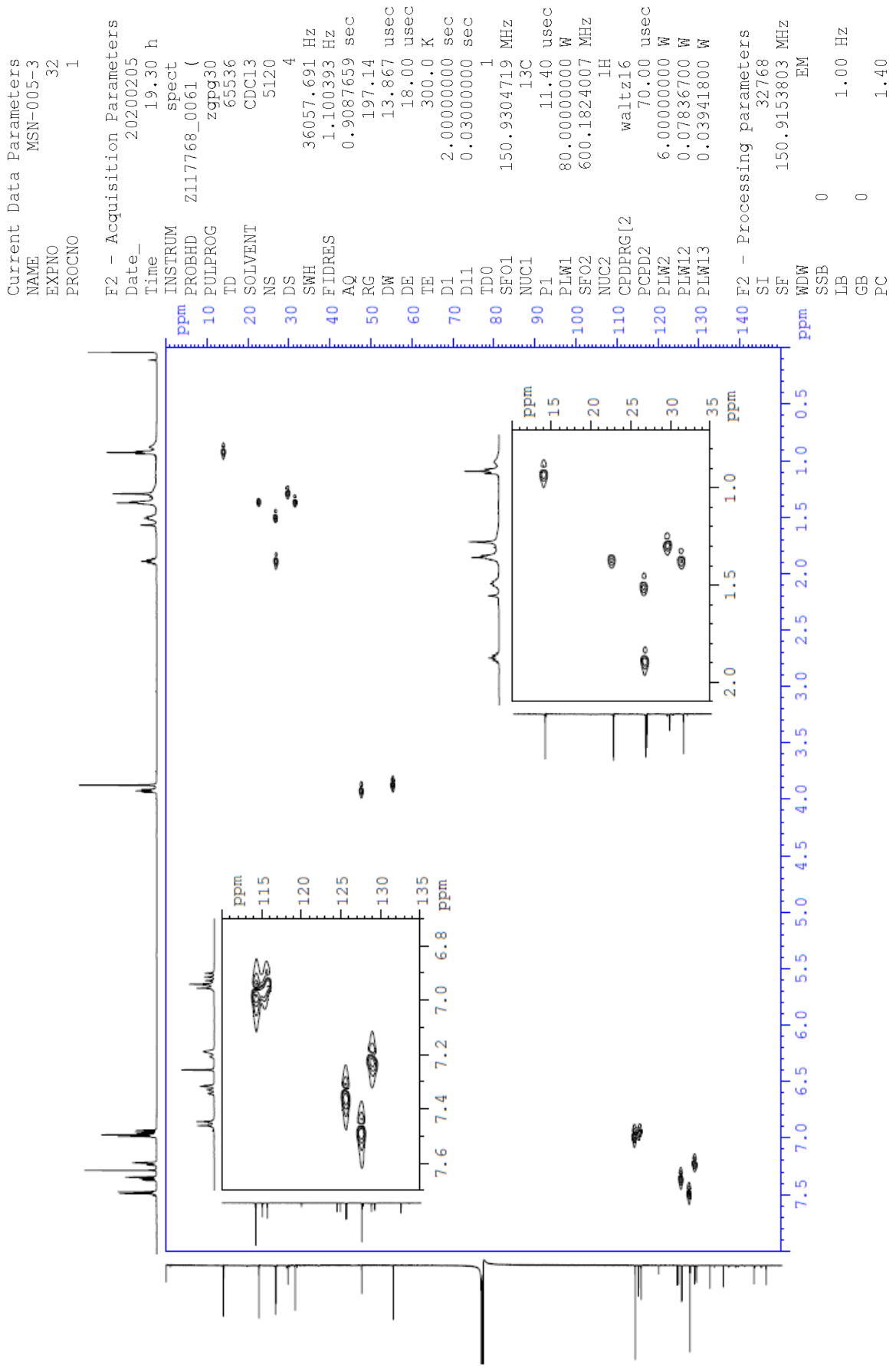

I.6 ^{1}H-^{13}C HMBC of **MSN-005**

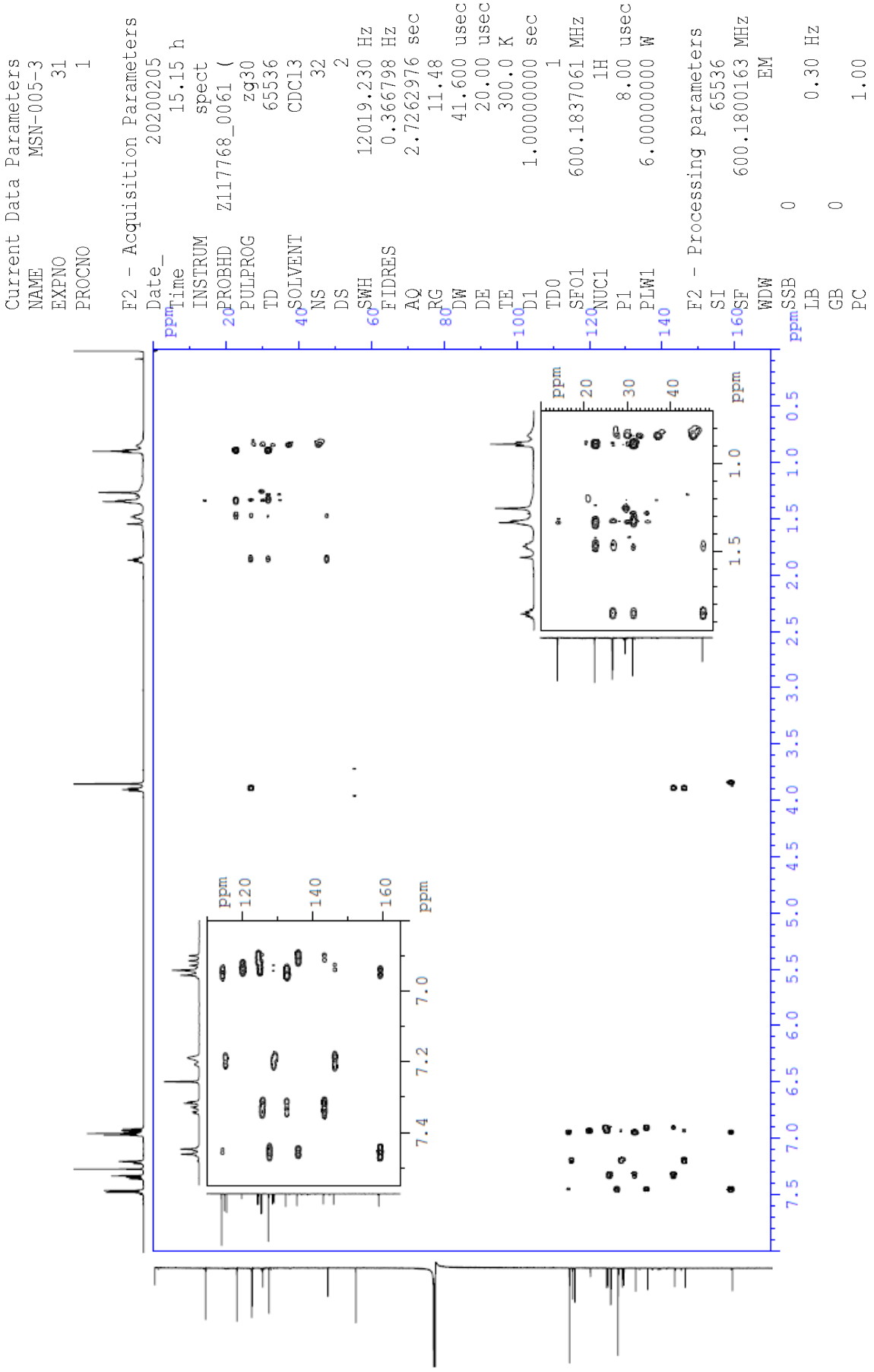

I.7 HRMS of MSN-005

Elemental Composition Report **Page 1**

Single Mass Analysis
Tolerance = 2.0 PPM / DBE: min = -5.0, max = 50.0
Element prediction: Off
Number of isotope peaks used for i-FIT = 3

Monoisotopic Mass, Even Electron Ions
2370 formula(e) evaluated with 4 results within limits (all results (up to 1000) for each mass)
Elements Used:
C: 0-100 H: 0-100 N: 0-2 O: 0-5 F: 0-6 S: 0-2
2019_816 34 (0.393) AM2 (Ar,35000.0,0.00,0.00); Cm (29:34)
1: TOF MS ES+

1.56e+006

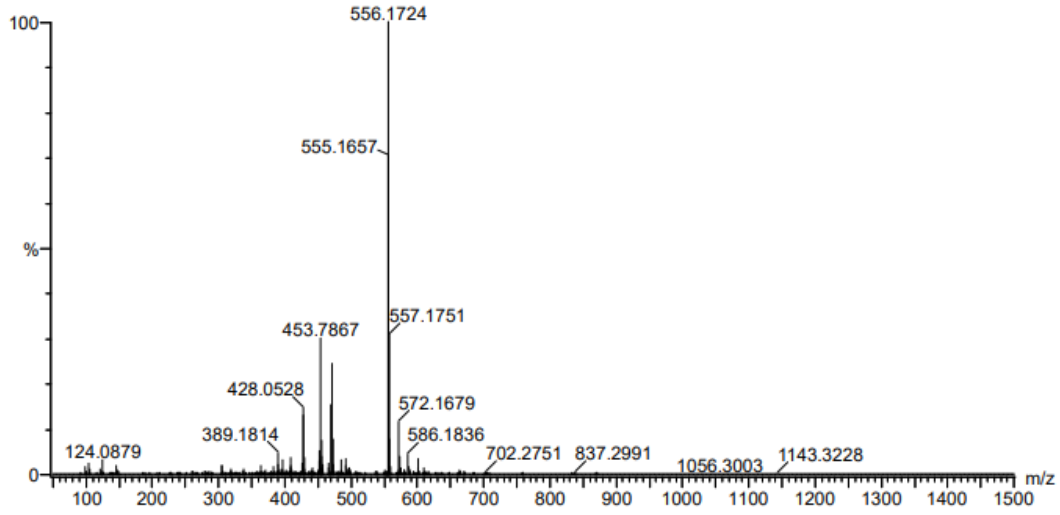

Minimum:				-5.0				
Maximum:		5.0	2.0	50.0				
Mass	Calc. Mass	mDa	PPM	DBE	i-FIT	Norm	Conf(%)	Formula
556.1724	556.1722	0.2	0.4	20.5	818.4	0.626	53.48	C34 H26 N F4 S
	556.1734	-1.0	-1.8	16.5	818.6	0.775	46.09	C31 H27 N O F5 S
	556.1735	-1.1	-2.0	27.5	823.7	5.884	0.28	C39 H26 N O S
	556.1724	0.0	0.0	24.5	824.3	6.472	0.15	C36 H24 N O3 F2

I.8 FT-IR of MSN-005 (neat)

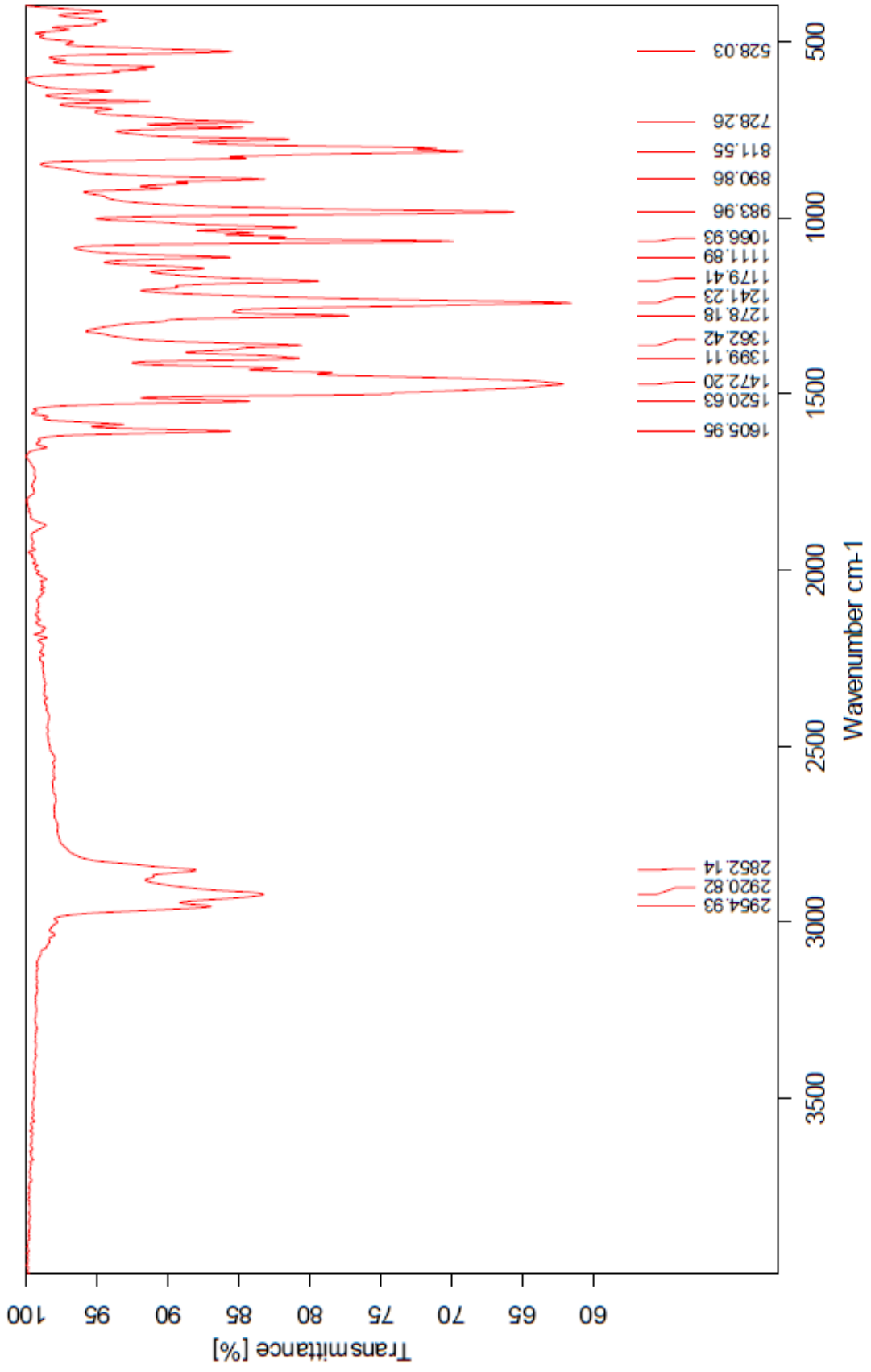

I.9 UV-Vis of **MSN-005** in DCM

Report Date: 10:58:48, 04/27/2020

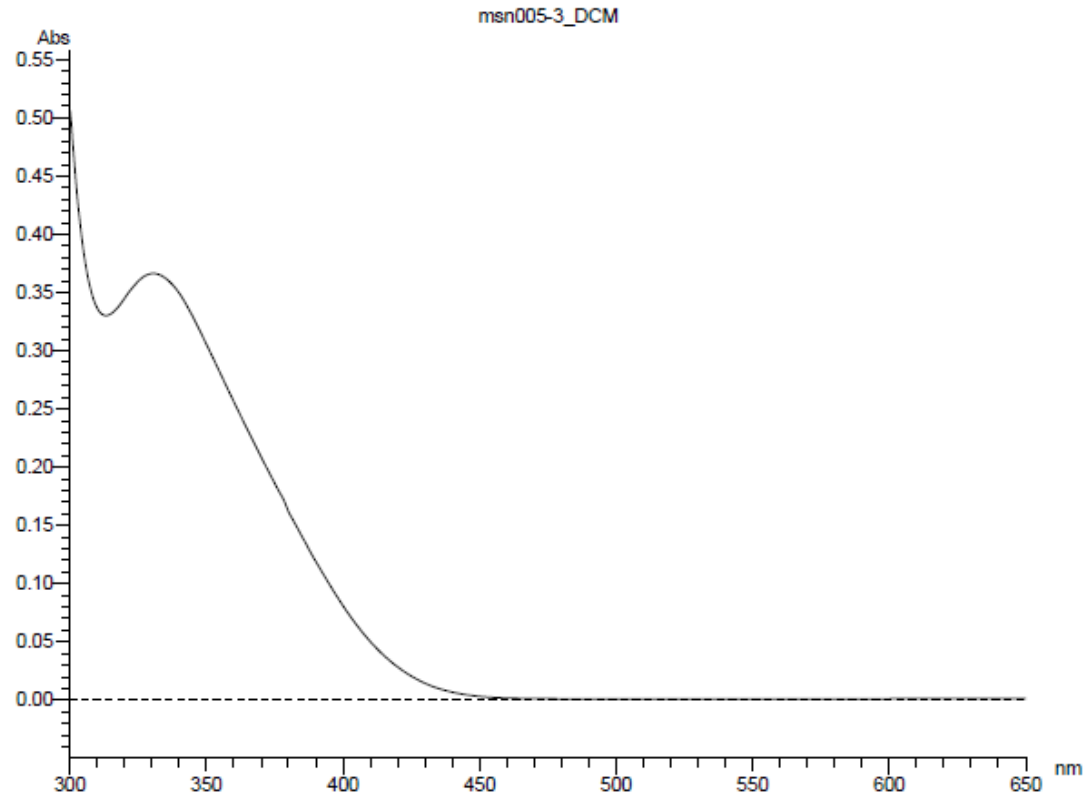

Sample: msn005-3_DCM
File name:
Run Date: 10:56:43, 04/27/2020
Operator: user
Comment:

Instrument
Model: U-1900 Spectrophotometer
Serial Number:
ROM Version: 3J05300 02

Instrument Parameters

Measurement Type:	Wavelength Scan
Data Mode:	Abs
Starting Wavelength:	650.0 nm
Ending Wavelength:	300.0 nm
Scan Speed:	400 nm/min
Sampling Interval:	0.5 nm
Slit Width:	4.00 nm
Lamp change mode:	Auto
Auto change wavelength:	340.0 nm
Baseline Correction:	User
Wait time:	0 s
Cycle Time:	0 min
Replicates:	1
Response:	Medium
Path Length:	10.0 mm

(Abs values are corrected to 10 mm path length)

Peak Integration

Method:	Rectangular
Sensitivity:	1
Threshold:	0.0100

Peaks

Peak #	Start (nm)	Apex (nm)	End (nm)	Height (Abs)	Area (Abs*nm)	Valley (nm)	Valley (Abs
1	650.0	330.5	313.0	0.366	23.914	313.0	0.330

J 10-hexyl-3-(4-methoxyphenyl)-7-(pyridine-4-yl)-10*H*-phenothiazine (MSN-006)

J.1 ^{1}H NMR of MSN-006

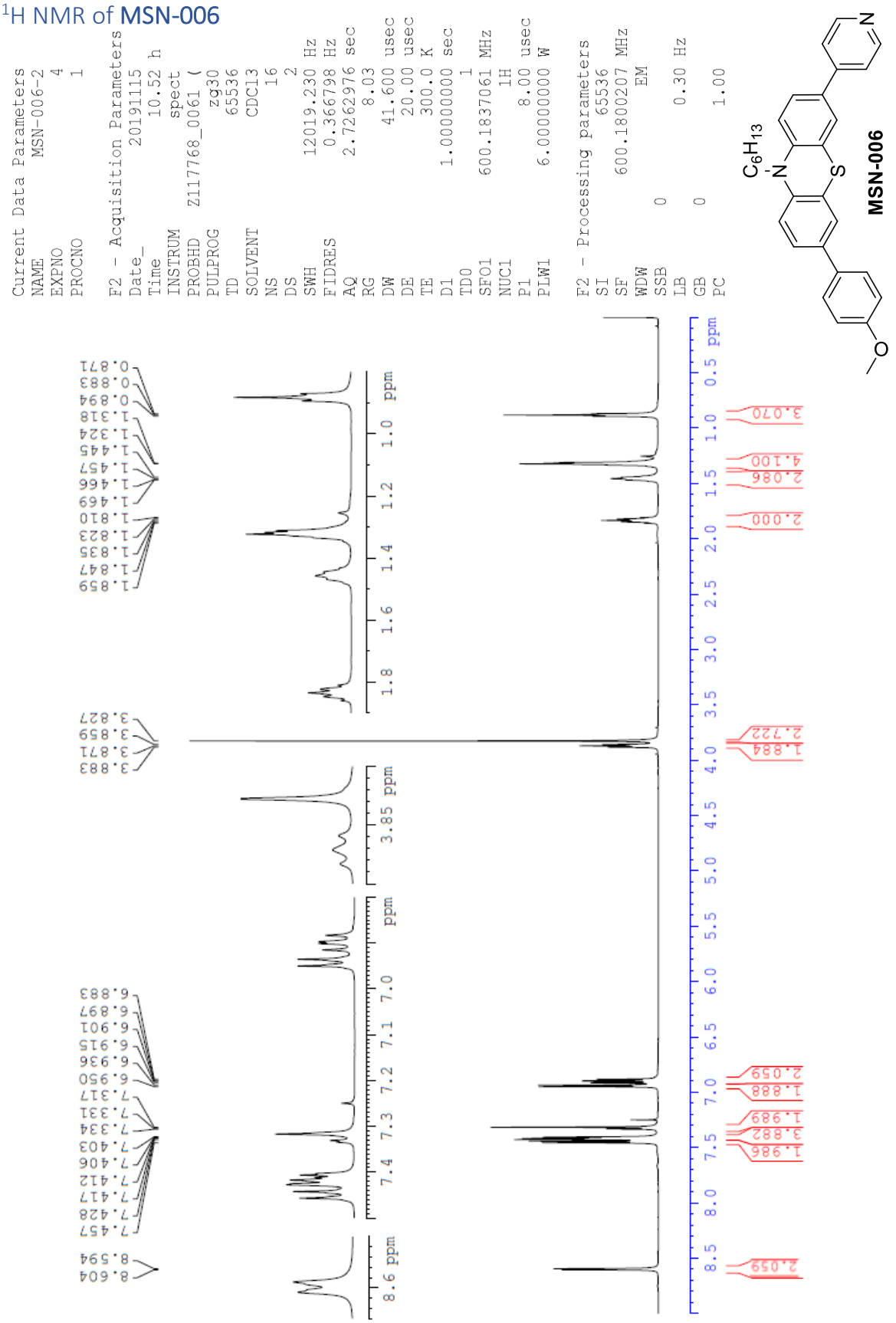

J.2 ^{13}C NMR of **MSN-006**

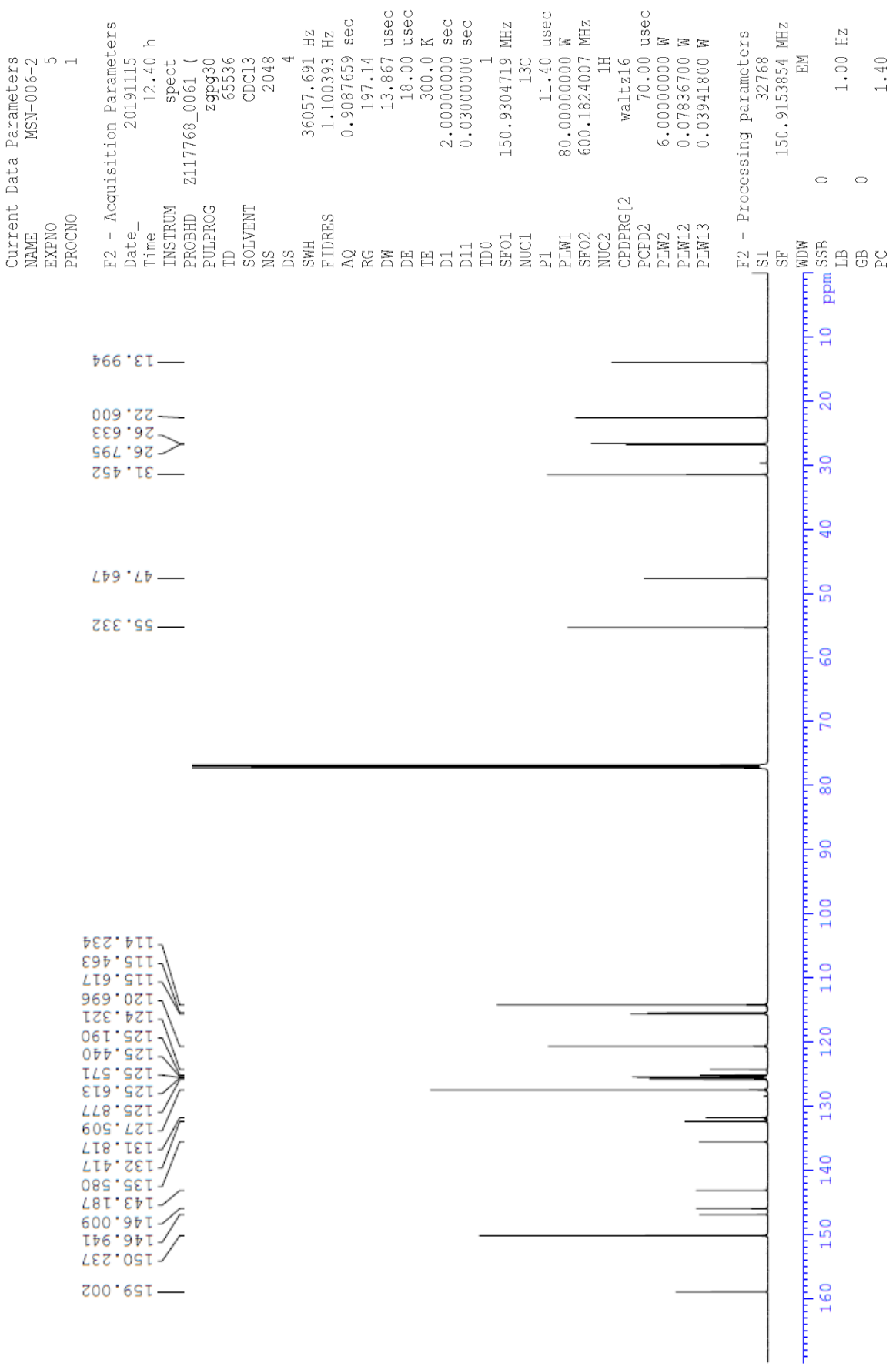

J.3 ^{1}H-^{1}H COSY of MSN-006

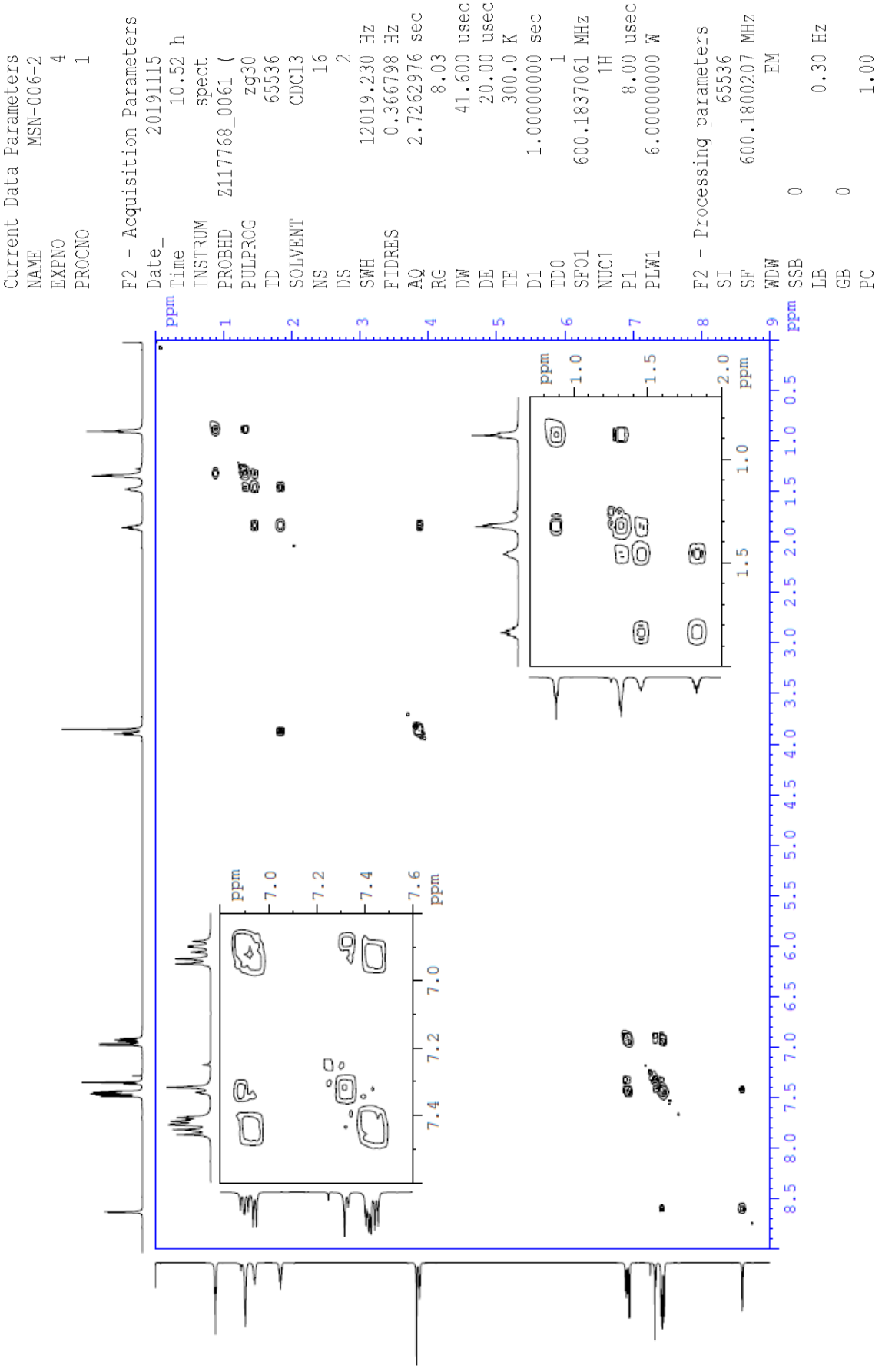

J.4 ^{1}H-^{13}C HSQC of MSN-006

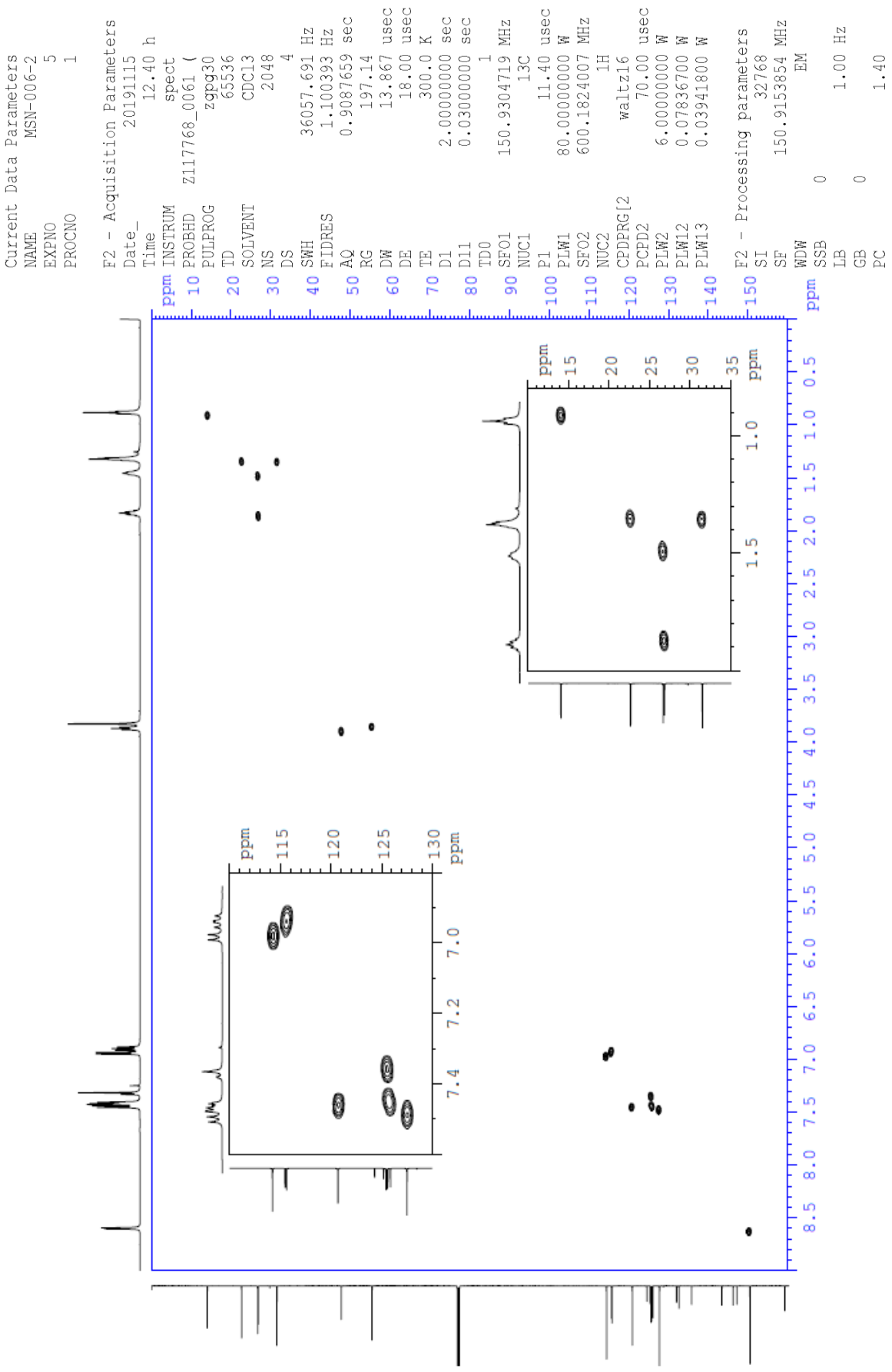

J.5 ^{1}H-^{13}C HMBC of MSN-006

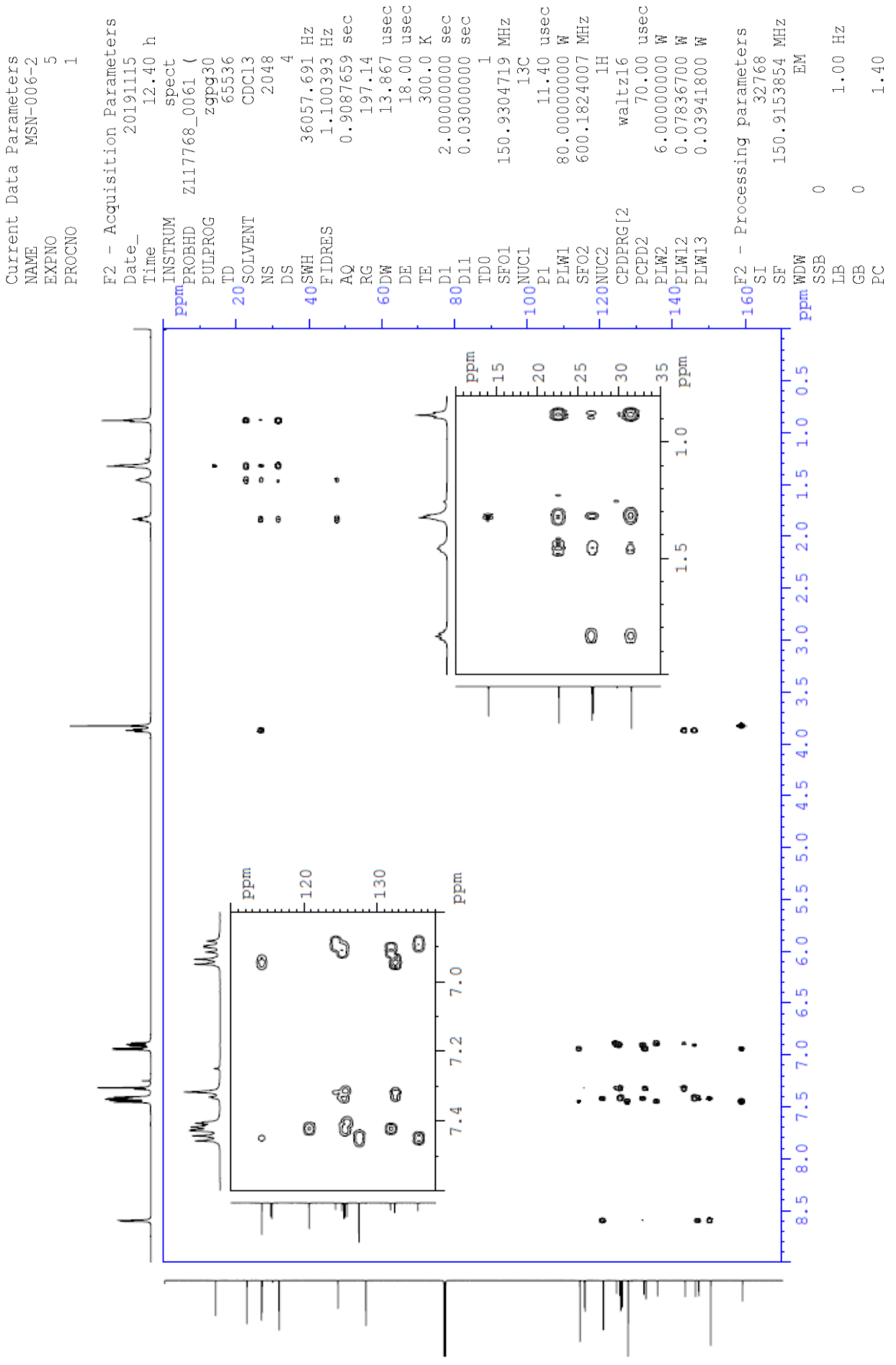

J.6 HRMS of MSN-006

Elemental Composition Report **Page 1**

Single Mass Analysis
Tolerance = 2.0 PPM / DBE: min = -5.0, max = 50.0
Element prediction: Off
Number of isotope peaks used for i-FIT = 3

Monoisotopic Mass, Even Electron Ions
3432 formula(e) evaluated with 4 results within limits (all results (up to 1000) for each mass)
Elements Used:
C: 0-100 H: 0-100 N: 0-10 O: 0-10 S: 0-5
2019_794 31 (0.360) AM2 (Ar,35000.0,0.00,0.00); Cm (29:31)
1: TOF MS ES+

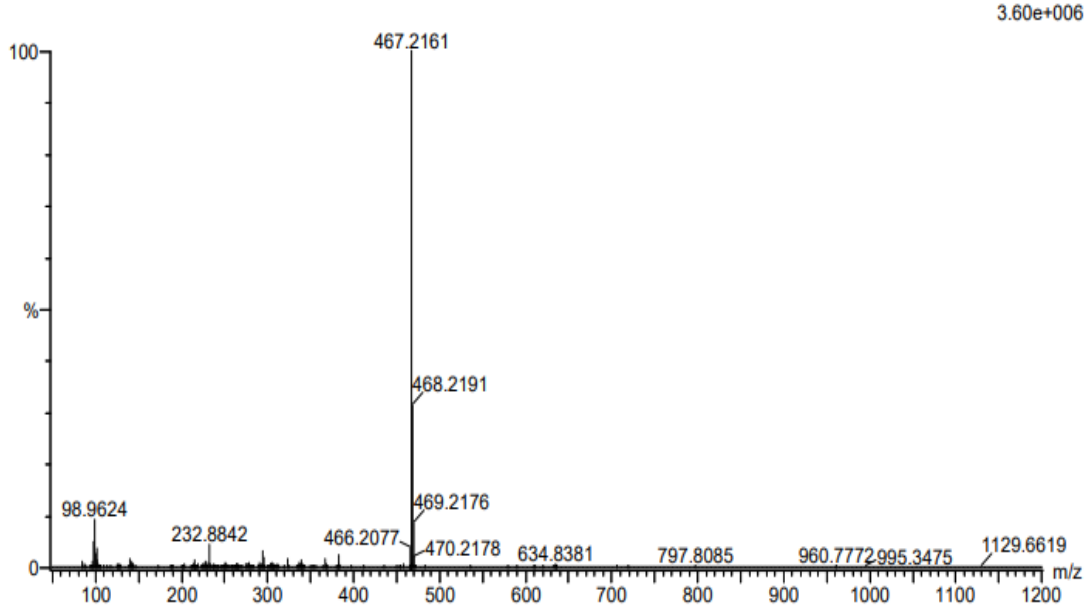

Minimum:				-5.0				
Maximum:		5.0	2.0	50.0				
Mass	Calc. Mass	mDa	PPM	DBE	i-FIT	Norm	Conf(%)	Formula
467.2161	467.2157	0.4	0.9	16.5	946.9	0.000	99.99	C30 H31 N2 O S
	467.2157	0.4	0.9	3.5	960.1	13.263	0.00	C15 H35 N10 O S3
	467.2155	0.6	1.3	13.5	956.8	9.919	0.00	C22 H27 N8 O4
	467.2153	0.8	1.7	-2.5	962.9	16.056	0.00	C15 H43 N6 S5

J.7 FT-IR of MSN-006 (neat)

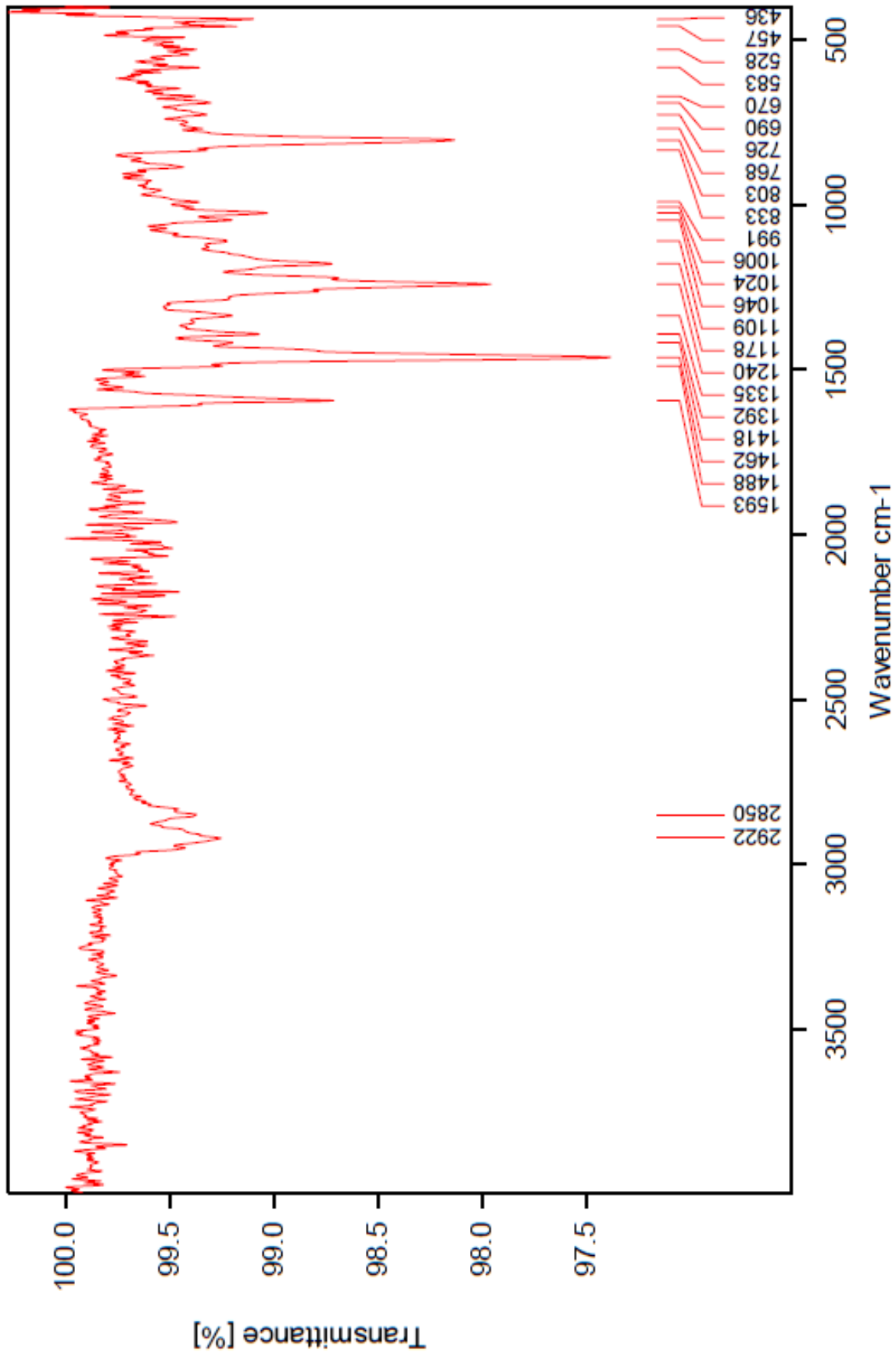

J.8 UV-Vis of MSN-006 in DCM

Report Date: 14:36:42, 11/19/2019

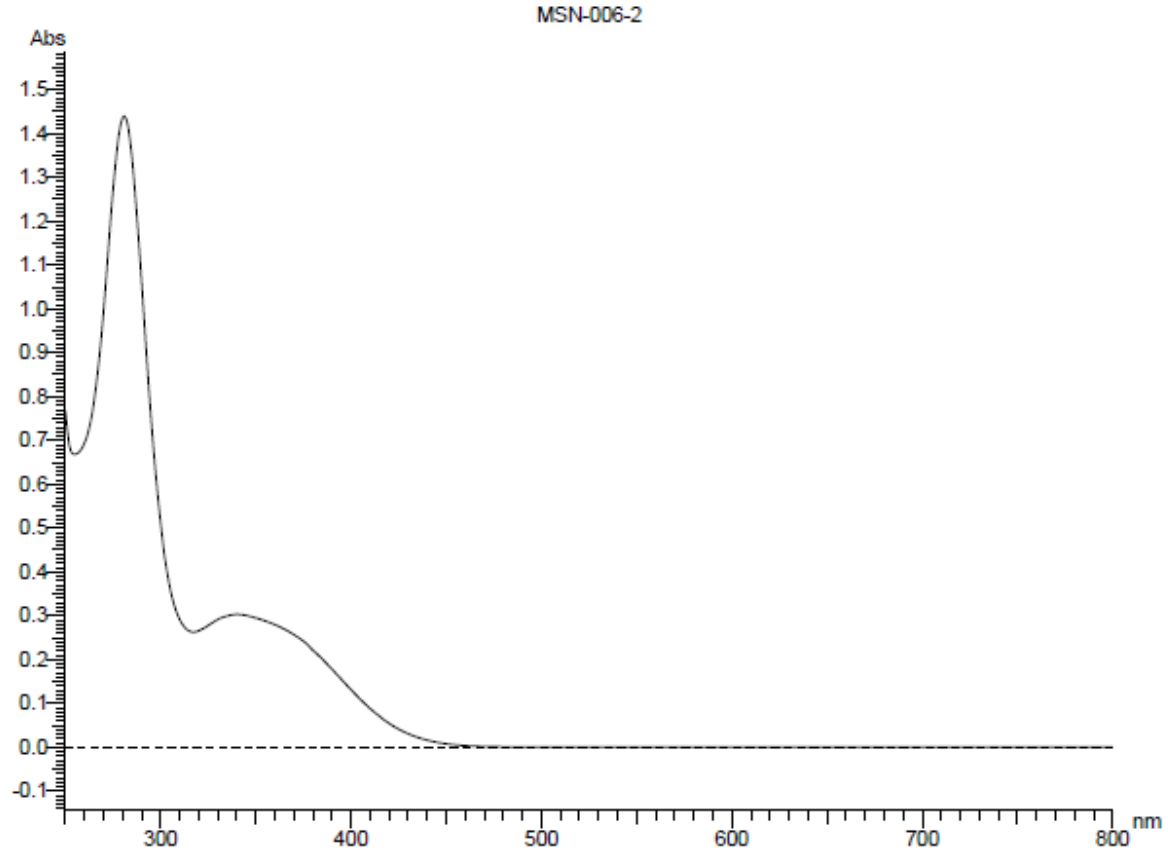

Sample: MSN-006-2
File name:
Run Date: 14:33:07, 11/19/2019
Operator: user
Comment:

Instrument
Model: U-1900 Spectrophotometer
Serial Number:
ROM Version: 3J05300 02

Instrument Parameters

Measurement Type:	Wavelength Scan
Data Mode:	Abs
Starting Wavelength:	800.0 nm
Ending Wavelength:	250.0 nm
Scan Speed:	400 nm/min
Sampling Interval:	1.0 nm
Slit Width:	4.00 nm
Lamp change mode:	Auto
Auto change wavelength:	340.0 nm
Baseline Correction:	User
Wait time:	0 s
Cycle Time:	0 min
Replicates:	1
Response:	Medium
Path Length:	10.0 mm

(Abs values are corrected to 10 mm path length)

Peak Integration

Method:	Rectangular
Sensitivity:	1
Threshold:	0.0100

Peaks

Peak #	Start (nm)	Apex (nm)	End (nm)	Height (Abs)	Area (Abs*nm)	Valley (nm)	Valley (Abs
1	800.0	340.0	317.0	0.303	24.008	317.0	0.263
2	317.0	281.0	250.0	1.440	53.593	250.0	0.767

J.9 UV-Vis of MSN-006 adsorbed on TiO_2 w/ CDCA

Report Date: 11:24:09, 12/04/2019

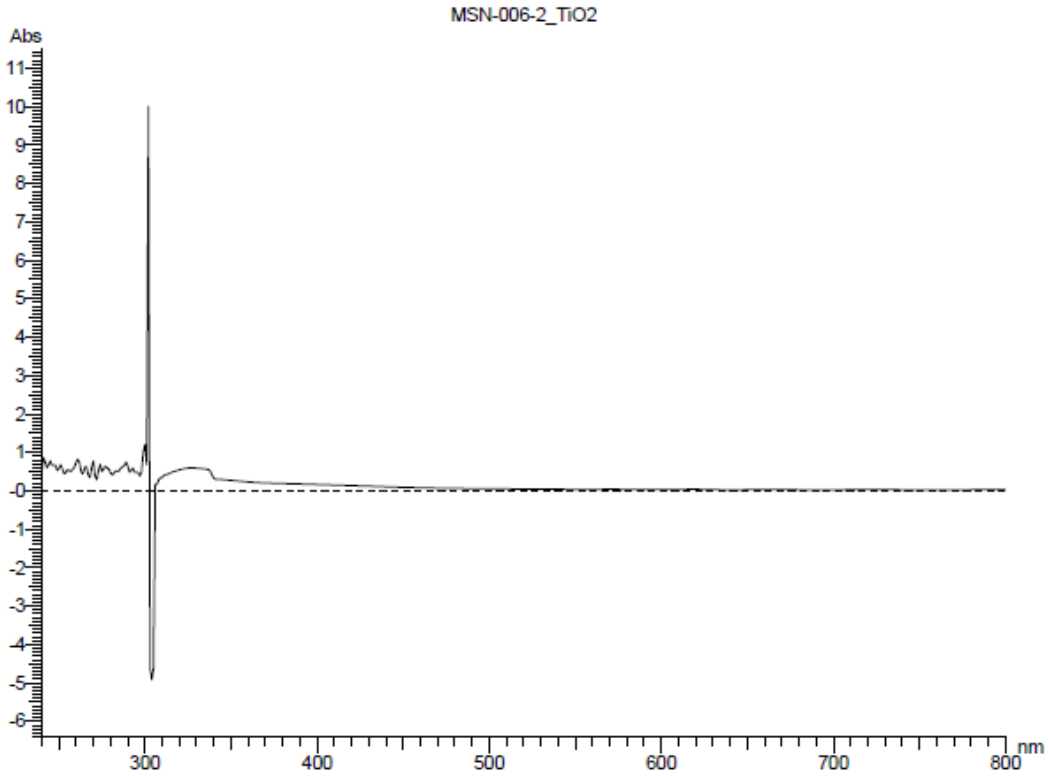

Sample: MSN-006-2_TiO2
File name:
Run Date: 11:20:53, 12/04/2019
Operator: user
Comment:

Instrument
Model: U-1900 Spectrophotometer
Serial Number:
ROM Version: 3J05300 02

Instrument Parameters

Measurement Type:	Wavelength Scan
Data Mode:	Abs
Starting Wavelength:	800.0 nm
Ending Wavelength:	240.0 nm
Scan Speed:	400 nm/min
Sampling Interval:	1.0 nm
Slit Width:	4.00 nm
Lamp change mode:	Auto
Auto change wavelength:	340.0 nm
Baseline Correction:	User
Wait time:	0 s
Cycle Time:	0 min
Replicates:	1
Response:	Medium
Path Length:	10.0 mm

(Abs values are corrected to 10 mm path length)

Peak Integration

Method:	Rectangular
Sensitivity:	1
Threshold:	0.0100

Peaks

Peak #	Start (nm)	Apex (nm)	End (nm)	Height (Abs)	Area (Abs*nm)	Valley (nm)	Valley (Abs
1	800.0	719.0	691.0	0.036	3.099	691.0	0.021
2	691.0	665.0	641.0	0.040	1.580	641.0	0.024
3	641.0	617.0	597.0	0.042	1.552	597.0	0.031
4	597.0	328.0	304.0	0.595	34.898	304.0	-4.915
5	304.0	302.0	297.0	10.000	4.231	297.0	0.385
6	297.0	289.0	281.0	0.751	9.159	281.0	0.420
7	281.0	274.0	268.0	0.686	7.395	268.0	0.345
8	268.0	261.0	253.0	0.828	8.921	253.0	0.449

J.10 UV-Vis of MSN-006 adsorbed on TiO_2 w/o CDCA

Report Date: 12:00:47, 02/05/2020

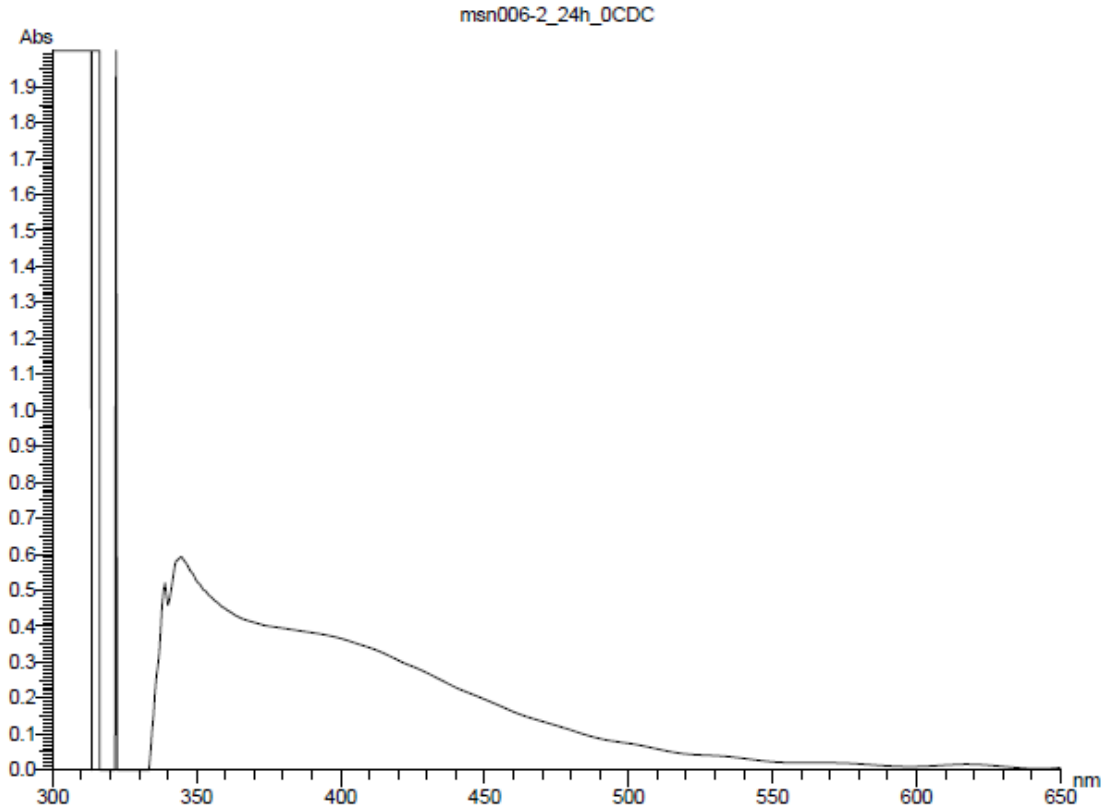

Sample: msn006-2_24h_0CDC
File name:
Run Date: 11:58:16, 02/05/2020
Operator: user
Comment:

Instrument
Model: U-1900 Spectrophotometer
Serial Number:
ROM Version: 3J05300 02

Instrument Parameters

Measurement Type:	Wavelength Scan
Data Mode:	Abs
Starting Wavelength:	650.0 nm
Ending Wavelength:	300.0 nm
Scan Speed:	400 nm/min
Sampling Interval:	0.5 nm
Slit Width:	4.00 nm
Lamp change mode:	Auto
Auto change wavelength:	340.0 nm
Baseline Correction:	User
Wait time:	0 s
Cycle Time:	0 min
Replicates:	1
Response:	Medium
Path Length:	10.0 mm

(Abs values are corrected to 10 mm path length)

Peak Integration

Method:	Rectangular
Sensitivity:	1
Threshold:	0.0100

Peaks

Peak #	Start (nm)	Apex (nm)	End (nm)	Height (Abs)	Area (Abs*nm)	Valley (nm)	Valley (Abs
1	650.0	344.5	323.5	0.593	47.655	323.5	-0.857
2	323.5	322.0	320.5	10.000	-2.353	320.5	-6.178

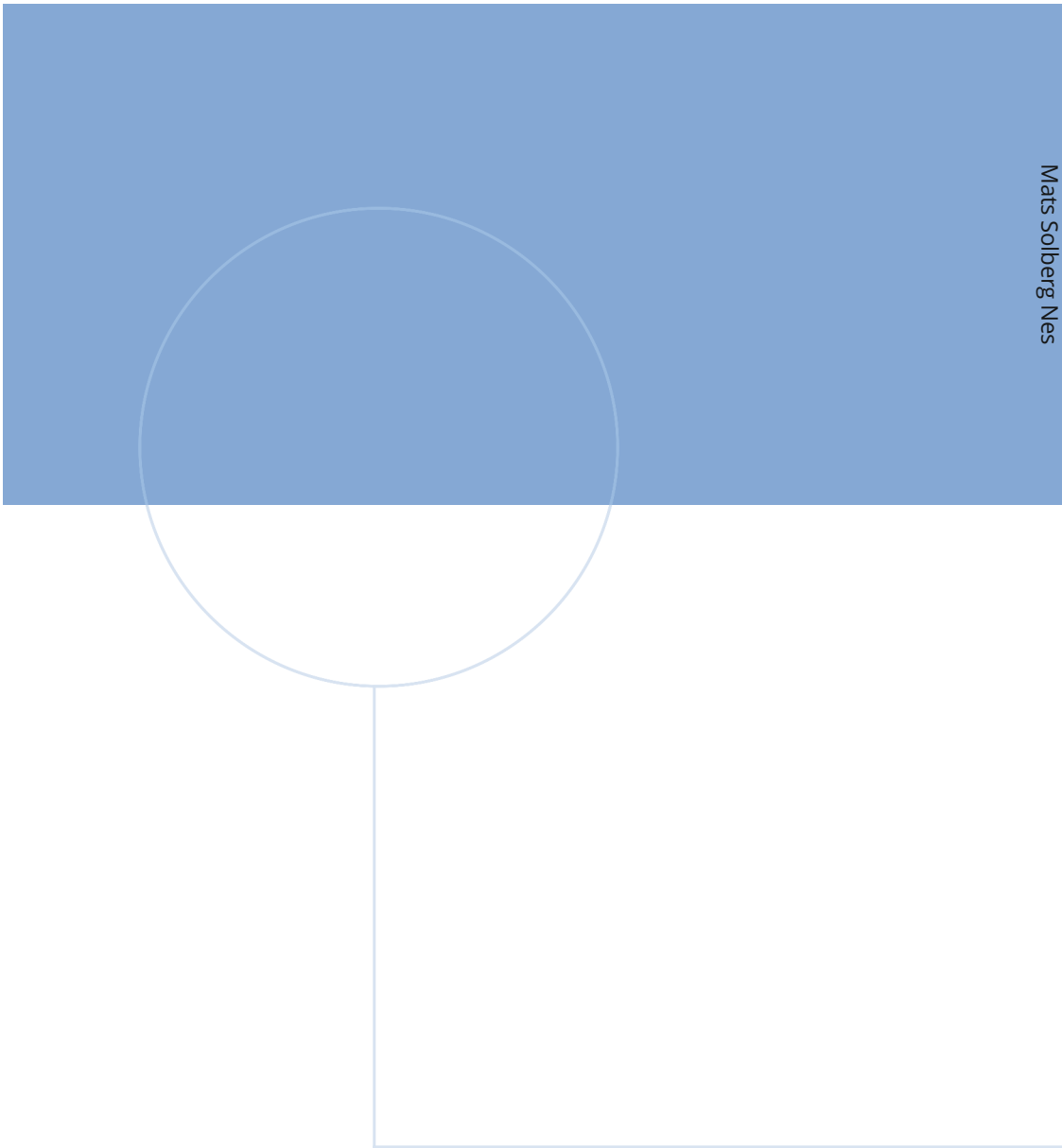

Mats Solberg Nes

NTNU
Norwegian University of
Science and Technology